



저작자표시 2.0 대한민국

이용자는 아래의 조건을 따르는 경우에 한하여 자유롭게

- 이 저작물을 복제, 배포, 전송, 전시, 공연 및 방송할 수 있습니다.
- 이차적 저작물을 작성할 수 있습니다.
- 이 저작물을 영리 목적으로 이용할 수 있습니다.

다음과 같은 조건을 따라야 합니다:



저작자표시. 귀하는 원저작자를 표시하여야 합니다.

- 귀하는, 이 저작물의 재이용이나 배포의 경우, 이 저작물에 적용된 이용허락조건을 명확하게 나타내어야 합니다.
- 저작권자로부터 별도의 허가를 받으면 이러한 조건들은 적용되지 않습니다.

저작권법에 따른 이용자의 권리는 위의 내용에 의하여 영향을 받지 않습니다.

이것은 [이용허락규약\(Legal Code\)](#)을 이해하기 쉽게 요약한 것입니다.

[Disclaimer](#) 

**Numerical investigation of shear zone
formation: implications for bimaterial
instability and surface heat flux**

Byung-Dal So

A dissertation submitted to Graduate School of Seoul
National University in partial fulfillment of the requirements
for the degree of Doctor of Philosophy

School of Earth and Environmental Sciences

Graduate School

Seoul National University

August, 2013

Contents

Abstract	(1)
List of Figures	(3)
List of Tables	(6)
Chapter 1 Introduction	
1.1. Introduction	(7)
1.2. References	(10)
Chapter 2 Asymmetric lithospheric instability facilitated by shear modulus contrast: implications for shear zones	
Abstract	(14)
2.1. Introduction	(16)
2.2. Numerical model	(18)
2.3. Results and Discussion	(23)
2.3.1. The nature of the asymmetric shear instability	(23)
2.3.2. Effects from other aspects of lithosphere on the instability	(29)
2.3.2.1. The difference in yield strength of bi-material lithosphere	(29)
2.3.2.2. Effect from a geothermal gradient	(31)
2.3.2.3. Variation of the Poisson ratio for whole lithosphere	(32)
2.4. Conclusions	(32)
2.5. References	(34)
2.6. Figures	(41)
2.7. Table	(53)

Chapter 3 An Efficient Implicit-Explicit Adaptive Time-Stepping Scheme for Handling Multi-Timescale Geodynamical Problems in Lithospheric Shear Zone Development

Abstract	(54)
3.1. Introduction	(55)
3.2. General model setup	(57)
3.3. Description of different numerical schemes	(59)
3.3.1. Explicit Scheme	(59)
3.3.2. Implicit scheme	(60)
3.3.3. ATS approach	(61)
3.4. Benchmark tests	(62)
3.4.1. Benchmark test I	(63)
3.4.2. Ogawa's model	(63)
3.5. Two problems of lithospheric shear zone development ..	(65)
3.5.1. R model	(65)
3.5.2. S model	(66)
3.6. Results	(66)
3.7. Discussion	(70)
3.8. Conclusions	(73)
3.9. Appendix	(74)
3.9.1. Explicit scheme	(74)
3.9.2. Implicit scheme	(76)
3.9.3. Benchmark test I	(77)
3.10. References	(80)
3.11. Figures	(86)
3.12. Tables	(98)

Chapter 4 Influence of Temperature-Dependent Thermal Conductivity on Surface Heat-Flow near Major Faults

Abstract	(100)
4.1. Introduction	(101)
4.2. Numerical model	(102)
4.3. Results	(104)
4.4. Discussion	(107)
4.5. Conclusions	(110)
4.6. References	(111)
4.7. Figures	(115)
4.8. Table	(121)

Abstract

I have performed numerical modeling dealing with shear/frictional heating within the lithosphere using high resolution finite element method. I have focused on three different subjects I-III: I) shear heating at the bi-material interface, II) the efficient numerical scheme for calculation of shear heating and III) frictional heating at the fault plane. Those three subjects are strongly related in terms of mathematical similarity and numerical techniques.

In subject I, thermal–mechanical numerical simulations were computed to understand the effects of shear modulus contrast on asymmetric instabilities. Strain-rate and stress-dependent rheology are used with a wide range of activation energy 0–850 kJ mol⁻¹ for all models. Numerical results with enough shear modulus contrast show asymmetric shear instability, which is generated around the interface and then propagates across the interface. Two parts of the lithosphere with different shear moduli (stiff for higher and soft for lower shear modulus lithospheres), which are simply connected to each other without a pre-defined weak zone, were compressed at a constant rate of 2 cm yr⁻¹. The shear modulus contrast has to be close to two for triggering asymmetric shear instability and is found to be by far a more important controlling factor in causing shear instability than activation energy of the creep law. My finding stresses that naturally occurring shear modulus contrast has also important impact on many geological problems related to bimaterial instability.

In subject II, I tested an adaptive time-stepping scheme, in particular, the adaptive time-stepping scheme (ATS) where the implicit is adopted for stages of quasi-static deformation and the explicit for stages involving short timescale nonlinear feedback. To investigate the efficiency of this adaptive scheme, I compared it with implicit and explicit schemes for two different cases involving: (1) shear localization around the predefined notched zone and (2) asymmetric shear instability from a sharp elastic heterogeneity. The ATS resulted in a stronger localization of shear zone than the other two schemes.

This is because either implicit or explicit schemes alone cannot properly simulate the shear heating due to a large discrepancy between rates of overall deformation and instability propagation around the shear zone. My comparative study shows that, while the overall patterns of the ATS are similar to those of a single time-stepping method, a finer temperature profile with greater magnitude can be obtained with the ATS. The ability to model an accurate temperature distribution around the shear zone may have important implications for more precise timing of shear rupturing, which is important in geodynamics.

In subject III, I have studied with high-resolution finite element simulations the potential thermo-mechanical effects ensuing from positive feedback between temperature-dependent thermal conductivity $k(T) \propto (1/T)^b$ and frictional heating in a crust-lithosphere system with both brittle and viscoelastic rheology. The variable conductivity together with frictional heating causes drastic reduction in thermal conductivity and these changes can influence the heat-flux near major faults. When $b = 1$, the temperature is 400 K higher under the fault than that in uniform conductivity case. This is caused by the reduction in thermal conductivity under the surface fault with the temperature rise. Consequently, frictional heating dominates over vertical heat diffusion. In spite of the high temperature around the fault in variable conductivity cases, the surface heat-flux is 60 (for $b = 0.5$) to 80% (for $b = 1$) lower than that in the uniform conductivity case. The fault is thermally insulated by the vertical conductivity contrast between the warm frictional zone and the adjacent cold region underneath. I may be able to explain partly the lack of heat-flow anomalies near major faults and also concur with previous hypotheses on the nature of the shear strength associated with these faults.

Keyword: Shear zone, shear heating, bimaterial, finite element, explicit-implicit adaptive scheme, heat flow, San Andreas Fault

Student number: 2006-22956

List of Figures

Chapter 2

- Figure 2.1 Domain of my 2D FEM model with a 600 km width and 150 km depth under the plane strain assumption (41)
- Figure 2.2 The rainbow color contours show the temperature distribution. Symmetric instability with same shear moduli in soft and stiff lithospheres occurs at 1 Myr (42)
- Figure 2.3 The rainbow color contour shows temperature distribution. (43)
- Figure 2.4 Initiation times of asymmetric instability with varying shear modulus contrast, R_s (shear modulus contrast, from 1 to 20) (44)
- Figure 2.5A The case of low activation energy (200 kJ/mol with $R_s = 3$) (45)
- Figure 2.5B Time history of temperature distribution in the calculating domain of the case of high activation energy (850 kJ/mol with $R_s = 3$) (45)
- Figure 2.6 The temperature profile along interface at 1 Myr with varying activation energy and constant $R_s = 3$ (46)
- Figure 2.7 Domain map of asymmetric instability with parameterized activation energy and shear modulus contrast (47)
- Figure 2.8 Shape of deformation and the shear instability at 1 Myr in cases with different yield strength (48)
- Figure 2.9 Elevated height on the top surface (49)
- Figure 2.10 Shape of deformation and the shear instability at 1 Myr in cases with different yield strength (50)
- Figure 2.11 Comparison of the asymmetric instability between the cases with and without the geothermal gradient (51)
- Figure 2.12 Comparison of the deformation on the top surface with varying Poisson ratio (52)

Chapter 3

- Figure 3.1 The cartoons showing three stages in shear zone development. Red color means high temperature or plastic strain-rate (81)
- Figure 3.2 The schematic description for Ogawa's model (1987) (82)
- Figure 3.3 Temporal evolution of time-step with different shearing rate under the implicit scheme (83)
- Figure 3.4 Total number of iterations with varying shearing rates (84)
- Figure 3.5 Descriptions for R (Figure 3.5.a) and S (Figure 3.5.b) models (85)
- Figure 3.6 Numerical results of R model using the ATS. Detailed explanation of each stage, as given in Figure 3.1, is consistent with this figure (86)
- Figure 3.7 Domain map of asymmetric instability with parameterized activation energy and shear modulus contrast (87)
- Figure 3.8 The temperature profiles along interface at 1 Myr with three different schemes for S model (88)
- Figure 3.9 The variation of time-step with higher extension rate under the implicit scheme (89)
- Figure 3.10 The map of convergence and divergence of S model under the implicit scheme (90)
- Figure 3.11 a. The evolution of time-step of R model in the implicit scheme with a slow extension of 2 cm/yr (91)
- Figure 3.11 b. Temporal variation of time-step in R model under the ATS with extensional velocity = 2 cm/yr (91)
- Figure 3.12 The comparison between analytical solution and numerical result with the explicit and implicit schemes (92)

Chapter 4

Figure 4.1	The schematic description for my model	(115)
Figure 4.2	The temperature distribution with varying values of b at 16% compression under 25 mW/m ² basal heat-flux condition	(116)
Figure 4.3	a. Heat-flux distributions with varying values of b at 16% compression	(117)
Figure 4.3	b. Temporal evolutions of the heat-flux with varying values of b observed at the Point A	(117)
Figure 4.4	a. The heat-flux profiles along the line AB with varying values of b in cases of 25 mW/m ² (solid lines) and 40 mW/m ² (dashed lines) basal heat-fluxes	(118)
Figure 4.4	b. The conductivity profiles along the line AB	(118)
Figure 4.4	c. The heat-flux profiles at 16% compression of high, low end-members (dashed lines) and realistic case with conductivities of feldspar for the crust and olivine for the lithosphere	(118)
Figure 4.4	d. The heat-flux profiles at the same temperature (i.e., 750 K) in the localized zone	(118)

List of Tables

Chapter 2

Table 1	Input parameters	(53)
---------	------------------	------

Chapter 3

Table 1	Input parameters of assessments for three models	(93)
---------	--	------

Table 2	Differences of the three models being assessed	(94)
---------	--	------

Chapter 4

Table 1	Input parameters and notations	(113)
---------	--------------------------------	-------

Chapter 1

1.1. Introduction

The shear instability in the viscoelastic lithosphere is a classical geophysical phenomenon with a great relevance for deep-intermediate focus earthquakes (Griggs and Baker, 1968; Ogawa, 1987). Moreover, the instability can lead to localized lithosphere-scale rupturing (Bercovici, 2002; Branlund et al., 2000; Yoshioka et al., 1995) and other planetary dynamics such as the existence of plate tectonics in Mars and Venus (Cramer and Kaus, 2010) and tidal dissipation on the Jovian moon Io (Nimmo et al., 2007; Peale et al., 1979). Viscous, viscoelastic, and visco-plasto-elastic materials have been utilized to describe the instability responding to exerted forces, such as compression (So et al., 2012), extension (Regenauer-Lieb and Yuen, 1998) and vertical loading (Regenauer-Lieb et al., 2001). These assumptions have been widely adopted for treating the realistic thermal-mechanical behavior of the lithosphere with some degree of numerical accuracy. However, the role of elasticity has been underestimated due to the bias that geodynamics are mainly ruled by long timescale instability. Accordingly, the use of a short time-step for fast timescale instability has been ignored. Elasticity, however, has received some attention from authors (e.g., Ben-Zion, 2001; Bercovici et al., 1992; Brietzke et al., 2006; Burov and Guillou-Frottier, 2005; Harder, 1991) and they reached a conclusion that it is also an important factor in long timescale and large spatial scale instabilities.

Many geophysical surveys have continuously reported a bi-material interface that refers to the elastic moduli discontinuity (e.g., Le Pichon et al., 2005). Moreover, recent studies found that the elastic contrast induces shear instability with a preferred propagation orientation (Ampuero and Ben-Zion, 2008) and enhances instability (So et al., 2012). According to seismological studies that reported the asymmetric distribution of deformation, the seismic velocity and the elastic properties along the fault plane (Lutter et al., 2004; McGuire and Ben-Zion, 2005), the bi-material condition in nature is

common at various spatial scales, such as the grain, glacier and plate boundary scales (Deichmann et al., 2000), and should be considered when geodynamically modeling shear instability.

In this study, I investigated the generation of asymmetric shear instability around the bi-material condition, which is based on the idea that two parts of lithosphere have different shear moduli. I modeled a two-dimensional domain (600 km \times 150 km) with elastoplastic rheology using ABABQUS/Standard (Abaqus Manual, 2009). The predefined weak zones such as fault and low viscosity zones have not been assigned to see the effect of shear modulus contrast on the nucleation of an asymmetric instability. I found that shear modulus contrast would be dominant over activation energy with the bi-material interface; higher shear modulus contrast can generate stronger and faster asymmetric instability crossing the interface for a wide range of activation energies (0–850 kJ/mol).

When the problem at hand has many timescales, a single time integration scheme cannot efficiently solve the problem owing to different stability characteristics between implicit and explicit schemes. In addition, time-stepping itself can induce chaotic phenomena. This hurdle motivates modelers to select an appropriate scheme for this type of geophysical processes. The implicit scheme is commonly employed in a structural modeling and leads to reasonable accuracy in obtaining a relatively stable solution. The main advantage of the implicit scheme is that it can stabilize the solution for a large time-step, but it needs multiple iterations for the convergence within a given tolerance. On the other hand, the explicit scheme is well suited for a fluid dynamical modeling and extremely short timescale problem, such as the impact and severe eroding of elements during calculation (Abaqus Manual, 2009; Iserles, 1996). In spite of a huge discrepancy between both schemes, most of the numerical codes usually adopt only one scheme (e.g., Kaus and Podladchikov, 2006; Regenauer-Lieb and Yuen, 1998). To resolve this inconsistency between multiple timescales and the use of a single scheme, the implicit-explicit adaptive scheme (i.e., ATS scheme) has recently

resurfaced in applied mathematics by Kennedy and Carpenter (2003). Constantinescu and Sandu (2010) and Brown (2011) later improved it. I intend to introduce and apply the philosophy of the ATS scheme for solving problems associated with shear instability.

The importance of selecting the time-stepping method in the understanding of long timescale mantle convection and mantle-lithosphere interaction has been emphasized (Bonnardot et al., 2008). Careful benchmarking has also been carried out in order to compare popular finite element codes (Moresi et al., 1998), but few comparisons for understanding the difference between implicit and explicit schemes have been documented. The main purpose of my work is to assess the effect each scheme has when applied in calculating the instability. Slow (from viscoplasticity) and fast (from elasticity) timescales coexist and interact with each other. This is similar to combustion, which involves many timescales ranging from slow simmering to the final explosive stage (Kassoy, 1976). Therefore, it is required that there is a time integration scheme to cover both instabilities.

I will compare pure explicit, implicit and ATS schemes for three published studies: (1) shear heating for deep focus earthquake (Ogawa, 1987), (2) shear localization and elastic energy release (Regenauer-Lieb and Yuen, 1998) and (3) asymmetric instability around the interface between stiff and soft lithospheres that have different shear moduli (So et al., 2012). The advantage of the particular sequence in using the explicit scheme for short timescale instability and then an implicit scheme for long timescale quasi-static feature is examined in terms of the strength and speed of the instability.

Another important phenomenon is frictional heating on fault plane. Mathematical description for frictional heating is similar with that for shear heating. Moreover, stick-slip behavior of frictional sliding has a wide spectrum of time-scale which requires adaptive time-stepping. I may apply what I have done to geodynamical problems dealing with frictional heating in the lithosphere. The heat flow paradox, which was posed by Brune et al.

(1969) in their geophysical observation at the San Andreas Fault, indicates that heat flow anomalies along major faults on the Earth are unexpectedly lower by a factor of 5 than those from laboratory experiment. This has been a long-standing open problem (Mora and Place, 1998; Saffer et al., 2003). In order to resolve this problem, I should understand the nature of shear zone as a heat source for surface heat flow. Since the amount of the shear/frictional heating is determined by the mechanical strength of lithosphere, people have thought that the determination of fault strength, weak (e.g., Carpenter et al., 2011; Zoback et al., 1987) or strong (e.g., Scholz, 2000), is a prerequisite to explain the paradox. However, temperature-dependent thermal conductivity, which may create the conductivity contrast between shear zone and surrounding crust, has not been considered as a cause of the paradox.

1.2. References

- Ampuero, J. P. and Y. Ben-Zion (2008), Cracks, pulses and macroscopic asymmetry of dynamic rupture on a bimaterial interface with velocity-weakening friction, *Geophys. J. Int.*, 173(2): 674-692, doi: 10.1111/j.1365-246X.2008.03736.x.
- Ben-Zion, Y. (2001), Dynamic ruptures in recent models of earthquake faults, *Journal of the Mechanics and Physics of Solids*, 49(9), pp. 2209-2244.
- Bercovici, D., H. Dick and T. Wagner (1992), Nonlinear viscoelasticity and the formation of transverse ridges, *J. Geophys. Res.*, 97, 14 195–14 206.
- Bonnardot, M.-A., R. Hassani, and E. Tric (2008), Numerical modelling of lithosphere–asthenosphere interaction in a subduction zone, *Earth Planet. Sci. Lett.*, 272, pp. 698-708.
- Branlund, J.M., M. C. Kameyama, D.A. Yuen and Y. Kaneda (2000), Effects of temperature-dependent thermal diffusivity on shear instability in a viscoelastic zone: implications for faster ductile faulting and earthquakes in the spinel stability field, *Earth Planet. Sci. Lett.*, 182(2), pp. 171–185.

- Brietzke, G. B. and Y. Ben-Zion (2006), Examining tendencies of in-plane rupture to migrate to material interfaces, *Geophys. J. Int.*, 167(2), pp. 807-819.
- Burov, E. and L. Guillou-Frottier (2005), The plume head-continental lithosphere interaction using a tectonically realistic formulation for the lithosphere, *Geophys. J. Int.*, pp. doi:10.1111/j.1365-246X.2005.02588.x.
- Carpenter, B.M., Marone, C., and Saffer, D.M., 2011. Weakness of the San Andreas Fault revealed by samples from the active fault zone. *Nature Geoscience*. v. 4, p. 251–254, doi:10.1038/ngeo1089.
- Cramer, F. and B. J. P. Kaus (2010), Parameters that control lithospheric-scale thermal localization on terrestrial planets, *Geophys. Res. Lett.*, 37, L09308.
- Deichmann, N., et al. (2000), Evidence for deep icequakes in an Alpine glacier, *Ann. Glac.*, 31, 85–90, doi: 10.3189/172756400781820462.
- Griggs, D.T. and D.W. Baker (1968), *The origin of deep-focus earthquakes: properties of matter under unusual conditions*, Wiley, New York, pp. 23–42.
- Harder, H., 1991. Numerical simulation of thermal convection with Maxwellian viscoelasticity, *Journal of Non-Newtonian Fluid Mechanics*, 39, 67–88.
- Hibbit, Karlsson and Sorenson Inc. (2009). *Abaqus/Standard User's Manual Version 6.9, Vol.1*.
- Kassoy, D. R. (1976), Extremely rapid transient phenomena in combustion, ignition and explosion, in *Asymptotic methods and singular perturbation*, SIAM-AMS Proceedings, Vol. X.
- Kaus, B. J. P. and Y. Y. Podladchikov (2006), Initiation of localized shear zones in viscoelastoplastic rocks, *J. Geophys. Res.*, 111, B04412, doi: 10.1029/2005JB003652.
- Le Pichon, X., C. Kreemer, and N. Chamot-Rooke (2005), Asymmetry in elastic properties and the evolution of large continental strike-slip faults, *J.*

Geophys. Res., 110, B03405, doi:10.1029/2004JB003343.

Lutter, W.J. et al. (2004), Upper crustal structure from the Santa Monica mountains to the Sierra Nevada, southern California: tomographic results from the Los Angeles regional seismic experiment, Phase II (LARSE II), *Bull. seism. Soc. Am.*, 94(2), 619–632.

McGuire, J.J. and Y. Ben-Zion (2005), High-resolution imaging of the Bear Valley section of the San Andreas Fault at seismogenic depths with fault-zone head waves and relocated seismicity, *Geophys. J. Int.*, 163, 152–164, doi: 10.1111/j.1365-246X.2005.02703.x.

Mora, P. and Place, D., (1998). Numerical simulation of earthquake faults with gouge: Toward a comprehensive explanation for the heat flow paradox. *J. Geophys. Res.*, v. 103, p. 21,067–21,089, doi:10.1029/98JB01490.

Moresi, L.N., Solomatov, V. (1998), Mantle convection with a brittle lithosphere: thoughts on the global tectonic styles of the earth and venus, *Geophysical Journal International* 133, 669–682.

Nimmo, F., J. R. Spencer, R. T. Pappalardo, and M. E. Mullen (2007), Shear heating as the origin of the plumes and heat flux on Enceladus. *Nature*, 447(7142), 289-291.

Ogawa, M. (1987), Shear instability in a viscoelastic material as the cause of deep focus earthquakes, *J. Geophys. Res.*, 92, 13801–13810.

Peale, S. J., P. Cassen and R. T. Reynolds (1979), Melting of Io by tidal dissipation, *Science*, 203, pp. 892-894.

Regenauer-Lieb, K. and D. A. Yuen (1998), Rapid conversion of elastic energy into plastic shear heating during incipient necking of the lithosphere. *Geophys. Res. Lett.*, 25(14): doi: 10.1029/98GL02056.

Regenauer-Lieb, K., D.A. Yuen and J. M. Branlund, (2001), The initiation of subduction: criticality by addition of water?, *Science*, 294 (5542), pp. 578–580.

- Saffer, D.M., Bekins, B.A. and Hickman, S., (2003). Topographically driven groundwater flow and the San Andreas heat flow paradox revisited. *J. Geophys. Res.*, v. 108, doi:10.1029/2002JB001849.
- Scholz, C. H., (2000). Evidence for a strong San Andreas fault. *Geology*, v. 28, p. 163– 166.
- So, B.-D., D. A. Yuen, K. Regenauer-Lieb, and S.-M. Lee (2012), Asymmetric lithospheric instability facilitated by shear modulus contrast: implications for shear zones, *Geophys. J. Int.*, 190(1): 23-36.
- Yoshioka, S., D. A. Yuen and T. B. Larsen (1995), Slab weakening: Mechanical and thermal-mechanical consequences for slab detachment, *Island Arc* 4(2), 89-103.
- Zoback, M.D., Zoback, M.L., Mount, V.S., Suppe, J., Eaton, J.P., Healy, J.H., Oppenheimer, D., Reasenber, P., Jones, L., Raleigh, C.B., Wong, I.G., Scotti, O., and Wentworth, C., (1987). New evidence on the state of stress of the San Andreas fault system. *Science*. v. 238, p. 1105–1111, doi:10.1126/science.238.4830.1105.

Chapter 2

Asymmetric lithospheric instability facilitated by shear modulus contrast: implications for shear zones*

Abstract

Viscoplasticity has been considered to be a dominant element in causing the nucleation of shear instability leading to lithospheric weakening. Here, I propose that a simple contrast in shear moduli may be sufficient for explaining the fast timescale asymmetric shear instability in a bimaterial setting. Not much attention has been paid to heterogeneous elasticity in geodynamical modeling because it is dominant only for short timescales. Up to now, no studies have been made on asymmetric shear instability induced by elastic modulus contrast. Thermal–mechanical numerical simulations based on high-resolution (from $0.4 \text{ km} \times 0.4 \text{ km}$ to $0.2 \text{ km} \times 0.4 \text{ km}$ meshes) finite-element methods were performed to understand the effects of shear modulus contrast on inducing asymmetric instabilities. Strain-rate and stress-dependent rheology are used with a wide range of activation energy $0\text{--}850 \text{ kJ mol}^{-1}$ for all models. Numerical results with enough shear modulus contrast show asymmetric shear instability, which is generated around the interface and then propagates across the interface. Two parts of the lithosphere with different shear moduli (stiff for higher and soft for lower shear modulus lithospheres), which are simply connected to each other without a pre-defined weak zone, were compressed at a constant rate of 2 cm yr^{-1} . Having different shear modulus is justified by chemical heterogeneity of geological minerals and their pressure–temperature dependence. To explore the dynamical effects generated by the contrast in the elastic modulus, the shear modulus of the soft lithosphere is fixed at 32 GPa, whereas that of stiff lithosphere is increased systematically from 32 up to 640 GPa. I also examined the role of activation energy ($0\text{--}850 \text{ kJ mol}^{-1}$) on the geometrical pattern and the initiation time of

asymmetric shear localization. The shear modulus contrast has to be close to two for triggering asymmetric shear instability and is found to be by far a more important controlling factor in causing shear instability than activation energy of the creep law. The instability develops rapidly between 250,000 and 500,000 yr after deformation begins, and thermal weakening in the shear zone is greater, when a stronger shear modulus contrast is prescribed. My work suggests that initiation of lithosphere-scale asymmetric instability would be faster than previous considerations. My finding stresses that naturally occurring shear modulus contrast has also important impact on many geological problems related to bimaterial instability.

Keyword: bimaterial interface, shear heating, asymmetric deformation

* An edited version of this chapter was published in Geophysical Journal International at 2012. So, B.-D. and D. A. Yuen et al (2012), Asymmetric lithospheric instability facilitated by shear modulus contrast: implications for shear zones, Geophysical Journal International, 190(1): 23-36, doi: 10.1111/j.1365-246X.2012.05473.x.

2.1. Introduction

Shear localization due to thermal–mechanical positive feedback has been investigated for a long time as a potential mechanism for the generation of shear zones and deep focus earthquakes (Ogawa, 1987). Complex viscoplastic rheologies (Kameyama et al. 1997; Branlund et al. 2001), a pre-defined fault or weak zone (Toth & Gurnis 1998; Doin & Henry 2001) and also sediment loading on passive margins (Regenauer-Lieb et al. 2001) has been thought to be important elements giving rise to unstable shear-heating instability at convergent plate boundaries.

However, these investigations have commonly assumed an imposed weak zone, complex plastic rheologies related to water content (Regenauer-Lieb et al. 2001) and other weakening processes (Yamasaki & Seno 2003; Mizoguchi et al. 2006), such as a velocity-dependent frictional coefficient (Fukuyama & Madariaga 1998; Goldsby & Tullis 2002). To improve on these models, plastic strength and shear localization for crust and mantle rocks were extensively studied with constraints drawn from laboratory experiments and field studies. For instance, Karato et al. (1998) reported that a significant plastic strength drop occurs during the phase transition from olivine to ringwoodite due to grain size reduction. Obata & Karato (1995) also noted that shear localization is promoted by high stress and low temperature, which corresponds to the environment of cold subducting slab.

Since elasticity is dominant over short timescales, viscoelasticity, which prevails for long timescale dynamics, has been widely adopted to investigate the nature of subduction zones (Zhong & Gurnis 1995; Billen & Gurnis 2001; Billen 2008). Thus, the role of elasticity has been downplayed and thought as being less important component compared with viscoelastic behaviour in long timescale problems, such as subduction. Except for some short-timescale studies (e.g. Weertman 1980; Adams 1995; Ben-Zion 2001, 2012; Brietzke & Ben-Zion 2006), most researchers in geodynamical modelling have not paid enough attention to the contrast in elastic properties as triggering mechanism for thermal weakening. Shear localization caused by

the contrast in elastic property is not well-understood and thus a systematic study of its fundamental effect in shear instability is necessary.

The shear modulus depends strongly on the type of mineral and pressure–temperature condition (Jackson & Liebermann 1974; Wentzcovitch et al. 2004), and the presence of solid-state phase transition (Stølen & Trønnes 2007). Shear modulus of minerals have been derived from first principle calculations dealing with thermodynamics and the relationship between S- and P-wave velocities.

The most popular and easiest example about bimaterial Earth materials is that concerning oceanic and continental lithospheres because they are composed of different minerals with different shear moduli. Feldspar, pyroxene and olivine which compose oceanic lithosphere have about three times larger shear modulus than quartz which is main composition of continental lithosphere (Hacker et al. 2003). However, the shear wave velocity contrast between the oceanic and continental lithospheres varies by a small percentage (Levander et al. 2007). This may indicate that the shear modulus contrast between oceanic and continental lithosphere is too small to initiate an asymmetric shear instability. However, from seismology short-wavelength heterogeneity is difficult to be imaged, but common along the margins of continental lithosphere (Yoshimoto et al. 1997), such as from intrusion of granite into basaltic outcrops along the Chinese eastern coast in Guangdong and Zhejiang. Short-wavelength heterogeneity from seismic inversion does not show convincing correlation because it is difficult to be imaged due to sensitivity to the type of data and damping algorithms used for seismic inversion (van der Hilst et al. 1997). Thus, it is possible that small-scale heterogeneity undetectable from seismic imaging can produce the short-wavelength thermomechanical instabilities, which can initiate a whole long-wavelength process. The diffusion and propagation of the instability, from small wavelength to lithospheric wavelength scale, are important and represents a promising mechanism for explaining large-scale shear instability. The concept that small-scale heterogeneity causes large-scale instabilities is

widely applied to many previous studies dealing with viscoelastic lithosphere. For example, Regenauer-Lieb & Yuen (1998) employed the small-scale (about $5 \text{ km} \times 5 \text{ km}$) notched zone on the top surface for the ductile faulting in whole spatial and temporal domains. A small and low viscosity seed for generating the instability throughout whole domain is also used in many studies such as by Huismans & Beaumont (2002).

When the shear moduli of two neighbouring materials (i.e. bimaterial (Rosakis et al. 1998; Ben-Zion & Shi 2005)) have a sufficiently large contrast, applied forces and consequent deformations around the interface may be considerably different over short timescales (Ben-Zion & Shi 2005). Thus, elastic shear modulus contrast may play an important role in short timescales in bimaterial systems, this poignant issue should not be overlooked in shear instability. The word of shear instability means the localized storage and fast release of elastic energy. I concentrate my attention on the effect of shear modulus contrast on generation of the asymmetric instability at a bimaterial interface. In particular, my study investigates (1) the timing, (2) the intensity of asymmetric instability and (3) its geological implications for initiation of weak zone and making it favourable for large-scale deformation in plate boundary. To understand lithospheric-scale large deformation, it is absolutely essential to study the thermal weakening of lithosphere and determine the features of instability such as timing, intensity and their developed asymmetry. In brief, my main aim is to understand the nature of asymmetric shear instability as a consequence of the shear modulus contrast.

2.2. Numerical model

I examine the development of asymmetric shear instability around the interface of bi-material with elasto-plastic rheologies under an imposed constant compression by using 2D fully coupled thermal-mechanical FEM code Abaqus/Standard (Hibbit et al. 2009) under the plane strain assumption. The rectangular domain is 150 km deep and 600 km wide. The left (in red

color) and right (in blue color) domains have different shear moduli, but have the same plastic rheology (Figure 2.1). Red and blue regions are respectively soft and stiff lithospheres with small and large shear moduli. More than 0.5 million heterogeneous Lagrangian quadratic type elements with highly resolved mesh ($0.2 \text{ km} \times 0.4 \text{ km}$) around interface and the region under the constant stress loading and coarse mesh ($0.4 \text{ km} \times 0.4 \text{ km}$) in other places have been prescribed. No weak zone, fault and notched zone for plastic instability nucleation have been prescribed, and the left and right sides are just attached as a frictionless interface. A free-surface boundary condition (i.e., no surface traction stress) and zero-horizontal-velocity boundary condition were applied at top and left boundary, respectively. The bottom is not allowed to move vertically. But if this model is applied for long timescale problem, then dash-pot element is needed to mimic the isostatic restoring force (Regenauer-Lieb et al. 2001), but this is a short timescale problem of $O(10^0)$ Myr duration and thus a vertically fixed bottom boundary should be appropriate. In the energy equation, all boundaries are thermally insulated. In modeling subduction the free-surface case (e.g. Gurnis et al. 1996) has been employed for reproducing the deformation of overriding plates above the slab. Since asymmetric lithospheric deformation is extremely essential, the free-surface boundary condition is definitely suitable. Calculations with both a free-surface boundary condition and a free-slip condition are found to differ not too much in this and other comparative studies (OzBench et al. 2008).

A constant and tiny pressure of 1 MPa is prescribed along a 100 km horizontal strip at the top of the domain. If I convert this value of pressure into sedimentary loading, which is a popular reason for initiating shear instability, the pressure corresponds to a sediment thickness of less than 0.1 km with a density of 2700 kg/m^3 . Strictly speaking, a small sedimentary loading is not required for generating asymmetric instability. The strength and initiation timing of asymmetric shear instability is very similar, regardless whether the loading is applied or not. However, the solution has a tendency to diverge, when a high shear modulus contrast (i.e. $R_s > 10$) is imposed without sedimentary loading at the surface. This convergence problem is caused by

step- function due to the stress jump at the interface from the high shear modulus contrast. The sedimentary loading acts as a buffer against the abrupt stress jump at the interface of the bi-material lithosphere. The solution is consequently stabilized under a high enough shear modulus contrast.

I will focus on the dynamical effect of shear modulus contrast ($R_s =$ shear moduli of stiff / soft lithospheres) on thermal instability. The values of R_s are systemically varied from 1 to 20. To find out more about the effect of shear modulus contrast, Young modulus (100 GPa) and Poisson ratio (0.3), which are other important elastic properties, have been maintained constant for both materials in all models. The time interval of all calculations ranges from 1 Myr to 4 Myr, and the time step is automatically selected as between 10^{-5} sec and 1000 yrs with full Newtonian iterative implicit scheme. The smallest time steps are employed in the initial stages, which last a very short time.

Time-integration dealing with partial differential equations can be divided into implicit and explicit schemes. Implicit scheme can have numerical stability, regardless of the size of time stepping for a given tolerance (i.e. 10^{-6}), but requires much computational cost for solving non-linear stiff problem. On the other hands, explicit scheme holds numerical stability with much less computational cost per time step (Regenauer-Lieb and Yuen, 1998), but needs very small size of time step and then consequently requires too many time steps for the entire run. Additionally, the dynamic problem which has short timescale is best solved by using an explicit scheme. The dynamic problem with multiple timescales cannot be solved completely with only one scheme. In recognition of this fact, the implicit-explicit (IMEX) mixed method was recently developed for efficient and accurate calculation (Kennedy et al. 2003; Constantinescu et al. 2010). The adaptive scheme for selection, which depends on timescale of problem and/or the IMEX scheme should be utilized to understand fully the instability induced by the elastic contrast, because this instability develops with a multi-scale resolution manner in time (So et al. 2011).

The non-linear effect due to a large elastic displacement on the subsequent time step is included in the Abaqus package (Abaqus Manual, 2009). Two types of initial temperature condition are adopted. The one is the uniform temperature distribution (978 K) for the entire domain to investigate the pure effect of shear modulus contrast on shear instability. Another is the depth-dependent temperature distribution. The linear geothermal gradient (i.e., 273 K for the top and 1273 K the bottom) is utilized. This is not meant to be a realistic geotherm but a first order attempt to assess the effects from geothermal gradients and shear modulus contrast on the feature of shear instability. Thus, the simple gradient is justified. The maximum allowable of temperature change for each time step is limited to 25 K. The Abaqus solver can effectively handle asymmetric matrix encountered in nonlinear thermal-mechanical feedback problems, as shown by previous works (e.g. Regenauer-Lieb and Yuen, 1998). Calculation was repeated over a finer grid to check the convergence and solution accuracy. Equation 1 represents the objective Jaumann derivative of the stress tensor (Kaus and Podladchikov, 2006).

$$\frac{D\tau_{ij}}{Dt} = \frac{\partial\tau_{ij}}{\partial t} + v_i \frac{\partial\tau_{ij}}{\partial x_i} - W_{ik}\tau_{kj} + \tau_{ik}W_{kj} \quad (1)$$

$$W_{ij} = \frac{1}{2} \left[\frac{\partial v_i}{\partial x_j} - \frac{\partial v_j}{\partial x_i} \right] \quad (2)$$

$$\rho c_P \frac{DT}{Dt} = \rho c_P \left[\frac{\partial T}{\partial t} + v_k \frac{\partial T}{\partial x_k} \right] = \frac{\partial}{\partial x_i} \left(k \frac{\partial T}{\partial x_i} \right) + \Psi \left[\dot{\epsilon}_{ij}^{\text{total}} - \frac{1}{2\mu} \frac{D\tau_{ij}}{Dt} \right] \quad (3)$$

D/Dt is the material derivative, τ_{ij} and v_i are deviatoric stress tensor, and i -direction velocity of displacement, respectively. W_{ij} is spin rate defined by Equation 2. Equation 3 represents the evolutionary energy equation with thermal-mechanical coupling. The 2nd term of right-hand side of Equation 3 denotes the viscous dissipation. Ψ indicates the efficiency of conversion between the plastic strain-rate and shear heating (Regenauer-Lieb and Yuen, 1998). The last term on the right-hand side of Equation 3 represents the coupling between temperature and plastic strain-rate.

$$\dot{\epsilon}_{ij}^{\text{total}} = \frac{1}{2} \left[\frac{\partial v_i}{\partial x_j} + \frac{\partial v_j}{\partial x_i} \right] \quad (4)$$

$$\dot{\epsilon}_{ij}^{\text{elastic}} = \frac{1}{2\mu} \frac{D\tau_{ij}}{Dt} \quad (5)$$

$$\dot{\epsilon}_{ij}^{\text{plastic}} = A J_2^{n-1} \tau_{ij} \exp\left(-\frac{Q}{RT}\right) \quad (6a)$$

$$J_2 = \left(\frac{1}{2} \tau_{ij} \tau_{ij} \right)^{1/2} \quad (6b)$$

$$\dot{\epsilon}_{ij}^{\text{total}} = \dot{\epsilon}_{ij}^{\text{elastic}} + \dot{\epsilon}_{ij}^{\text{plastic}} \quad (7)$$

The total strain-rate $\dot{\epsilon}_{ij}^{\text{total}}$ is simply the sum of elastic strain rate $\dot{\epsilon}_{ij}^{\text{elastic}}$ and plastic strain rate $\dot{\epsilon}_{ij}^{\text{plastic}}$ (see Equations 4–7). J_2 (Equation 6b) represents the second invariant of deviatoric stress tensor. I have employed the Von Mises yield criterion with a yield strength σ_y . This simple Von Mises criterion has been used to define the moment of failure, when the material is not deforming elastically and provides an appropriate assumption for studying multi-scale fault mechanics (Moresi et al. 1998). I use a yield strength of 100 MPa. If the second invariant of deviatoric stress tensor is larger than yield strength, the temperature and stress- dependent plastic rheology (Equation 6a) (Glen, 1955; Hutter, 1983; Karato, 2008) is activated and the total strain-rate becomes then the sum of elastic and plastic strain-rates (Equation 7). The activation energy and deviatoric stress-dependent, plastic strain-rate are set to be the same in the two materials. The values of the parameters are given in Table 1.

The right-hand side (stiff) of the computational domain is set to have a larger shear modulus than the left side (soft) in all models. In many studies, a soft crust (e.g. continental crust) is depicted as having quartz-rich composition with a shear modulus of about 40 GPa (Henderson and Henderson, 2009; Hacker et al. 2003). On the other hand, a stiff crust (e.g. oceanic crust) contains feldspar, pyroxene and olivine-rich composition of 100 to 120 GPa shear modulus (Yeganeh-Haeri et al. 1989; Henderson and

Henderson, 2009). If I use the concept of asymmetric instability from shear modulus contrast, I may support generation of asymmetric instability and weak zone around the boundary where shear moduli are changed. Oceanic-continental passive margin and subducting slab under conditions of pressure-temperature changing and phase transition (Hill, 1952) are good candidates for this type of boundary. van Hunen and Allen (2011) concluded that the collision of positive buoyant continental crust induces a strong extensional strain and subsequent slab detachment. However, if I introduce asymmetric instability due to shear modulus contrast, the generation of shear zone that represents the seed for slab detachment can occur without any special tectonic intervention (e.g. collision of buoyant lithosphere).

Strictly speaking, the assumption that two different lithospheres have the same mechanical thickness and plastic properties may not be entirely realistic. However, my aim is to investigate simply the effects of R_s on the development of asymmetric instability. For this purpose, the simplification can be justified.

2.3. Results and Discussion

2.3.1. The nature of the asymmetric shear instability within a bi-material lithosphere

The temporal development of the temperature field over time is plotted for a constant compression rate (2 cm/yr) at time of 1 Myr. Figure 2.2 shows temperature distribution for $R_s = 1$ (e.g. no shear modulus contrast) where the shear moduli of stiff and soft lithospheres are the same at 32 GPa. The symmetric instability is facilitated by pressure applied at the top and a constant horizontal deformation imposing from the side. No asymmetric shear instability is observed in the case of $R_s = 1$. Even when the deformation was continued up to 4 Myr and activation energy was lowered down to zero, asymmetric instability at the interface did not develop in the $R_s = 1$ case. There is then no possibility that nucleation of weak zone. In addition, no

asymmetric deformation feature appears at all in the case of $R_s = 1$. The influence of the elasticity (e.g. Young's modulus) of the whole plate has been investigated in other previous studies. However, they concluded that the elastic modulus has a small effect on large-scale subduction motion and stress fields within subducting slabs (Capitanio et al. 2007). On the other hand, I introduce bi-material lithosphere having shear modulus contrast within it to generate the asymmetric shear instability. This approach is novel and distinguishes itself from all other previous works in that they only focused on an homogeneous elastic plate without considering any thermo-mechanical coupling.

Figures 2.3.a, b and c illustrate the thermal field for $R_s = 3$ and 498 kJ/mol activation energy for different time steps. A quasi-symmetric instability is usually generated at an early stage (before 0.34 Myr). Then the seeds of asymmetric instability (see red circle in Figure 2.3a in the left bottom and the right top of the domain) appear. Eventually the instabilities extend to the bottom and top, and merge at 0.41 Myr. I envisage that this asymmetric instability may be capable of producing quickly a shear zone, which may lead to rapid deformations at plate boundary. I believe that the asymmetric instability becomes more coherent with the passage of time. In Figure 2.3c, the asymmetric deformation, which resembles a form of obduction and subduction, is observed. Subduction and obduction like features are shown in both the right and left sides of the domain, respectively. In Figure 2.5A-c representing the case of 200 kJ/mol activation energy and $R_s = 3$, a stronger asymmetric instability is generated with a smaller activation energy. The steeper underthrusting angle (i.e. meaning stronger asymmetric deformation) in the stiff lithosphere side is shown in the case of lower activation energy.

Figure 2.4 demonstrates the initiation time for activation energy of 498 kJ/mol with different values of R_s . If R_s is smaller than 1.7, no asymmetric instability is produced with any activation energy. This result argues that there exists a critical shear modulus contrast for asymmetric instability. As mentioned previously, the shear modulus of lithospheric minerals can be

changed by state variables, such as pressure and/or temperature; the shear modulus can be calculated or measured as a function of temperature and pressure (Hill 1952; Anderson et al. 1992; Bina et al. 1992). Consequently, thermal–mechanical instability induced by shear modulus contrast is highly feasible in nature. A large variation in initiation time (~ 0.5 and ~ 0.3 Myr for $R_s = 1.7$ and $R_s = 4$, respectively) occurs between $R_s = 1.7$ and 4. Beyond $R_s = 4$, the initiation time of the instability appears to converge rapidly to about 0.25 Myr. In laboratory experiments and calculations, shear modulus can be varied by up to factor of 5 or more with temperature and pressure (Berckhemer et al. 1982). Therefore, such a shear modulus variation is possible and hence the instability is highly feasible. I have found that asymmetric instability in the soft-stiff lithospheric boundary may occur at timescales much shorter than 1 Myr. This short timescale of around 1 Myr does not mean the timing of a mechanical break-off, but rather the timescale for creating a thermally weakened zone.

To investigate the effect of activation energy, I applied unrealistically large and small activation energy values of 850 kJ/mol and 200 kJ/mol, respectively. In Figure 2.5 shows a time sequences of temperature profile, the case of lower activation energy (200 kJ/mol, $R_s = 3$, see Figure 2.5A) has a faster asymmetric instability than other cases. It is ~ 0.11 Myr faster and ~ 3 K warmer than that of 498 kJ/mol with $R_s = 3$. Above 800 kJ/mol (e.g. 850 kJ/mol with $R_s = 3$, see Figure 2.5B) the asymmetric feature is not produced perhaps because of too low a plastic strain rate. Even though the time domain is expanded up to 2 Myr (see Figure 2.5B-c), it is difficult to generate shear heating with attendant shear localization due to the large activation energy. It has been shown that the lower the activation energy, the earlier the initiation of asymmetric instability. This is similar to what was found for listric faults (Regenauer-Lieb et al. 2004); so I can conclude that strong shear localization is facilitated by a small activation energy.

In order to ensure the reliability of my calculation, I perform end-member modeling with the activation energy of 200, 498 and 800 kJ/mol under same

R_s . Figure 2.6a is temperature profile at 1 Myr with different 200, 498 and 800 kJ/mol activation energies. The case of lower activation energy (i.e. 200 kJ/mol) induces a stronger instability. On the other hand, the maximum temperature is higher for low activation energy. Another interesting aspect of Figure 2.6a is that the region of high temperature (the location of shear localization) becomes more localized for lower activation energy. The localization width is about twice as wide for strong than for weak activation energy. The narrower shear localization is more favorable weak zone for mechanical break-off. The depth of maximum temperature has a tendency to go deeper with decreasing activation energy. This suggests that more asymmetric deformation occurs with smaller activation energy. Stronger asymmetric instability due to lower activation energy induces larger plastic deformation along the interface. The stress guides underthrusts deeper (~ 90 km and ~ 60 km in cases of 200 kJ/mol and 800 kJ/mol activation energies, respectively), when a stiffer lithosphere is underthrusting toward a soft lithosphere. The green line referring realistic activation energy (498 kJ/mol) of olivine (Chopra and Paterson, 1981) lies between the strong (800 kJ/mol) and weak (200 kJ/mol) cases. Thus, this finding lends confidence to this end-member investigation.

In Figure 2.6.b, temperature profiles along the interface at 1 Myr with 498 kJ/mol activation energy are plotted for $R_s = 2$ to 20. For $R_s = 1$, asymmetric instability is not observed. The maximum temperature becomes higher with increasing R_s . Figure 2.6.c is a close-up shot of Figure 2.6.b. A strong instability develops for high R_s value. However, the variation of temperature rising with increasing R_s is just 1 K. I need to discuss further this small temperature change, which is growing consistently with increasing R_s .

In my two-dimensional simulation I find a small temperature increase; this result is in contrast to Ogawa's classical one-dimensional model. Ogawa (1987) reported that temperature arises up to 100-400 K, which is enough to melt subducting materials, leading to deep focus earthquake. However, this huge temperature increase is caused by long time span (i.e. more than 100

Myr) with a suppressed heat advection due to 1D nature. In this context, it is easy to imagine that high temperature anomalies in a shear zone are required for large deformation. However, considering the heat flow paradox in large strike-slip fault zone, no sharp anomaly in heat flow is observed in spite of very fast and significant fault movement (Brune et al. 1969; Lachenbruch and Sass, 1992). Brune et al. (1993) stated that large instabilities can occur without substantially strength drop or temperature growing in the lithosphere, if the stress that is perpendicular to the boundary varies spatially and changes temporarily. The key focus of my study is not only the analysis of heating in the shear zone, but also heterogeneous stress distribution change caused by the shear modulus contrast. In brief, shear modulus contrast causes both higher temperature in shear zones and larger stress differences around the boundary, which enhances initiation of the weak zone. I propose that heterogeneous stress distribution around the interface of bi-material lithosphere due to larger shear modulus contrast causes:

i) The asymmetric instability

ii) The weak zone which induces large deformation

These two points mean that this mechanism can cause large instability in the latter stage because of larger stress difference and the positive thermal-mechanical positive effect (Hobbs et al. 2010), although the temperature increase is smaller (less than 1 K, in Figure 2.6.c) with increasing shear modulus contrast.

The occurrence of asymmetric instability with activation energy and R_s has been mapped out (Figure 2.7). To validate my findings, I have employed a grid set composed of R_s and activation energy for delineating the extents of each mode. The increments are 0.5 and 50 kJ/mol for R_s and activation energy, respectively. In Figure 2.7, three different modes, S (Stable; red zone), FU (Fast Unstable; green zone) and SU (Slow Unstable; blue zone), are defined. S mode is the case that there is no asymmetric shear instability during the calculation (see Figure 2.2). Because of the high activation energy and the low

shear modulus contrast, no asymmetric shear instability occurs, even though the geological time is lengthened up to 4 Myr. The region of S modes indicates that the required R_s for asymmetric instability is larger than 1.7 even with zero activation energy. Additionally, no asymmetric instability occurs when activation energy is higher than 850 kJ/mol. The value of 850 kJ/mol corresponds to a lithosphere too stiff for promoting sufficiently large plastic strain.

FU and SU modes represent the cases that have an apparent asymmetric shear instability. However, the time for the maturing shear instability, which refers to the time when temperature increment is 2 K greater than compared with the initial state, differs with R_s and activation energy. I define the FU mode that the time for maturing is faster than 1 Myr. Conversely, the SU mode indicates that the maturing time is slower than 1 Myr. The notable aspect in these two unstable modes is the big difference in the areas covered by each mode. The large territory of FU mode suggests that R_s has a dominant effect on the speed of instability development. In short, fast timescale asymmetric instability ($< 1\text{Myr}$) is generated under wide range of activation energy and can be controlled by a sufficiently large shear modulus contrast.

This asymmetric bi-material instability occurs because of a substantial difference in shear moduli of continental and oceanic lithospheres, where the change in applied forces and torques at the boundary leads to asymmetric bi-material viscoelastic instability. The distortion and larger differential stress eventually leads to shear localization. According to my results, a large shear modulus contrast facilitates the development of lithospheric necking and fault instability.

I have not ruled out that the bi-material instability may come from density contrast between stiff and soft lithospheres, not only from shear modulus contrast, as discussed in previous study (e.g. Nikolaeva et al. 2010). However, in my model with a short duration of calculation, I have not included the density contrast between stiff and soft lithosphere within the framework of a visco-elasto-plastic rheology. In further study using a more complete

numerical set-up both shear modulus and density contrasts between stiff and soft lithospheres will be required to unravel the fundamental causes of the bi-material instability and its implications for geodynamics. State variable change (e.g. pressure and temperature) and phase transition cause not only shear modulus change, but also sharp density variation (Lee, 2003). I should consider both shear modulus and density contrast taken together.

2.3.2. Effects from other aspects of lithosphere on the instability

To investigate additional features of asymmetric shear instability developed in realistic nature, the simple geothermal gradient and the difference of yield strength between stiff and soft lithospheres are employed to my model. Previous studies (Ogawa, 1987; Regenauer-Lieb and Yuen, 1998) have used initially a constant temperature distribution to observe pure effect of predefined shearing boundary condition and geometrical perturbation such as notched zone. Consistently, I also have employed constant temperature distribution in my study. However, the rheology depends significantly on temperature and thus a depth-dependent temperature must be introduced. Additionally, the deviatoric stress for plastic yielding may be different in stiff and soft lithospheres. Low yield strength is prescribed to the soft lithosphere, and vice versa. On the other hands, Poisson's ratio is also an important elastic property, which may influence on the asymmetric shear instability.

2.3.2.1. The difference in yield strength of bi-material lithosphere

Many previous studies (e.g. Andrews et al. 2009) have suggested that the yield strength of the lithosphere controls the ultimate fate of deformation and large-scale motion. Although my main aim is to investigate the asymmetric shear instability from shear modulus contrast in a bi-material lithosphere, distinguishing the influence of shear modulus contrast and yield strength difference in bi-material lithosphere is an important issue. Figure 2.8 shows the shape of deformation and the shear instability at 1 Myr in cases that different yield strength and the same shear modulus (i.e. $R_s = 1$) are prescribed. The shear instability and the deformation appear to be localized in the soft

part (see Figure 2.8). This also shows a strong asymmetry, but the shape is completely different with models with same yield strength and different shear moduli. Relatively small difference of yield strength, even just few percent, can trigger the shear instability. The deviatoric stress level reaches more quickly to yield strength in the lithosphere of lower yield strength; it leads to single set of shear zone in soft lithosphere. The elevated height on the top surface is plotted in Figure 2.9. I can recognize that the deformation is sharper and more uplifted with a larger difference of yield strength between two lithospheres in Figure 2.9. The different feature compared to the instability from shear modulus contrast is that the strength of the instability is weaker, for a larger difference in the yield strength. In cases of the instability from shear modulus contrast, higher shear modulus contrast induces stronger instability. The soft lithosphere with the weaker yield strength develops much more quickly the plastic strain. It means that less elastic energy is stored due to the lower yield strength. This result can be the important key for revealing on heat flow paradox, which was first proposed by Brune et al. (1969). Heat flow paradox is an enigmatic geophysical phenomenon, questioning why heat flow is very low in a narrow zone, where large shear heating is expected such as San Andreas Fault and subduction areas. I propose that the large difference in yield strength in bi-material induces large deformation (See Figure 2.9a), but a lower temperature in the shear zone (see Figure 2.8a). It can be one plausible reason for the heat flow paradox.

I have performed modeling with both differences in yield strength and shear moduli of bi-material lithosphere in order to understand the interaction between two elements. Figure 2.10 shows the results of the cases with $R_s = 3$ and varying the difference in yield strength. The yield strength of 100 MPa for stiff part is constantly applied, and the yield strength of soft part is changed (i.e. 10, 50, 90 and 100 MPa). The asymmetric instability due to the yield strength difference (similar features in Figure 2.8a) is predominant, when its value is greater than around 10 MPa. Otherwise, the asymmetric instability from R_s prevails (similar with Figure 2.3c), if the yield strength difference is smaller than about 10 MPa. Figure 2.10 is associated with the coupling

between the yield strength difference and R_s . Figure 2.10.a show definitely the asymmetric instability from yield strength contrast. Otherwise Figure 2.10.c and 10.d indicate the transient feature and fully R_s dominant feature, respectively. According to balancing between the yield strength difference and R_s in bi-material lithosphere under compression or extension, I determined the shape of asymmetric instability. One feature I noticed is that the initiation time and the strength of the instability are faster and weaker, respectively, when the higher yield strength difference is prescribed. This result is expected because a lower yield strength allows the material to give away quickly and not to store a large amount of elastic energy.

The fundamental difference in shear moduli has an important implication on shear instability in bi-material lithosphere. Considering separately the yield strength difference in bi-material, I must also look at yield strength contrast in terms of the timing of plastic yielding for the different materials.

2.3.2.2. Effect from a geothermal gradient

The lithosphere is not thermally constant and has a temperature-dependent rheology. Thus it is reasonable to test the effect coming from a simple geothermal gradient. As mentioned previously, my aim is to investigate pure effect of shear modulus contrast. Within this context, I have used a uniform temperature distribution, which is similar to that employed by Regenauer-Lieb and Yuen (1998). In that study by Regenauer-Lieb and Yuen, they already confirmed that depth-dependent temperature has minor effect in the case of the releasing of stored elastic energy with fast timescale. However, checking out the effect of geothermal gradient is important to emphasize the effect of shear modulus contrast. Therefore, the model with a simple linear gradient, from 273 K (the top) to a1273 K (the bottom), is calculated under 498 kJ/mol activation energy and $R_s = 3$.

The left column of Figure 2.11 (i.e. Figure 2.11.a, b, c) is showing the influence of asymmetric instability with the geothermal gradient. The right

column (i.e. Figure 2.11.d, e, f), otherwise, represents the case with a uniform temperature. The temperature distributions of initial stage and 1 Myr are plotted in Figure 2.11.a and 11.b, respectively. Due to asymmetric instability, the temperature field is perturbed at both top and the bottom (see Figure 2.11.b), similarly with Figure 2.11.e. In terms of equivalent plastic strain, the general shape with and without the gradient are almost the same except for the strength. A slightly higher shear instability is observed in Figure 2.11.c than that in Figure 2.11.f, which indicates that high temperature in lower part of lithosphere promotes the development of plastic strain. In addition, the initiation times of the asymmetric instability are very similar in these two cases (i.e. around 0.34 Myr with or without the geothermal gradient).

2.3.2.3. Variation of the Poisson ratio for whole lithosphere

The Poisson ratio is also an important material characteristic, which can be varied by water content and volatile and less by varying by pressure and temperature. I have performed modeling using same Poisson ratio (i.e. 0.3), but the effect of Poisson ratio on asymmetric shear instability must be investigated. The models with Poisson ratios (e.g. 0.25, 0.3 and 0.37) are calculated under $R_s = 3$. The results show that Poisson ratios have a minor effect on the strength and the initiation time of the asymmetric shear instability. However, the magnitude of deformation after asymmetric instability differs dramatically with changing Poisson ratio and also in dimensionality. In Figure 2.12, the smaller Poisson ratio has a tendency to induce larger deformation on the top surface. Dashed lines in Figure 2.12 represent the elevation on the top surface at 0.1 Myr, which occurs before occurrence of the asymmetric instability. After generating and maturing of the asymmetric instability, the elevations rise quickly.

2.4. Conclusions

I have shown that the asymmetric instability can develop from shear modulus contrast of a bi-material by using a series of high-resolution finite-element simulations with a Lagrangian mesh. Such an asymmetric instability

can generate a localized shear zone around the interface of stiff and soft crusts. The shear zone plays an important role as a weak zone and may lead to lithospheric scale break-off (e.g. Gerya et al. 2004). The higher the shear modulus contrast, the more likely asymmetric instability and deformation will be produced. I find that the thermally weak zone will develop more readily, when the activation energy is low and R_s is high. In particular, when $R > 1.7$ asymmetric instability will develop over a wide range of activation energy from 0 to 800 kJ/mol.

My study finds that the shear localization leading to generation of a weak zone may start as early as 1 Myr after plate convergence. Using the same activation energy as Regenauer-Lieb and Yuen (1998), the initiation times of shear localization in this study and previous work (Regenauer-Lieb and Yuen, 1998) are 0.25-0.53 (with varying R_s from 20 to 1) and 0.725 Myr, respectively. The work of Regenauer-Lieb and Yuen (1998) had a notched zone, which refers the brittle fault in the top surface of the lithosphere; their work suggested that brittle fault triggers shear instability through the entire lithosphere. However, my model without a predefined notched zone also reveals asymmetric shear instability, which indicates that predefined shear modulus contrast can trigger the instability in the whole lithosphere. Moreover, the initiation of shear instability in my study is faster than previous work (i.e. Regenauer-Lieb and Yuen, 1998). This result strongly suggests that shear modulus contrast has also important effect on shear instability generation. Moreover, the geometrical instability is completely asymmetric along the boundary, which can explain severe convoluted deformation around plate boundaries.

The development of asymmetric instability from variations in the lithospheric shear modulus is useful for explaining geological phenomena such as subduction initiation. Contrast in elastic parameters in the lithosphere is essential in the development of instability over short timescales. In addition to inherent mineralogical difference between continental and oceanic lithospheres, mineralogical phase transition (Dalguer and Day, 2009) can

cause significant shear modulus change and consequent bi-material shear instability can be generated.

2.5. References

- Anderson, O. L., D. Isaak, and H. Oda (1992), High-temperature elastic constant data on minerals relevant to geophysics, *Rev. Geophys.*, 30(1), 57–90, doi:10.1029/91RG02810.
- Andrews, E. R. and M. I. Billen (2009), Rheologic controls on the dynamics of slab detachment, *Tectonophysics* 464(1-4), 60-69.
- Adams, G. G. (1995), Self-excited oscillations of two elastic half-spaces sliding with a constant coefficient of friction, *J. Appl. Mech.* 62, pp. 867–872.
- Ben-Zion, Y. (2001), Dynamic ruptures in recent models of earthquake faults. *Journal of the Mechanics and Physics of Solids.* 49(9), pp. 2209-2244.
- Ben-Zion, Y., and Shi, Z. (2005), Dynamic rupture on a material interface with spontaneous generation of plastic strain in the bulk, *Earth and Planetary Science Letters*, 236, pp. 486-496.
- Ben-Zion, Y. (2012), Episodic tremor and slip on a frictional interface with critical zero weakening in elastic solid, *Geophys. J. Int.*, doi: 10.1111/j.1365-246X.2012.05422.x.
- Berckhemer, H., W. Kampfmann, et al. (1982), Shear modulus and Q of forsterite and dunite near partial melting from forced-oscillation experiments. *Physics of the Earth and Planetary Interiors*, 29(1), pp. 30-41.
- Billen, M.I., M. Gurnis (2001), A low viscosity wedge in subduction zones, *Earth and Planetary Science Letters.* 193, pp. 227–236.
- Billen, M. I. (2008), Modeling the Dynamics of Subducting Slabs, *Annual Review of Earth and Planetary Sciences.* 36(1), pp. 325-356.

- Bina, C. R. and G. R. Helffrich, (1992), Calculation of Elastic Properties from Thermodynamic Equation of State Principles, *Annual Review of Earth and Planetary Sciences*, 20(1), pp. 527-552.
- Branlund, J. M., K. Regenauer-Lieb, et al. (2001), Weak zone formation for initiation subduction from thermal-mechanical feedback of low-temperature plasticity, *Earth and Planetary Science Letters*, 190, pp. 237-250.
- Brietzke, G. B. and Y. Ben-Zion (2006), Examining tendencies of in-plane rupture to migrate to material interfaces, *Geophysical Journal International*, 167(2), pp. 807-819.
- Brune, J. N., T. L. Henyey, and R. F. Roy (1969), Heat Flow, Stress, and Rate of Slip along the San Andreas Fault, California, *J. Geophys. Res.*, 74(15), 3821–3827, doi:10.1029/JB074i015p03821.
- Brune, J. N., S. Brown, and P. A. Johnson (1993), Rupture mechanism and interface separation in foam rubber models of earthquakes: a possible solution to the heat flow paradox and the paradox of large overthrusts, *Tectonophysics*, 218, pp. 59-67
- Capitanio, F.A., Morra, G., Goes, S. (2007), Dynamic models of downgoing plate buoyancy driven subduction: subduction motions and energy dissipation, *Earth and Planetary Science Letters*, 262, 284-297.
- Chopra, P. N. and M. S. Paterson (1981), The experimental deformation of dunite. *Tectonophysics*, 78(1-4), pp. 453-473.
- Constantinescu, E. M. and A. Sandu (2010), Extrapolated implicit-explicit time stepping, *SIAM Journal of Scientific Computing* **31**(6), pp. 4452-4477.
- Dalguer, L. A., and S. M. Day (2009), Asymmetric rupture of large aspect-ratio faults at bi-material interface in 3D, *Geophysical Research Letters*, 36, L23307, doi:10.1029/2009GL040303.

- Doin, M.-P. and P. Henry (2001), Subduction initiation and continental crust recycling: the roles of rheology and eclogitization, *Tectonophysics*, 342(1-2), pp. 163-191.
- Fukuyama, E. and Madariaga, R. (1998), Rupture dynamics of a planar fault in a 3D elastic medium: rate- and slip-weakening friction, *Bull. seism. Soc. Am.*, Vol.88, 1-17.
- Gerya, T.V., Yuen, D.A. and W. V. Maresch, (2004), Thermomechanical modelling of slab detachment, *Earth and Planetary Sci. Lett.*, 226, 101-116.
- Glen, J. W. (1955), The Creep of Polycrystalline Ice, *Proceedings of the Royal Society of London. Series A, Mathematical and Physical Sciences*, Volume 228, Issue 1175, pp. 519-538.
- Goldsby, D. L., and T. E. Tullis (2002), Low frictional strength of quartz rocks at subseismic slip rates, *Geophysical Research Letters*, **29**(17), 1844, doi:10.1029/2002GL015240.
- Gurnis, M., Eloy, C., and Zhong, S. (1996), Free-surface formulation of mantle convection—II. Implications for subduction zone observables, *Geophysical Journal International*, 127, pp. 719–727.
- Hacker, B. R., G. A. Abers, and S. M. Peacock (2003), Subduction factory 1. Theoretical mineralogy, densities, seismic wave speeds, and H₂O contents, *Journal of Geophysical Research*, 108(B1), 2029, doi:10.1029/2001JB001127.
- Henderson, P., Henderson, G. M. (2009), *Earth Science Data*, Cambridge University Press.
- Hibbit, Karlsson and Sorenson Inc. (2009), *Abaqus/Standard User's Manual Version 6.9*, Vol. 1.
- Hill, R. (1952), The elastic behavior of crystalline aggregates, *Philos. Trans. R. Soc. London, Ser. A*, 65, 349–354.

- Hobbs, B., K. Regenauer-lieb, et al. (2010), Folding with thermal mechanical feedback: Another reply, *Journal of Structural Geology*, 32(1), pp. 131-134.
- Huismans, R. S., Beaumont, C. (2002), Asymmetric lithospheric extension: The role of frictional plastic strain softening inferred from numerical experiments, *Geology*, 30, pp.211-214.
- Hutter, K. (1983), *Theoretical Glaciology: Material Science of Ice and the Mechanics of Glaciers and Ice Sheets (Mathematical Approaches to Geophysics)*, Springer Verlag.
- Jackson, I. N. S. and R. C. Liebermann (1974), Melting and elastic shear instability of alkali halides, *Journal of Physics and Chemistry of Solids*, 35(9), pp. 1115-1119.
- Kameyama, M.C., D. A. Yuen, and H. Fujimoto (1997), The interaction of viscous heating with grain-size dependent rheology in the formation of localized slip zones. *Geophysical Research Letters*, 24, pp. 2523-2526.
- Karato, S., C. Dupas-Bruzek, et al. (1998), Plastic deformation of silicate spinel under the transition-zone conditions of the Earth's mantle, *Nature*, 395(6699), pp. 266-26.
- Karato, S., (2008), *Deformation of Earth Materials: An Introduction to the Rheology of Solid Earth*, Cambridge University Press.
- Kaus, B. J. P., and Y. Y. Podladchikov (2006), Initiation of localized shear zones in viscoelastoplastic rocks, *J. Geophys.Res.*, 111, B04412, doi:10.1029/2005JB003652.
- Kennedy, C. A. and M. H. Carpenter (2003), Additive Runge–Kutta schemes for convection–diffusion–reaction equations, *Applied Numerical Mathematics*, 44, pp. 139-181.
- Lachenbruch, AH. and Sass, J.H. (1992). Heat flow from Cajon Pass, Fault strength, and tectonic implications, *Journal of Geophysical Research*, 97

(B4), pp. 4995-5030.

- Lee, C.-T. A. (2003), Compositional variation of density and seismic velocities in natural peridotites at STP conditions: Implications for seismic imaging of compositional heterogeneities in the upper mantle, *Journal of Geophysical Research*, **108**(B9): 2441.
- Levander, A., C. A. Zelt, et al. (2007), Crust and Lithospheric Structure—Active Source Studies of Crust and Lithospheric Structure, *Treatise on Geophysics*, 1, pp. 247-288.
- Mizoguchi, K., T. Hirose, T. Shimamoto, and E. Fukuyama (2006), Moisture-related weakening and strengthening of a fault activated at seismic slip rates, *Geophysical Research Letters*, 33, L16319, doi:10.1029/2006GL026980.
- Moresi, L.N., Solomatov, V. (1998), Mantle convection with a brittle lithosphere: thoughts on the global tectonic styles of the earth and venus, *Geophysical Journal International* 133, 669–682.
- Nikolaeva, K., T. V. Gerya, and F. O. Marques (2010), Subduction initiation at passive margins: Numerical modeling, *Journal of Geophysical Research*, 115, B03406.
- Obata, M. and S.-I. Karato (1995), Ultramafic pseudotachylite from the Balmuccia peridotite, Ivrea-Verbano zone, northern Italy, *Tectonophysics*, 242(3-4), pp. 313-328.
- Ogawa, M. (1987), Shear instability in a viscoelastic material as the cause of deep focus earthquakes, *Journal of Geophysical Research*, 92, 13801–13810.
- OzBench, M., K. Regenauer-Lieb, et al. (2008), A model comparison study of large-scale mantle-lithosphere dynamics driven by subduction. *Physics of the Earth and Planetary Interiors*, 171(1-4), pp. 224-234.
- So, B.-D., Yuen, D.A., and Lee, S.-M. (2011), The Importance of Using

Explicit and then Implicit Schemes in the Fast time-scale Rupturing at Oceanic-Continental Boundary, 2011 AGU Fall Meeting, abstract T33C-2432.

Stølen, S. and R. G. Trønnes (2007), The perovskite to post-perovskite transition in CaIrO₃: Clapeyron slope and changes in bulk and shear moduli by density functional theory, *Physics of the Earth and Planetary Interiors*, 164(1-2), pp. 50-62.

Regenauer-Lieb, K., and D. A. Yuen (1998), Rapid conversion of elastic energy into plastic shear heating during incipient necking of the lithosphere, *Geophysical Research Letters*, 25(14), 2737–2740, doi:10.1029/98GL02056.

Regenauer-Lieb, K., D.A. Yuen and J. Branlund (2001), The initiation of subduction: criticality by addition of water?, *Science*, 294 (5542), pp. 578–580.

Regenauer-Lieb, K., Hobbs, B., Ord, A. (2004), On the thermodynamics of listric faults, *Earth Planets and Space*, **56**(12), pp. 1111-1120.

Rosakis, A. J., O. Samudrala, et al. (1998), Intersonic crack propagation in bimaterial systems, *Journal of the Mechanics and Physics of Solids*, 46(10), pp. 1789-1814.

Toth, J., M. Gurnis (1998), Dynamics of subduction initiation at preexisting fault zones, *Journal of Geophysical Research*, 103(B8).

van der Hilst, R. D., S. Widiyantoro, et al. (1997), Evidence for deep mantle circulation from global tomography, *Nature*, 386(6625), pp. 578-584.

van Hunen, J. and M. B. Allen (2011), Continental collision and slab break-off: A comparison of 3-D numerical models with observations, *Earth and Planetary Science Letters*, 302(1-2), pp. 27-37.

- Weertman, J. (1980), Unstable slippage across a fault that separates elastic media of different elastic constant, *Journal of Geophysical Research*, 85(B3), pp. 1455–1461.
- Wentzovitch, R. M., B. B. Karki, et al. (2004), Thermoelastic Properties of MgSiO₃-perovskite: Insights on the Nature of the Earth's Lower Mantle, *Physical Review Letter*, 92(1), doi: 10.1103/PhysRevLett.92.018501
- Yamasaki, T., Seno, T. (2003), Double seismic zone and dehydration embrittlement of the subducting slab, *Journal of Geophysical Research*, 108(B4), 2212, doi:10.1029/ 2002JB001918.
- Yeganeh-Haeri, D. J. W., and E. Ito (1989), Elasticity of MgSiO₃ in the Perovskite Structure, *Science*. pp.787-789.
- Yoshimoto, K., H. Sato, et al. (1997), Short-wavelength crustal heterogeneities in the Nikko area, Central Japan, revealed from the three-component seismogram envelope analysis. *Physics of the Earth and Planetary Interiors*, 104(1-3), pp.63-73.
- Zhong, S., M. Gurnis (1995), Mantle convection with plates and mobile, faulted plate margins, *Science*, 267, pp. 838–843.

2.6. Figures

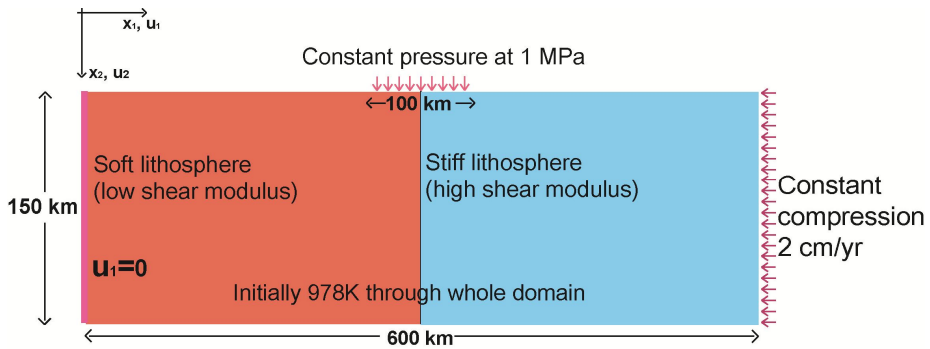


Figure 2.1. Domain of my 2D FEM model with a 600 km width and 150 km depth under the plane strain assumption. I have used 0.5 to 1 million elements with irregularly spaced grid points. Constant velocity boundary condition 2 cm/yr is imposed at right side boundary. Free surface boundary condition and zero horizontal velocity boundary condition are used at top and left boundary, respectively. The left and right portions have different elastic shear moduli. The left part with smaller shear modulus and the right part with larger shear modulus correspond to soft and stiff lithospheres, respectively. The boundary between the two different lithospheres has no frictional mechanism.

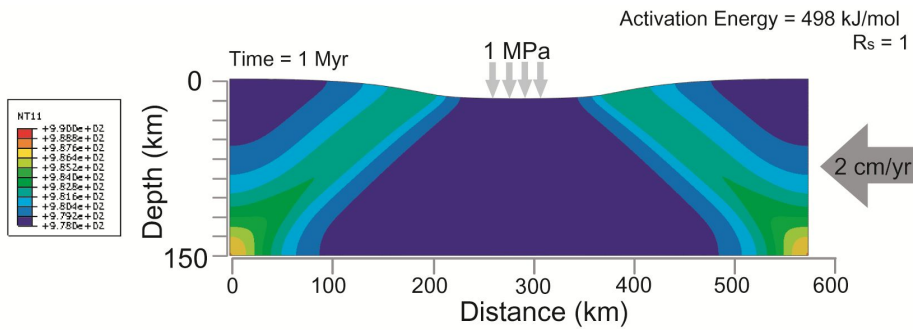


Figure 2.2. The rainbow color contours show the temperature distribution. Symmetric instability with same shear moduli in soft and stiff lithospheres occurs at 1 Myr. Symmetric thermal instability occurs in both parts because of the constant vertical pressure. Asymmetric deformation does not appear.

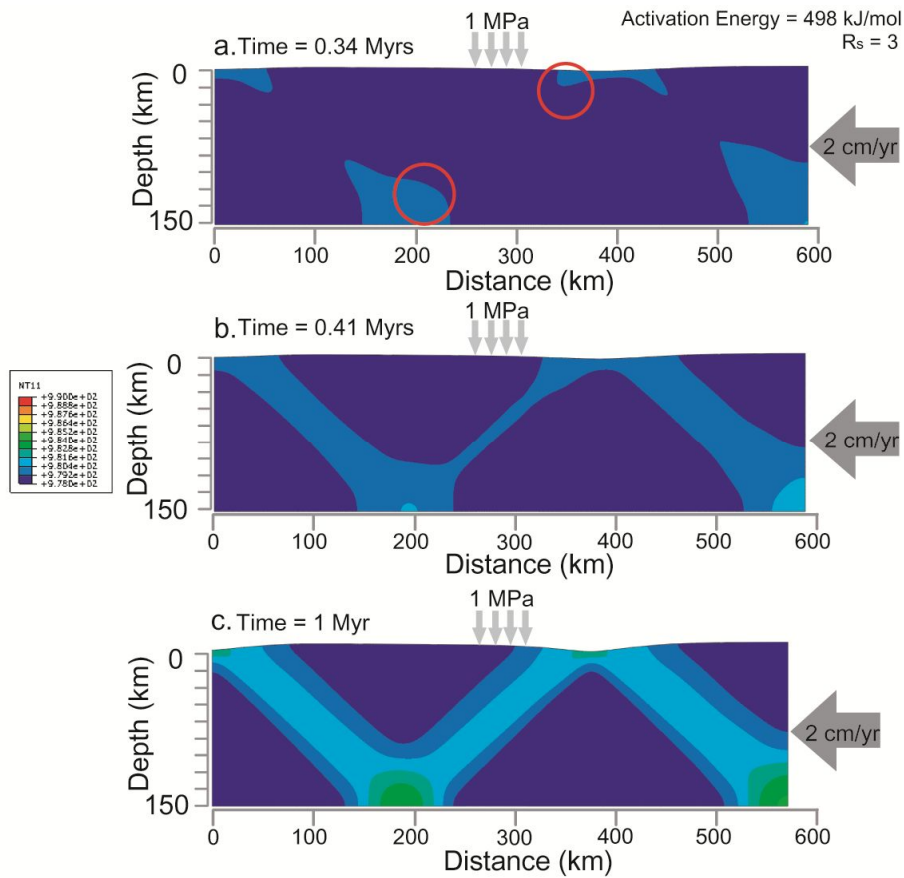


Figure 2.3. The rainbow color contour shows temperature distribution. **a.** Nucleation of asymmetric instability. The seeds for asymmetric instability (red circle) are nucleated on bottom and top of the domain at 0.34 Myr. **b.** Growing of asymmetric instability. The thermal instabilities from both and top run toward each other and merge in center at 0.41 Myr. Shear localization is clearly observed clearly. **c.** Maturing of asymmetric instability at 1 Myr. The asymmetric instability becomes stronger and stronger with time. This process matures and localizes the asymmetric instability.

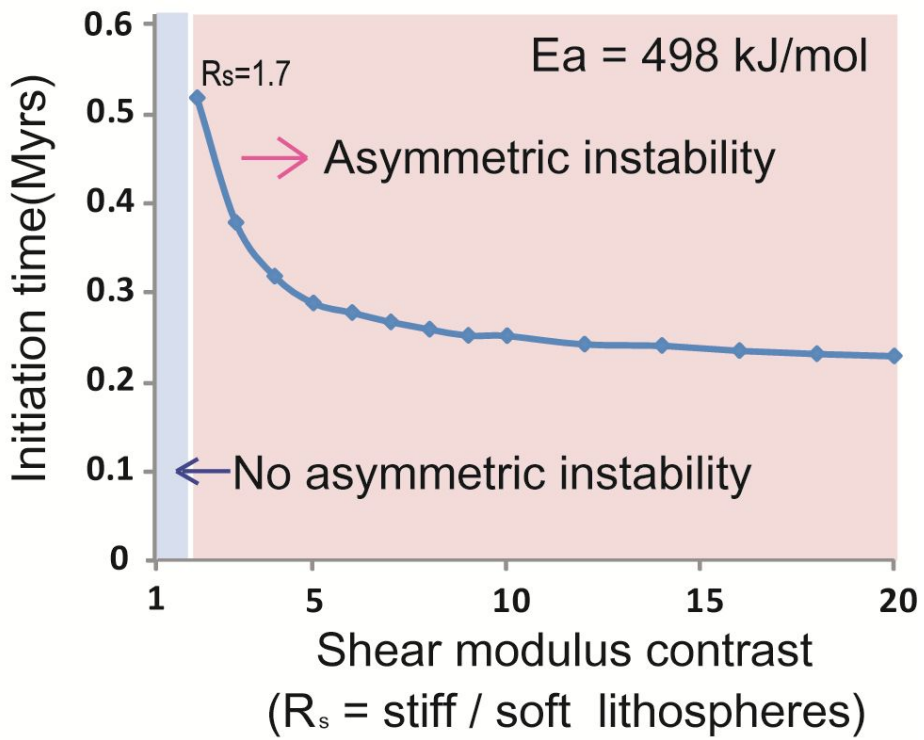


Figure 2.4. Initiation times of asymmetric instability with varying shear modulus contrast, R_s , from 1 to 20. No asymmetric instability occurs in the blue region with small shear modulus ratio.

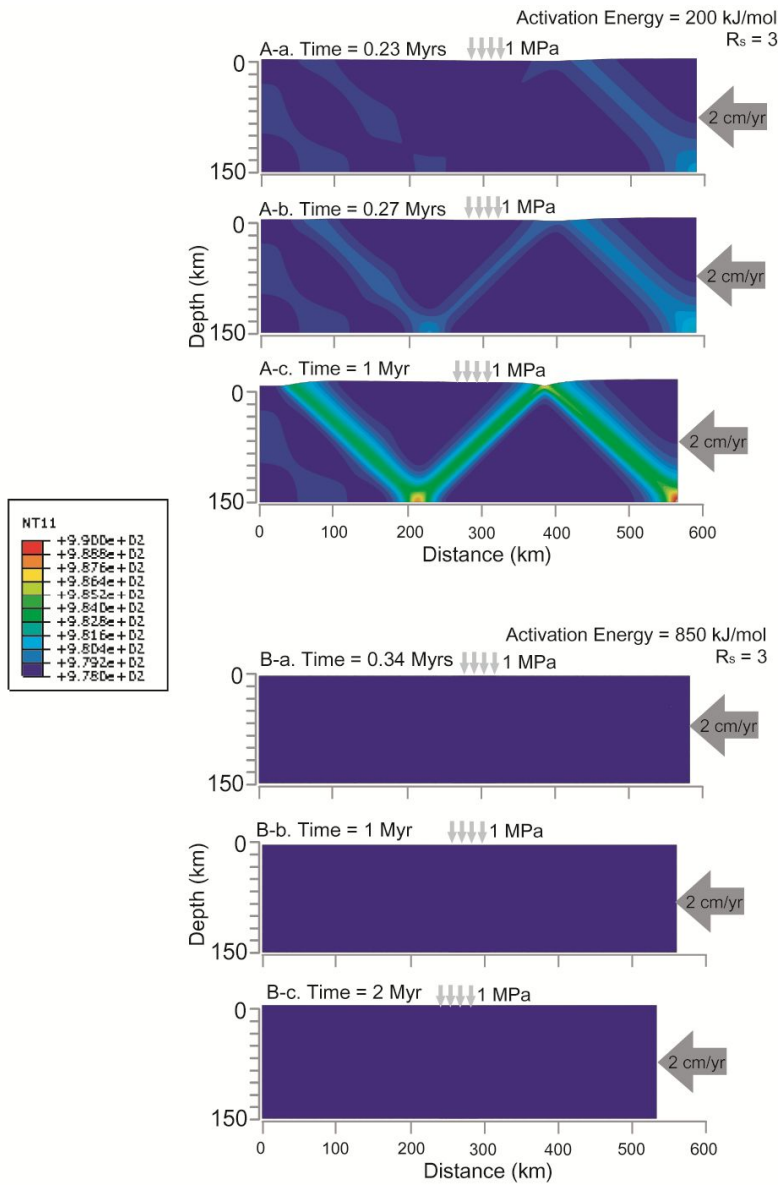


Figure 2.5A. a-c. The case of low activation energy (200 kJ/mol with $R_s = 3$). It shows that ~ 0.11 Myr faster and ~ 3 K hotter asymmetric instability develops than for the 498 kJ/mol model.

Figure 2.5B. a-.) Time history of temperature distribution in the calculating domain of the case of high activation energy (850 kJ/mol with $R_s = 3$). It shows just the elastic deformation rather than plastic deformation.

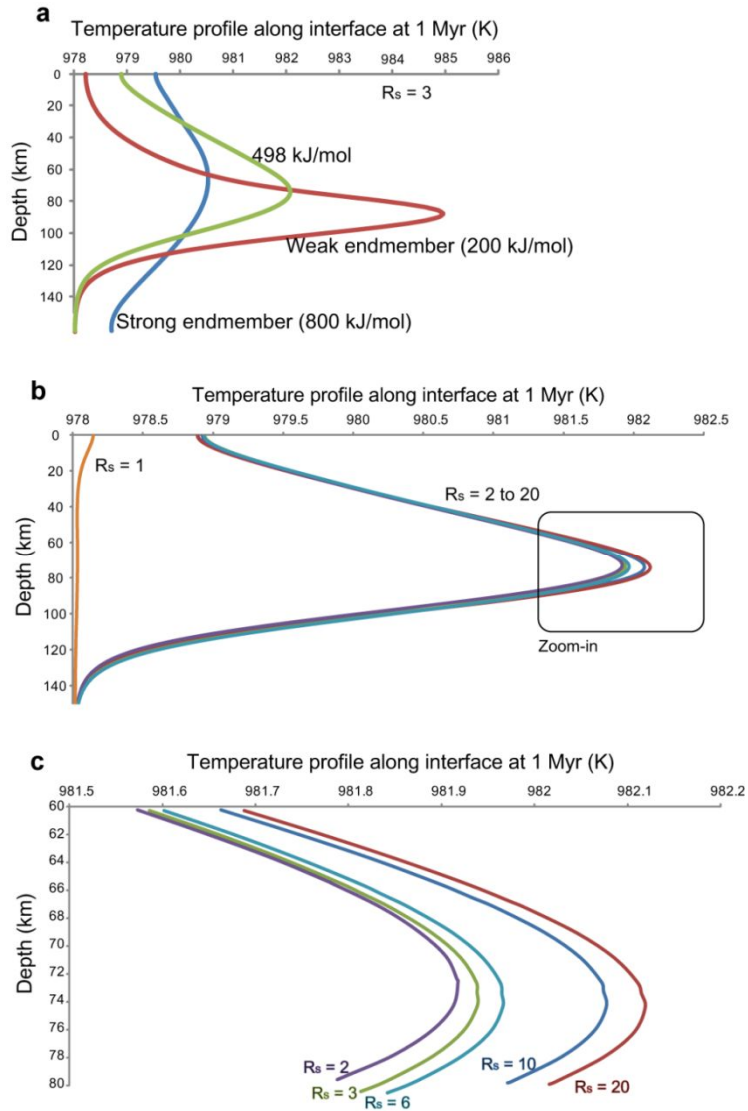


Figure 2.6. a. The temperature profile along interface at 1 Myr with varying activation energy and constant $R_s = 3$. Blue line is result from strong endmember (800 kJ/mol activation energy) and red line is that from weak endmember (200 kJ/mol activation energy). Green line shows realistic case with rheology of 498 kJ/mol activation energy. **b.** The temperature profile along interface with varying R_s , under 498 kJ/mol activation energy condition. The strength is varied with R_s . **c.** the zoomed-in temperature profiles at the center of instability.

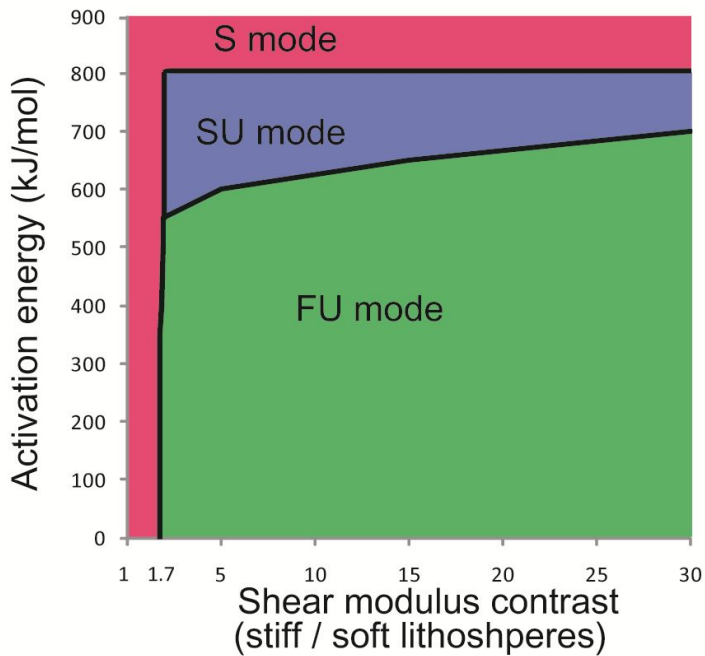


Figure 2.7. Domain map of asymmetric instability with parameterized activation energy and shear modulus contrast. S mode (red zone) means stable mode that no asymmetric instability despite of long timescale (4 Myr). The unstable group can be divided to two modes, FU (fast unstable; green zone) and SU (slow unstable; blue zone), in terms of the initiation time of asymmetric instability, before or after 1 Myr.

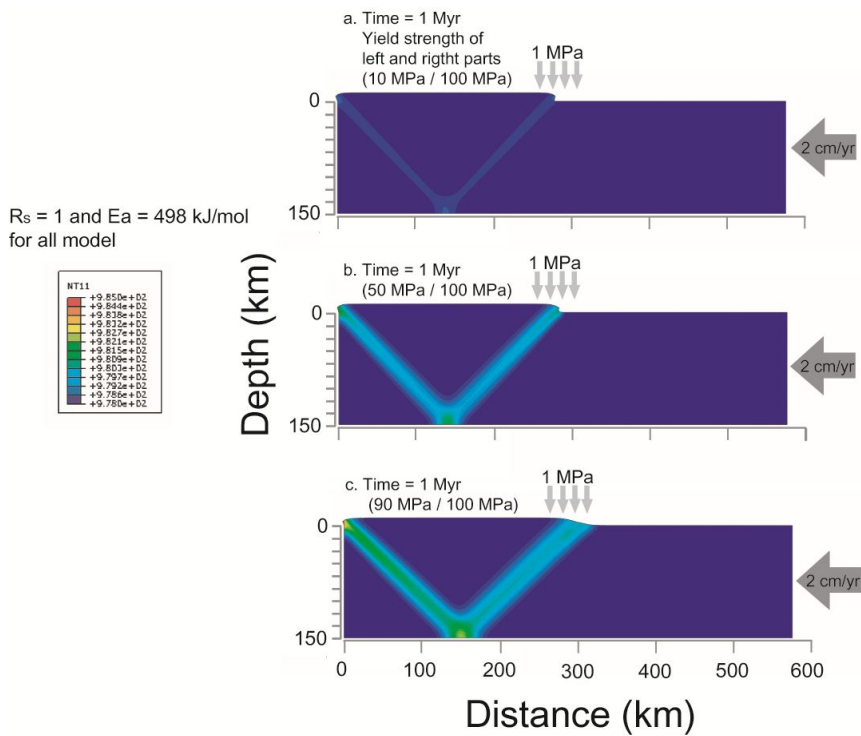


Figure 2.8. Shape of deformation and the shear instability at 1 Myr in cases with different yield strength. R_s and activation energy are fixed a 1 and 498 kJ/mol, respectively. **a.** Yield strength of left and right parts = 10 MPa / 100 MPa. **b.** 50 MPa / 100 MPa. **c.** 90 MPa / 100 MPa. All cases are consistently showing a single shear zone of the part with a lower yield strength.

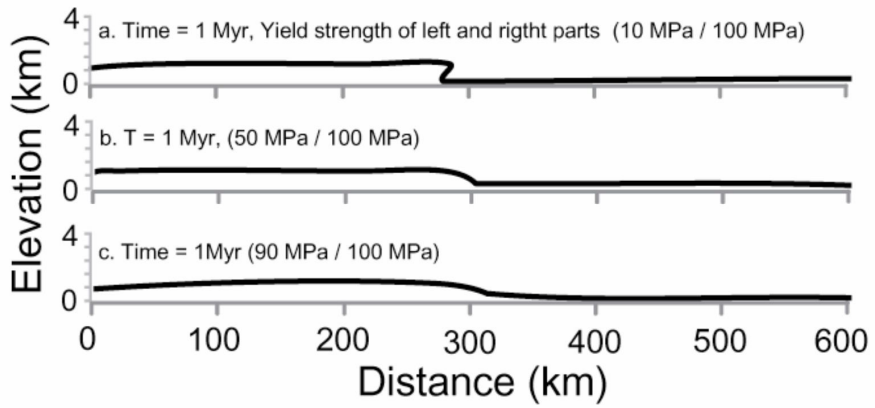


Figure 2.9. Elevated height on the top surface. **a.** Yield strength of left and right parts = 10 MPa / 100 MPa. **b.** 50 MPa / 100 MPa. **c.** 90 MPa / 100 MPa. The case of largest difference (i.e. case (a)) in yield strength shows the sharpest deformation of the top surface.

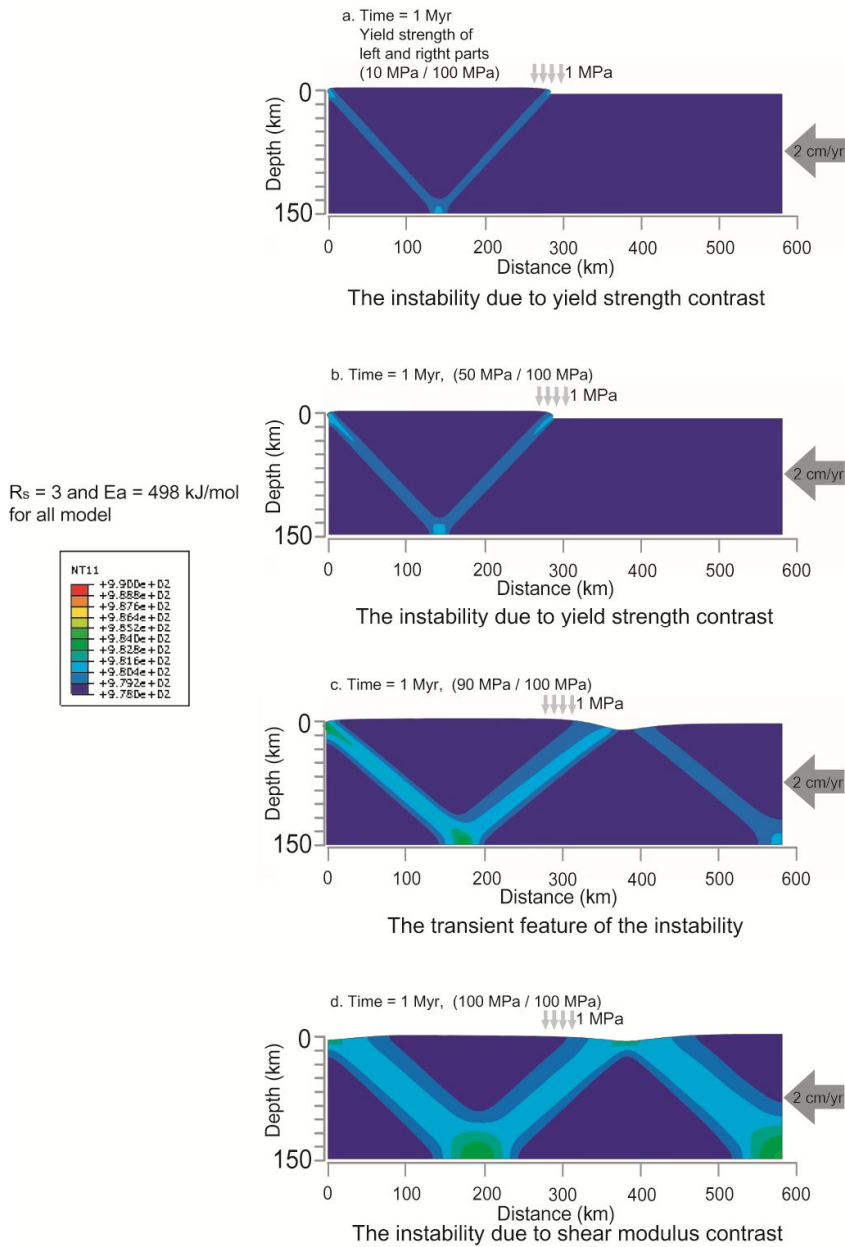


Figure 2.10. Shape of deformation and the shear instability at 1 Myr in cases with different yield strength. R_s and activation energy are fixed at 3 and 498 kJ/mol, respectively. **a.** Yield strength of left and right parts = 10 MPa / 100 MPa. **b.** 50 MPa / 100 MPa. **c.** 90 MPa / 100 MPa. **d.** 100 MPa / 100 MPa.

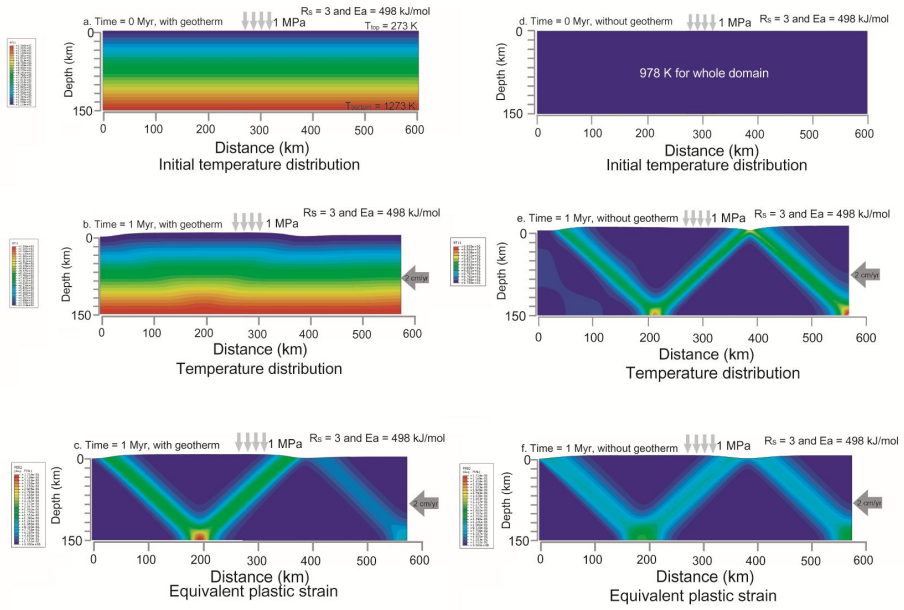


Figure 2.11. Comparison of the asymmetric instability between the cases with and without the geothermal gradient. The left and the right columns are showing the cases with and without the gradient, respectively. In terms of the magnitude of the plastic strain, two cases are similar.

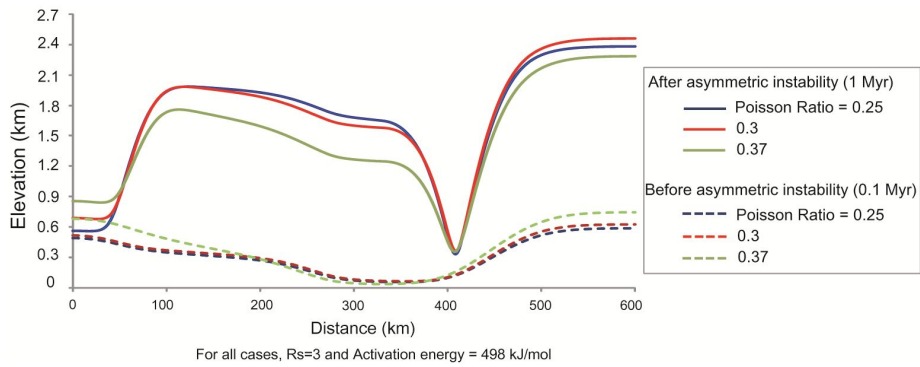


Figure 2.12. Comparison of the deformation on the top surface with varying Poisson ratio. Dashed line means the deformation for 0.37 (green line), 0.3 (red line) and 0.25 (blue line) of Poisson ratio before the asymmetric instability. Otherwise, solid lines refer to those after the occurrence of asymmetric instability.

2.7. Table

Table 1. Input parameters.

Parameters	Symbol	Values
Specific heat	c_p	1240 J/kg/K
Thermal conductivity	κ	3.4 W/m/K
Lithospheric density	ρ	3300 kg/m ³
Shear modulus	μ	Variable
Conversion efficiency from plastic work into shear heating	Ψ	0.9
Activation energy	Q	Variable
Gas constant	R	8.314 J/mol/K
Power law exponent	n	4.48
Prefactor	A	5.5×10^{-25} Pa·n·s
Yield strength	σ_y	100 MPa

Chapter 3

An Efficient Implicit-Explicit Adaptive Time-Stepping Scheme for Handling Multi-Timescale Geodynamical Problems in Lithospheric Shear Zone Development*

Abstract

Geodynamical problems associated with shear zone development in the lithosphere involve features of widely different timescales, since the gradual buildup of stress leads to rapid and localized shear instability. Such problems have a large stiffness in time domain and cannot be solved efficiently by a single time-integration scheme. This conundrum has forced us to use an adaptive time-stepping scheme, in particular, the adaptive time-stepping scheme (ATS) where the former is adopted for stages of quasi-static deformation and the latter for stages involving short timescale nonlinear feedback. To test the efficiency of this adaptive scheme, I compared it with implicit and explicit schemes for two different cases involving: (1) shear localization around the predefined notched zone and (2) asymmetric shear instability from a sharp elastic heterogeneity. The ATS resulted in a stronger localization of shear zone than the other two schemes. This is because either implicit or explicit schemes alone cannot properly simulate the shear heating due to a large discrepancy between rates of overall deformation and instability propagation around the shear zone. My comparative study shows that, while the overall patterns of the ATS are similar to those of a single time-stepping method, a finer temperature profile with greater magnitude can be obtained with the ATS. The ability to model an accurate temperature distribution around the shear zone may have important implications for more precise timing of shear rupturing, which is important in geodynamics.

Keyword: implicit scheme, explicit scheme, adaptive scheme, multi-timescale modeling, shear heating

* An edited version of this chapter is under “accepted” in *Geochemistry Geophysics Geosystems* in 2013.

3.1. Introduction

Lithospheric rupture is essential to plate tectonics, and yet many aspects of this crucial event are not well understood (e.g., Scholz, 2002). In particular, little is known about the initiation of shear zone, which acts as a weak zone within lithosphere near many large deformation zones. The understanding of the development of such a zone is essential to elucidate the cause of subduction initiations (Regenauer-Lieb et al., 2001) and slab detachments (Gerya et al., 2004). One of the favorite explanations for the development is that they begin by concentration of stress at a localized region and then grow by positive feedback between shear heating and reduction in material strength (e.g., Bercovici, 2002; Branlund et al., 2000; Hobbs et al., 2007). However, due to multiple-time and -spatial scales involved in this extremely nonlinear problem, the effective simulation of these features has always been a challenge.

The process that leads to lithospheric shear zone can in general be divided into three stages (see the cartoons in Figure 3.1). The stage 1 involves the buildup of stress by tectonic loading. In stage 2, plastic deformation starts to occur and then thermal instability develops within a narrow zone in the lithosphere. The stage 3 can be envisaged as a period where the temperature in the localized zone becomes stable as the heat generated at the zone is balanced by thermal diffusion (Kincaid and Silver, 1996).

A particular difficulty when simulating the development of shear zone is that it contains features with vastly different timescales and spatial scales. For instance, the entire domain where the force is being applied is substantially

large, whereas the area of significant deformation can be quite localized. Also during most of computing time of the numerical experiment, the whole region may deform steadily in the stages 1 and 3 mentioned above, which contrasts with the abrupt development of shear instability in the stage 2. Since there is a large difference in characteristic timescales for each stage, the numerical formulation is not easy and falls within the category of large stiffness problems (Dahlquist and Björck, 2008).

To resolve the large discrepancies in spatial scales, in recent years, more and more problems employ adaptive mesh refinement to calculate growing or moving instability (e.g., Stadler et al., 2010). However, for problems with large differences in timescales, there appears to be no simple solution. Up to now, most studies adopt a single time-stepping approach (i.e., implicit or explicit schemes). Employing a single scheme may be convenient, but as I shall demonstrate, it can miss short timescale features, which can be important for understanding the intricate physics around the localized zone.

As an attempt to handle the dilemma with different timescales, I propose the use of the implicit-explicit time-integration method (Brown, 2011; Constantinescu and Sandu, 2010). This method can be divided into two different kinds of schemes. One is implicit-explicit combined scheme, where the implicit and explicit schemes are respectively used for advection and diffusion terms (Constantinescu and Sandu, 2010). The second case is the adaptive scheme, which switches between implicit and explicit schemes when dominant timescales and mathematical stiffness are changed abruptly with time (Butcher, 1990; Hairer and Wanner, 2004). I have focused on the adaptive time-stepping scheme (ATS) where the former scheme is applied to slow deforming phase and the latter to fast propagation of the instability. By doing so, I exploit the advantages of each scheme.

The ATS has a potential to calculate multiple timescale phenomena. However, this approach has not been widely adopted in geodynamical simulations. In this study, I compare the ATS against the two previous investigations of the shear zone development (Regenauer-Lieb and Yuen,

1998; So et al., 2012) to see whether the ATS provides a better solution than previous approach using a single time-stepping method. In the case of Regenauer-Lieb and Yuen (1998) (hereinafter referred to as R model), instabilities are triggered around the predefined notched hole as a result of far-field extension, whereas So et al. (2012) (hereinafter referred to as S model) examined the development of asymmetric instability generated at the interface between the stiff and soft lithospheres by far-field compression. In addition, I conducted two benchmark tests to ensure that solutions obtained from my numerical techniques are consistent with a simple analytical solution (benchmark test I) and Ogawa's model (Ogawa, 1987).

My study shows that for modeling multi-scale problems the ATS approach is better than one based on a single time-stepping method in terms of its accuracy and ability to handle highly nonlinear thermal-mechanical feedback. In the two examples (Regenauer-Lieb and Yuen, 1998; So et al., 2012) that were considered, the results of the ATS show fine-scale features near the localized shear zone that were difficult to be observed using the implicit scheme alone.

3.2. General model setup

I used ABAQUS (Hibbit, Karlsson and Sorenson Inc., 2009) a finite element code which allows the user to prescribe either implicit or explicit time-stepping method. The solvers can be set to have the same order of accuracy for both approaches. The use of this particular code was necessary because the two previous studies (R and S models) employed the implicit scheme.

I assumed that the mass, momentum and energy are conserved within the system which is made up of a material whose strength is stress- and temperature-dependent (Glen, 1955; Karato, 2008). Equations 1-3 represent the continuity equation, objective Jaumann derivative of the stress tensor (Kaus and Podladchikov, 2006), and energy equation, respectively. D/Dt is the

material derivative.

$$\frac{\partial v_i}{\partial x_i} = 0 \quad (1)$$

$$\frac{D\tau_{ij}}{Dt} = \frac{\partial \tau_{ij}}{\partial t} + v_i \frac{\partial \tau_{ij}}{\partial x_i} - W_{ik} \tau_{kj} + \tau_{ik} W_{kj} \quad (2)$$

$$\rho c_P \frac{DT}{Dt} = \rho c_P \left[\frac{\partial T}{\partial t} + v_k \frac{\partial T}{\partial x_k} \right] = \frac{\partial}{\partial x_i} \left(k \frac{\partial T}{\partial x_i} \right) + \Psi \tau_{ij} \left[\dot{\epsilon}_{ij}^{total} - \frac{1}{2\mu} \frac{D\tau_{ij}}{Dt} \right] \quad (3)$$

$$W_{ij} = \frac{1}{2} \left[\frac{\partial v_i}{\partial x_j} - \frac{\partial v_j}{\partial x_i} \right] \quad (4)$$

where t is the time, x_i is the spatial coordinate along the i -direction and v_i is the velocity in i -direction. τ_{ij} and W_{ij} are deviatoric stress and spin rate tensors as defined by Equation 4, respectively. The detailed meaning and value of the parameters for different cases are listed in Table 1. Other information concerning the model, such as mesh size and initial condition, can be found in Table 2.

I also assumed that

$$\dot{\epsilon}_{ij}^{total} = \frac{1}{2} \left[\frac{\partial v_i}{\partial x_j} + \frac{\partial v_j}{\partial x_i} \right] \quad (5),$$

$$\dot{\epsilon}_{ij}^{total} = \dot{\epsilon}_{ij}^{elastic} + \dot{\epsilon}_{ij}^{inelastic} \quad (6),$$

$$\text{and } \dot{\epsilon}_{ij}^{elastic} = \frac{1}{2\mu} \frac{D\tau_{ij}}{Dt} \quad (7).$$

where $\dot{\epsilon}_{ij}^{total}$ (Equation 5) is total strain-rate tensor defined by the simple

sum of elastic and inelastic strain-rate tensors (Equation 6). The former can be expressed as in Equation 7, and μ denotes the elastic modulus such as the Young's (in the cases of Ogawa's and R model) or shear modulus (in the case of S model).

$$J_2 = \left(\frac{1}{2} \tau_{ij} \tau_{ij} \right)^{1/2} \quad (8)$$

$$\dot{\varepsilon}_{ij}^{inelastic} = A J_2^{n-1} \tau_{ij} \exp\left(-\frac{Q}{RT}\right) \quad (9)$$

Furthermore, when the second invariant of deviatoric stress tensor J_2 (Equation 8) of each node exceeds the predefined yield strength (σ_{yield}), the lithosphere is assumed to behave in an inelastic manner as a function of deviatoric stress and temperature (Equation 9). Moreover, this inelastic strain is converted into shear heating with a ratio of Ψ (See Equations 3 and 9). In this study, I use von Mises yield criterion with 100 MPa of finite yield strength. Both plastic deformation and frictional motion cause temperature elevation in the lithosphere. Rheologies for both mechanisms are different, but large plastic yield strength (~ 100 MPa) has been used to mimic a strong fault (Hale et al., 2010) which has a large frictional coefficient ($f \approx 0.7$) and may cause a great deal of heat generation.

3.3. Description of different numerical schemes

3.3.1 Explicit Scheme

The general mathematical formulation for the explicit scheme can be simply described as

$$\mathbf{u}|_{t+\Delta t} = \mathbf{f}(\mathbf{u}|_t) \quad (10).$$

In this scheme, the information on the next time-step $\mathbf{u}|_{t+\Delta t}$ comes directly from $\mathbf{u}|_t$ and the function \mathbf{f} which comes from the discretization of the partial differential equation for the system at hand (Griffiths and Higham, 2010). It is quite straightforward. However, the explicit scheme can become unstable because of the relationship between time-step and spatial mesh, and thus to avoid such ill behavior the size of time-step should obey a strict criterion according to numerical analysis (e.g., Dahlquist and Björck, 2008). Such restriction poses a severe problem in geodynamical modeling where the solution has to be integrated over a very long period of time in which case the implicit scheme must be used. However, the important advantage of the explicit scheme is that it is better than the implicit scheme in highly dynamic simulations (Iserles, 1996). For highly nonlinear stress-strain responses such as sliding, contact and faulting, the explicit scheme more efficiently handles the complexity and sharp field variables change than the implicit scheme (Nezo et al., 2011; Noels et al., 2004). This is because the implicit scheme may show a numerical divergence when calculating tangent stiffness matrix under small time-stepping (Wang et al., 1997; Sun et al., 2000). The small time-stepping in the implicit scheme for highly dynamic physics can be adopted, but the error tolerance should be relaxed for ensuring the convergence of stiffness matrix. In short, the explicit scheme is useful for treating problems whose timescale has the same order as the stability limit for time-stepping (Hulbert and Chung, 1996). The detailed formulation for the second order derivative of \mathbf{u} and the criterion for time-step are presented in Appendix A.1.

3.3.2 Implicit scheme

The implicit time-stepping scheme, on the other hand, can be expressed as below

$$\mathbf{u}|_{t+\Delta t}^i = \mathbf{f}(\mathbf{u}|_t^i, \mathbf{u}|_{t+\Delta t}^i) \quad (11).$$

where $\mathbf{u}|_{t+\Delta t}^i$ is the unknown (i.e., temperature or displacement at each node) at time $t + \Delta t$ at i^{th} iteration. \mathbf{f} is the discretized functional derived from partial differential equations. Unlike the explicit scheme, $\mathbf{u}|_{t+\Delta t}^i$ is calculated from both $\mathbf{u}|_t^i$ and $\mathbf{u}|_{t+\Delta t}^i$. $\mathbf{u}|_{t+\Delta t}^i$ is generally obtained using an iterative method which is continued until the difference between $\mathbf{u}|_{t+\Delta t}^i$ and $\mathbf{u}|_{t+\Delta t}^{i-1}$ becomes small enough to ensure local convergence. As mentioned previously, the main advantage of the implicit scheme is that rather large time-steps can be taken without worrying about the solution becoming unstable. However, its disadvantage is that it can often miss short timescale features and is not suitable for handling highly dynamic situations. The implicit scheme is the method of choice for relatively steady-state situation (King et al., 2010). A detailed description of the implicit scheme is provided in Appendix A.2.

3.3.3. ATS approach

Many geodynamical problems involve features with vast timescale differences and thus may not be suitable for solving them using either explicit or implicit approach. In the previous works on the shear localization in crystalline structure (e.g., Braeck and Podliadchikov, 2007) and bi-material interface (e.g., Langer et al., 2010), time-steps and schemes were varied to increase the accuracy of the calculations of highly nonlinear physics. However, there is no detailed investigation for an algorithm to determine the time-step and the time-integration scheme.

For these sets of problems, the adaptive time-stepping scheme (simply referred to as the ATS) can be a solution to these tough situations (e.g., Butcher, 1990; Hairer and Wanner, 2004). For instance, as mentioned above, the process of lithospheric shear zone development can be divided into different stages depending on the dominant physics (see Figure 3.1). The implicit scheme may be suitable for the stages 1 and 3 where the rate of deformation and change in temperature are relatively small and steady. On the

other hand, for the stage 2 where the change in temperature and material strength is relatively abrupt, the explicit scheme is a better approach.

Employing the ATS method is not a simple task. For instance, one has to consider when to change the scheme from one to the other and also make sure that momentum balance is maintained during this transition between two schemes. During the transition from the implicit scheme, the explicit scheme can produce an unrealistically large and fast deformation due to the failure in balancing external and internal forces. However, there is no unrealistically large deformation when I switch the implicit scheme into the explicit scheme, because the deformation rate of whole domain is similar with the imposed boundary condition.

In geodynamical problems dealing with shear heating, the velocity of shear instability propagation is much faster than the deformation rate (e.g., So et al., 2012). The deformation rate is relatively steady while the thermal instability is suddenly initiated and propagated. The lithospheric system is significantly influenced by the thermal event (i.e., shear heating) arisen from energy equation. Moreover, if I adopted the explicit scheme for momentum equation (see Equation (7) in Appendix A.1), the size of time-step is less than a second. This extremely small time-step costs too large computational expense. Therefore, I switch between the implicit and explicit schemes only for energy equation while keep the implicit scheme for momentum equation.

3.4. Benchmark tests

I should ideally compare the numerical results with analytical solution. However, in my problem where the momentum and energy equations are coupled through stress- and temperature-dependent nonlinear rheology, analytical solution to my best knowledge is not available. In order to demonstrate the strengths and weaknesses of individual schemes and reliability of my techniques in handling the problem of shear heating in the lithosphere, two benchmark tests were made. Benchmark test I is a case where

the numerical results of the implicit and explicit schemes are compared with the known analytical solution involving shear heating within purely viscous lithosphere with a temperature-dependent viscosity. Finally, I carry out benchmark test for Ogawa's model with numerical results from Ogawa (1987), which employed the explicit method.

3.4. 1. Benchmark test I

The steady-state analytical solution for a viscous fluid with the temperature-dependent viscosity was derived by Sukanek et al. (1973). Turcotte and Schubert (2001) extended the problem to include large geological scales. I compare the numerically generated solutions from the explicit and implicit schemes with the analytical solution. My results reflect that the explicit scheme is more appropriate for dealing with the shear deformation alongside strong feedback between the heating and material strength. Equations for benchmark test I and the detailed discussion are included in Appendix A.3.

3.4. 2. Ogawa's model

In this section, I compare the fourth order Runge-Kutta explicit method with the second order central difference and full Newtonian implicit schemes employed by ABAQUS for one-dimensional shear heating case. Figure 3.2.a is the schematic diagram for the original model by Ogawa (1987) where the cause of deep focus earthquake was explored as a result of shear instability within the subducting viscoelastic lithosphere. Stress- and temperature-dependent rheology was also assumed, and the deformation rate was set at a constant strain-rate of 10^{-13} s^{-1} . In addition, the magnitude of initial stress and temperature were prescribed as 400 MPa and 978 K, respectively. I have assigned the temperature perturbation around the lower boundary with a small amount of 10 K and a size of 0.1 km. This perturbation is applied to promote shear localization. Additional information for this benchmark test is in Tables 1 and 2. By demonstrating that the temperature in the shear zone can rise quickly up to additional 100–400 K, Ogawa (1987) deduced that shear heating

can be an efficient mechanism for triggering deep focus earthquakes.

The numerical experiment of Ogawa (1987) was repeated in this study using both schemes. Figure 3.2.b is the comparison among different approaches. The explicit scheme is much closer to the result by Ogawa (1987). Furthermore, the temperature evolutions at the shear zone predicted by the explicit and implicit schemes are different. In the early stage of viscous dissipation, the explicit and implicit schemes produce relatively similar outcome. However, in the latter stage, temperature elevation in the explicit scheme is much more rapid. Temperature in the shear zone rises faster and faster with time, due to the one-dimensional nature of limited diffusion (Ogawa, 1987). The explicit scheme is appropriate for calculating the shear instability propagation which has a similar timescale with time-steps of the scheme (Hulbert and Chung, 1996). Therefore, the curves of the explicit and implicit schemes become very different at the latter stage of viscous dissipation.

In Figure 3.2.c the temperature profiles at time = 400 Myr are obtained by the explicit (red line) and implicit (blue line) schemes. It shows that temperature profiles of depth between 15 km and 50 km are almost the same. However, in the region where the shear heating takes place, the temperature profiles are quite different. The explicit scheme produces two times larger temperature increase than that found with the implicit scheme.

A higher shearing rate induces vigorous positive feedback between temperature and plastic strain. If the generation of shear heating in Ogawa's model is governed by the quasi-static mechanism which would be well-resolved by a large time-step, the time-step in the implicit scheme should not be fluctuated, rather it should be uniform. Otherwise, the case of higher shearing rate is expected to be highly nonlinear. Therefore, small time-stepping is necessary to calculate the dynamic effect properly. Figure 3 illustrates the temporal evolution of time-step with different shearing rates under the implicit scheme. Thick and thin lines in Figure 3 depict variations of time-step for slow shearing (≤ 1.5 cm/yr) and fast shearing (≥ 3 cm/yr),

respectively. In the beginning stage, all models show the sharp increasing of time-step, because the initial time-step is set to be 1 second. For the case of slow shearing, the time-step is large and almost uniform throughout the whole time domain. Otherwise, all the thin lines are significantly fluctuating (see yellow stars in Figure 3). The black thin lines (for the case of 9.0 cm/yr) and the blue thin lines (for the case of 3.0 cm/yr) exhibit the fastest and latest fluctuations of time-step, respectively. This means that there is a marked correlation between time-step and nonlinearity from the fast shearing rate. Intense deformation rates cause large temperature increases. It forces the implicit solver to reduce drastically the time-step. Figure 3.4 shows the total iteration number with varying shearing rates. As expected, higher shearing rates increase the number of iterations necessary for the convergence within a given tolerance $O(10^{-5})$.

3.5. Two problems of lithospheric shear zone development

This section describes the two previous studies of shear zone development in the lithosphere that will be reexamined with my new adaptive scheme (i.e., ATS). The R model involves the case of lithospheric necking (Regenauer-Lieb and Yuen, 1998) and the S model is related with the development of shear zone at the interface of two materials with different elastic shear moduli (So et al., 2012). Originally, both R and S models employed the implicit scheme.

3.5.1. R model

Figure 3.5.a shows the configuration of the model where the lithosphere is 800 km long and 100 km high. The rheology is elasto-plastic, that is, the lithosphere behaves elastically below a certain stress criterion, but upon exceeding this yield criterion it deforms plastically. When the domain behaves plastically, the temperature/stress dependent creep rheology derived from laboratory experiments (Chopra and Paterson, 1981) is assigned (see Equation 9). The lithosphere was extended at a rate of 2-8 cm/yr from the right. The left

side is fixed whereas the top and bottom boundaries are prescribed as a free surface. A notch was prescribed at the top of the lithosphere so that the necking would start at that location.

According to Regenauer-Lieb and Yuen (1998), the plastic yielding starts at around 0.725 Myr, and within the next 0.1 Myr, the shear instability propagates until it reaches the base of the lithosphere. Once this point is reached, the temperature field of the lithosphere gradually becomes stabilized as the shear heating generated at the shear zone is balanced by the thermal diffusion toward the surrounding lithosphere whose temperature is relatively low.

3.5.2. S model

Figure 3.5.b describes the configuration of the model examining the generation of asymmetric instability zone at the interface of two materials with different shear moduli. The lithosphere is 600 km long and 150 km high with an elasto-plastic rheology. The boundary conditions assigned to this model is similar to those of R model. However, unlike Regenauer-Lieb and Yuen (1998), a weak zone such as fault and low viscosity zones was not predefined. The experiment was performed over a wide range of shear modulus contrast and activation energy (0–850 kJ/mol) for a constant compression rate of 2 cm/yr.

3.6. Results

Figure 3.6 is the plot of temperature field of the R model generated using the ATS. The implicit scheme was used for the stage 1 before plastic yielding and the stage 3 which corresponds to a post-shear-zone-development period where the heat generated at the shear zone is balanced by thermal diffusion. The explicit scheme was used for the stage 2 of plastic yielding, the initiation of shear instability and its rapid propagation. These results were compared with those obtained using single time-stepping approaches (i.e., both implicit

and explicit schemes). The overall pattern of shear heating and deformation was not much different among the different schemes. However, around the notch where plastic yielding and shear instability occur, a notable difference can be discerned among the predictions.

Figures 7a and 7b show respectively deformation around the notched area and the temperature field for different schemes. The final shape of the notch is not much different from its original configuration in the case of the implicit scheme, but it is more accentuated and localized for the explicit and the ATS (Figure 3.7.a). The temperature at the notch becomes higher, as one changes the time-stepping method from the implicit and explicit methods to the ATS. The difference in resulting temperature at the notch can be manifested more clearly in Figure 3.7.a which shows that not only does the temperature becomes higher but also is more confined for the ATS than for the other two schemes.

The emergence of fine-scale features when employing the ATS is also evident in the S model. Figure 3.8 is the temperature profile at the interface between two different parts of lithosphere. Again, a higher and more localized temperature is found around the asymmetric shear zone when using the ATS than the single time-stepping schemes.

Another important benefit of using the ATS is that the solution is stable and convergent over a wider range of model parameters. For instance, if one uses the implicit scheme alone, the solution diverges with increasing rate of extension in the R model. This shortcoming is demonstrated in Figure 3.9 where the red star symbols represent the time beyond which the implicit solver fails due to growing nonlinearity. The time span during which non-divergent solution can be obtained becomes shorter with increasing extension rate. The implicit solver tries to circumvent this problem by reducing the time-step near the plastic yielding point but there is a limit to the reduction it can make. As a result, the implicit method cannot handle cases with extremely high strain-rates.

In addition to the deformation rate, another model parameter that can affect the convergence is the contrast in material properties. For instance, a large shear modulus contrast can render the solution to be divergent in the S model. Figure 3.10 is a map showing the regime for divergence and convergence for the implicit scheme plotted as a function of compression rate and shear modulus contrast. In general, with increasing compression rate and shear modulus contrast, the solution becomes divergent. However, the region of divergence can be turned into convergence only if the explicit scheme is applied during stage 2. Hence, another important advantage of using the ATS method is that it can handle a wider range of situations than the implicit scheme. Many previous studies have applied the special treatment for stabilizing the solution, such as a cutoff setting of temperature and viscosity (e.g., Billen and Jadamec, 2012; Zhu et al., 2011). However, I should not ignore the sharp variation of material strength and strain-rates for an accurate determination. This is the reason why the explicit scheme is enforced for a large contrast in material properties and high velocity boundary condition.

An important issue in using the ATS is when to change between the different schemes. Figure 3.11.a is an example of the variations in time-step size for the implicit scheme. In most routines, this time-step size is automatically adjusted based on a certain criterion and tests performed after each iteration. In the case of R model, the time-step size is reduced from $\sim 30,000$ years to $\sim 3,000$ years (Figure 3.11.a). However, such a brute-force tactic involving a simple reduction may not be sufficient to guarantee the accuracy of the solution near the shear zone.

According to So et al. (2012), the velocity of shear instability propagation is $\sim 5 \cdot 10^{-6}$ m/s which greatly differs with the deformation rate of $\sim 5 \cdot 10^{-10}$ m/s during stage 2. In order to impose much smaller time-step such that the detailed features are not lost, it may be more practical to switch from the implicit to explicit schemes. In my study, I reduced the time-step size down to 0.3–3 years for stage 2 of the ATS in R model (Figure 3.11.b).

The disadvantage of the explicit method is that it takes an immense

amount of computational time due to its extremely small time-stepping. Therefore, when the balance is reached as in stage 3, it may be better to switch back to the implicit scheme. However, unlike the transition from stages 1 to 2, the exact timing may not be clear for transition from stage 2 to 3 since the thermal balance is reached slowly over a long timescale.

Figure 3.11.b shows the variation in the time-step for the ATS. The first and last stages, which are covered by the implicit scheme, represent respectively the elastic energy storage and maturing of shear localization. In Figure 3.11.b, sharp time-step change appears at the beginning step of the implicit scheme employed stages (see blue regions). The implicit scheme solver quickly increases time-step from 1 to 10^{11} – 10^{12} seconds (3,200–32,000 years) to save computational cost, since solutions in this stage are expected to be relatively stable. In the middle stage (red region), highly nonlinearity, sharp temperature change and fast shear instability propagation demanded the explicit scheme with small time-step. The implicit scheme can handle the small time-step, but the size of tangent stiffness matrix becomes larger with smaller time-step and the convergence may not be guaranteed within a given tolerance $O(10^{-5})$ (Choi et al., 2002). Definitely, I can keep adopting purely implicit scheme for all Stages 1, 2 and 3 with relaxing the error tolerance for using small time-stepping. If I relax the tolerance and then use small time-stepping in purely implicit scheme, the accuracy is not guaranteed. Otherwise, if I use small time-stepping with a fixed tolerance of 10^{-5} , the calculation of tangent stiffness matrix may be diverged. The way to solve this contradiction is developing new robust implicit solver. If the implicit solver is improved, I can catch the small time-stepping for short timescale physics and the accuracy with tight tolerance. This effort has been paid in applied mathematics (e.g., Burckhardt et al., 2009). On the other hand, the explicit scheme can manage very short timescale and highly nonlinearity and a large stiffness in time without any problems for convergence. In red region in Figure 3.11.b, the time-step hovers around 10^7 to 10^8 seconds (0.3–3 years). This time-step is consistent with that of Ogawa's study (1987), which argued that the timescale

for earthquake phenomenon is reduced from few hundreds of years to few years. This extremely short time-step does not cause any problems with convergence and allows an accurate determination of temperature elevation (~ 11 K at 1 Myr) from elastic energy release whose characteristic timescale is very short. The evolution of time-steps in S model with the ATS displays a similar trend with the R model.

3.7. Discussion

I have studied effectiveness of the ATS method for modeling geodynamical phenomena with multiple timescales. In particular, I have compared the single time-stepping methods against the ATS for shear zone development in the lithosphere by extension or compression.

The process of shear zone development can be divided into three stages. The stage 1 can be regarded as a period where the stress inside the medium builds up. The response of the lithosphere to the external force is purely elastic. The gradual buildup of stress eventually causes plastic yielding, and the stage 2 can be defined as the start of the yielding. An important aspect of the plastic yielding is the generation of shear heating which in turn reduces the mechanical strength. Although the amount may be small at the beginning, the temperature around the shear zone can grow rapidly as a result of a positive feedback between shear heating and deformation. The stage 2 thus can be characterized as a period during which the shear zone develops and the instability occurs within the lithosphere. In the case of R model, the yielding zone eventually reaches the bottom of the lithosphere. In the S model, two yielding zones, one at the top and the other at the bottom, merges at the center of the lithosphere. Then, the temperature within the lithosphere increases steadily as a balance is reached between the heat generated by the shear deformation and outward heat diffusion. The time at which this equilibrium occurs can be defined as the beginning of the stage 3. Unlike an abrupt transition from the stages 1 to 2, the transition from the stages 2 to 3 may be

gradual. In the implicit scheme, the transition between the different stages can be clearly identified by the change in time-stepping sizes.

Before investigating the benefits of the ATS, it is important to explore the characteristics and reliability of my technique. Two benchmark tests were performed. In the benchmark test I, the implicit and explicit schemes were compared for a case involving shear heating within pure viscous fluid. The test was done because an analytical solution exists in this particular case and also the mathematical description of the problem is somewhat similar to that of lithospheric shear zone development. In the Ogawa's model, where the explicit method of Ogawa (1987) was compared with my results, the two numerical results were almost identical except for a slight difference in the initiation time of instability.

When dealing with multi-timescale physics, it is important to understand how the differences in timescales may affect the numerical solutions. One way to characterize fast and slow processes is to compare the characteristic velocities of the different components in the computational domain. In the stage 1 where the lithosphere responds elastically according to the prescribed boundary condition, the characteristic velocity can be equated to the deformation rate. On the other hand, in the stage 2 where the important change in the system is caused by the reduction in mechanical strength as a result of plastic yielding and shear heating, the characteristic velocity can be regarded as the propagation speed of the shear zone. For the stage 1, the characteristic velocity is approximately 10^{-10} m/s. Compared to that of the stage 2 where the estimated propagation speed is roughly 10^{-6} m/s, the extraordinary characteristic velocity of stage 2 is 10^4 times faster but the duration of this period is extremely short. Unfortunately, most implicit schemes cannot adjust to such a rapid change in time-step sizes within a given tolerance of error $O(10^{-5})$ between the successive iterations. A viable option is to change from the implicit to the explicit schemes.

An important consideration that has to be taken into account is the balance between the internal and external forces during information

transportation from the stages 1 to 2. The implicit scheme ensures that the balance between internal and external forces is achieved as it continues to iterate until the nodal force equilibrium is achieved. On the other hand, the explicit scheme does not guarantee the balance because it is not constrained by the iteration. As a result, in the explicit scheme, artificial force can produce unrealistically large deformation with short time duration. Fortunately, in the problems that were considered, the generation of large artificial force did not occur during the transitions between stages.

The abrupt change of moment of inertia is one of the most important factors to control the whole crustal system (Homburg, 2012). However, the deformation rate is continuous during the transition between Stages 1 and 2. This means that the moment of inertia is almost uniform during my modeling. However, the propagation of thermal instability occurs suddenly and is very fast. This is the main reason why the explicit scheme is adopted only for the energy equation.

Comparison between the ATS and single time-stepping schemes results shows that, although the overall features appear to be similar, one important advantage gained by the ATS is that it produces a much fine-scale image near the localized shear zone (see Figures 7 and 8). For instance, according to the ATS, the temperature at the shear zone becomes higher by a few degrees after 1 Myr the deformation field becomes more localized.

The ability to predict correctly deformation and temperature at the shear zone has important implications for understanding the nature and behavior of abrupt feature such as fault, subduction initiation and slab detachment. Great efforts have been made to fill the gap between the tectonic stress on the lithosphere (e.g., slab pull and ridge push) and the required stress for explaining observed large ruptures on the Earth. The stress found in the nature is much smaller than the required stress for the shear deformation in the field (Regenauer-Lieb et al., 2008), thus many complex mechanisms, such as grain-size related weakening (Yamasaki, 2004) or damaged rheology (Karrech et al., 2011), have been employed. In summary, my ATS has the same aim of

reducing the stress for explaining observed large deformation and shear heating, but I take a distinct approach of choosing the ATS, which can help in the re-evaluation of the immediate deformation history in terms of choosing the proper time-integration scheme.

Moreover, one of the most intensively debated issues is related with the strength of fault and timing at which faults will slip. Predicting the exact temperature at the fault zone is vital as temperature is one of the major factors controlling the effective strength of the material. My study, which shows that the pattern of temperature distribution at the fault zone can be quite different depending on whether the ATS or single time-stepping approach is employed, can have an important impact on the studies involving local ductile instabilities which may cause earthquakes (Ide et al., 2007).

3.8. Conclusions

I have highlighted the importance of selecting appropriate schemes (i.e., implicit, explicit, the ATS schemes) for strongly nonlinear and stiff geodynamical problems, which have multiple timescales. I find that stages of triggering of elastic energy release and geometrical failure would require very small time-steps. Otherwise, relatively large time-step is enough for resolving steady phenomena, such as the stage before plastic yielding and the stage after achieving the equilibrium between shear heating and thermal diffusion. This strategy of choosing judiciously short and long time-steps should be for solving geodynamical problems and thus the modeler should consider the ATS and test the timing of switching from one into the other. The suitable schemes for the proper physical situations have been insinuated by King (2008), Regenauer-Lieb and Yuen (1998) and Kassam and Trefethen (2005), who noted that direct-explicit and iterative-implicit schemes should be chosen according to the characteristic of solution of problems. If a steady solution is not expected, the explicit scheme is better. Within this context, reliable previous studies, R and S models, have been comparatively analyzed with

considering three different schemes. Generally, in two-dimensional models, the ATS reveals the strongest and the most localized instability, which is favor to lithosphere-scale instabilities. Using either implicit or explicit schemes leads to underestimate the temperature elevation (~ 4 K at 1 Myr in the R and S models and ~ 200 K at 400 Myr in the Ogawa's model) by shear instability. Moreover, the implicit scheme has the tendency that the solution blows up, when strong nonlinearity is involved (e.g., fast deformation rate or high shear modulus contrast), because the solver uses short time-stepping, causing rapidly growing of tangent stiffness matrix under a given error tolerance (Choi et al., 2002). On the other hand, the extremely short time-step in the explicit scheme requires too many time-steps. Therefore, the explicit scheme does not efficiently calculate elastic energy storage in quasi-static compressional or extensional stages. Explicit and implicit methods have both advantages and drawbacks in terms of the computational time and the ability to capture the proper timescales. Therefore, I can advocate that this adaptive time-stepping (i.e., ATS) strategy can be helpful to other challenging problems in geodynamics, such as magma and mantle dynamics with multiple timescales.

3.9. Appendix

3.9.1. Explicit scheme

The explicit time-stepping scheme in ABAQUS adopts the second order central difference integration rules (Hibbit, Karlsson and Sorenson Inc., 2009):

$$\mathbf{u}_{k+1} = \mathbf{u}_k + \Delta t_{k+1} \dot{\mathbf{u}}_{k+1} \quad (1)$$

$$\dot{\mathbf{u}}_{k+\frac{1}{2}} = \dot{\mathbf{u}}_{k-\frac{1}{2}} + \mathbf{u}_k + \frac{1}{2}(\Delta t_{k+1} + \Delta t_k) \ddot{\mathbf{u}}_k \quad (2)$$

$$\mathbf{M} \ddot{\mathbf{u}}_{k+1} = \mathbf{F}_k - \mathbf{I}_k \quad (3).$$

where \mathbf{M} is the diagonal lumped mass matrix (Sun et al., 2000), \mathbf{F} and \mathbf{I} are the applied and internal force vectors, respectively. k means the index of time-step and $k \pm \frac{1}{2}$ are mid-increment indexes. $\dot{\mathbf{u}}$ and $\ddot{\mathbf{u}}$ definitely refer the first and second time derivatives of \mathbf{u} , respectively. Δt_k is the time-step at index k . The explicit procedure requires no iterations and no tangent stiffness matrix. The time-step in the explicit scheme for convergence and accuracy should be selected more carefully than that for the implicit scheme. Time-step criterion is defined below.

In text book for finite element structural modeling of elasticity (Bathe, 1996), the time-step Δt for stability of the solution is theoretically derived as:

$$\Delta t \leq \frac{2}{\omega_{\max}} \quad (4).$$

ω_{\max} is the highest dynamical frequency of the entire system and Δt is in practice computed by Belytschko et al. (2000):

$$\Delta t \approx \frac{L_{\min}^2}{c_d} \quad (5).$$

where c_d is the compressional wave speed for solid elements of isotropic material. L_{\min} is the spatial scale of the smallest element.

$$c_d = \sqrt{\frac{E(1-\nu)}{(1+\nu)(1-2\nu)\rho}} = \sqrt{\frac{\lambda + 2\mu}{\rho}} \quad (6)$$

E , ν and ρ are Young's modulus, Poisson's ratio and density, respectively. λ and μ are Lamé's constants.

For thermal modeling problems, the time-step Δt for the convergence is theoretically and practically defined according to the Hibbit,

Karlsson and Sorenson Inc. (2009):

$$\Delta t \leq \frac{2}{\lambda_{\max}} \quad (7)$$

$$\Delta t \approx \frac{L_{\min}^2}{\alpha} \quad (8)$$

λ_{\max} is the largest eigenvalue in the matrix system describing the temperature equation. α represents thermal diffusivity

$$\alpha = \frac{k}{\rho c_p} \quad (9).$$

k and c_p are thermal conductivity and specific heat, respectively.

For strong viscous heating, the time-steps are controlled by the fastest rate of the frictional heat production.

3.9.2. Implicit scheme

ABAQUS/Standard (Implicit) uses full Newton-Raphson iterative solver (Axelsson, 1977). Simple procedure description at time = t is below:

$$\Delta \mathbf{u}|_t^i = \mathbf{u}|_t^{i+1} - \mathbf{u}|_t^i \quad (10)$$

$$\mathbf{K}|_t \left[\Delta \mathbf{u}|_t^i \right] = \mathbf{F}|_t^i - \mathbf{I}|_t^i \quad (11).$$

Index i represents i^{th} iteration. $\mathbf{u}|_t^i$ means displacement and temperature vectors of i^{th} iteration in structural and thermal modelings, respectively.

$\mathbf{K}|_t$ is tangent stiffness matrix in configuration at time = t . $\mathbf{I}|_t^i$ and $\mathbf{F}|_t^i$ refer the internal force and applied force vectors at t and i^{th} iteration, respectively (Sun et al., 2000). $\mathbf{K}|_t$, $\mathbf{F}|_t^i$ and $\mathbf{I}|_t^i$ are calculated from $\mathbf{u}|_t^i$

and then I can compute $\Delta \mathbf{u}|_t^i$ using Equation 11. $\mathbf{u}|_t^{i+1}$ is derived by solving Equation 10 and then this iteration will be repeated until the convergence of $\mathbf{u}|_t^{i+N}$ is ensured.

For dynamic time integration, the implicit scheme applies first-order backward Euler operator and Hilber-Hughes-Taylor (Hughes et al., 1977) method which weights to information at t and $t + \Delta t$:

$$\mathbf{M} \ddot{\mathbf{u}}|_{t+\Delta t} + (1 + \alpha) \mathbf{K} \mathbf{u}|_{t+\Delta t} - \alpha \mathbf{K} \mathbf{u}|_t = \mathbf{F}|_{t+\Delta t} \quad (12)$$

$$\mathbf{u}|_{t+\Delta t} = \mathbf{u}|_t + \Delta t \dot{\mathbf{u}}|_t + \Delta t^2 \left[\left(\frac{1}{2} - \beta \right) \ddot{\mathbf{u}}|_t + \beta \ddot{\mathbf{u}}|_{t+\Delta t} \right] \quad (13)$$

$$\dot{\mathbf{u}}|_{t+\Delta t} = \dot{\mathbf{u}}|_t + \Delta t \left[(1 - \gamma) \ddot{\mathbf{u}}|_t + \gamma \ddot{\mathbf{u}}|_{t+\Delta t} \right] \quad (14)$$

Where

$$\beta = \frac{1}{4}(1 - \alpha^2), \quad \gamma = \frac{1}{2} - \alpha, \quad -\frac{1}{3} \leq \alpha \leq 0.$$

\mathbf{M} and \mathbf{K} are mass and tangent stiffness matrixes in reference configuration. $\dot{\mathbf{u}}$ and $\ddot{\mathbf{u}}$ are the first and second time derivatives of \mathbf{u} , respectively. α definitely should be a negative real number. $\alpha = -0.05$ is selected as a default value in ABAQUS (Hibbit, Karlsson and Sorenson Inc., 2009). For problems with strong shear heating, the time-steps are controlled by the maximum rate of mechanical heat production.

3.9.3. Benchmark test I

Previous studies dealing with comparisons between experimental results and numerical simulations (Nezo et al., 2011; Noels et al., 2004) have demonstrated that the explicit scheme is more similar to experimental results when the timescale of the physics is short. Since the laboratory experiments of geodynamical situations with multiple scales are technically very difficult, I

need to benchmark both schemes with the analytical solution for shear heating within the lithosphere with stress- and temperature-dependent rheology. Few people have focused on comparing their numerical results with the analytical solution because it is not easy to derive the solution of the problem due to the coupling between complicated rheology and governing equations.

In a theoretical study done 40 years ago, Sukanek et al. (1973) found an analytical solution of shear heating in viscous fluid with the temperature-dependent viscosity ($\mu(T)$, Equation 15). Turcotte and Schubert (2001) extended the solution to the geological scale and solved the differential equation, which is composed of the Brinkman number (Br, Equation 16) and a dimensionless temperature (θ , Equation 17) with a simplified assumption consisting of a constant tangential stress τ on the top and uniform initial temperature T_0 of the whole one-dimensional fluid with $h = 100$ km depth. The values of thermal conductivity (i.e., k) and activation energy (i.e., Q) are 4 W/(m·K) and 400 kJ/mol, respectively. R is universal gas constant. Equation 18 is the analytical relationship between the maximum temperature and the Br number (See details in section 7-5 of Turcotte and Schubert, 2001). I have compared the solution with my steady-state results from the one-dimensional explicit and implicit schemes with the same mesh size (~ 0.05 km, $\sim 2,000$ grid points). Time steps for each scheme are automatically determined by system configuration of each time-step.

$$\mu(T) = \mu_0 \exp \left\{ \frac{Q}{RT_0} \left(\frac{T_0}{T} - 1 \right) \right\}, \quad (\mu_0 = \text{viscosity at } T_0, 10^{24} \text{ Pa}\cdot\text{s}) \quad (15)$$

$$\text{Br} = \frac{\tau^2 h^2 Q}{k \mu_0 R T_0^2} \quad (16)$$

$$\theta = \frac{QT}{RT_0^2} \quad (17)$$

$$\text{Br} = \frac{2 \left(\frac{\text{Br} \cdot \exp(\theta_{\max})}{2} \right)}{\left\{ \cosh \left(\frac{\text{Br} \cdot \exp(\theta_{\max})}{2} \right)^{1/2} \right\}^2} \quad (18)$$

The quasi-static stage for elastic energy storing is not necessary for the purely viscous, fluid-like, viscoelastic model. Thus, I do not need to use the ATS. The purpose of this benchmarking is to determine which scheme is more appropriate for solving shear heating with a short timescale and complicated feedback between the mechanical and thermal instabilities. The Br number is changed along the branch only by varying the tangential stress for a given initial temperature of $T_0 = 400$ K and 1000 K. A low T_0 leads to a subcritical branch in which the initial viscosity is large, and thus, the tangential stress is the dominant factor for the temperature elevation. Otherwise, a high T_0 induces the supercritical branch in which the initial viscosity is low and the stress cannot be transmitted to the bottom. In this branch, the viscosity should be decreased for a mechanically and thermally steady-state even in the case of large tangential stress.

On the subcritical branch, the difference between the results from the low and high Br numbers is obvious (see the blue region in Figure 3.12). With the low Br number, both schemes generate a similar temperature because of the weak nonlinearity due to a low tangential stress leading to a small variation in the rheology and temperature. On the other hand, the explicit scheme shows far greater accuracy to the analytical solution and a high Br number. High stress induces a sharp change in the temperature and rheology, and this high nonlinearity requires short time-stepping with the explicit scheme. In the case of the supercritical branch (see the red region in Figure 3.12), both schemes show completely distinct results. This branch hardly converges to the steady-state due to the low viscosity and the subsequent high strain-rate with the implicit scheme. This result is consistent with my results showing that the implicit solver cannot guarantee numerical convergence within a given tolerance (10^{-5}) when a too high a deformation rates are assigned. Otherwise,

the maximum temperatures from the explicit scheme are close to the analytical solution. In this section, I have confirmed again the usefulness of the explicit scheme for solving problems involving shear heating in situations with simultaneous high shear stress and strain-rate.

3.10. References

- Axelsson, O. (1977), *Solution of Linear Systems of Equations: Iterative Methods*, Springer-Verlag, Berlin, Heidelberg, New York.
- Bathe, K.-J. (1996), *Finite element procedures*, Prentice-Hall, Inc.
- Belytschko, T., W.K. Liu and B. Moran (2000), *Nonlinear finite elements for continua and structures*, John Wiley & Sons Ltd., Chichester.
- Bercovici, D. (2002), The generation of plate tectonics from mantle convection, *Earth Planet. Sci. Lett.*, 6451 (Frontiers), pp. 1–15, doi: 10.1016/S0012-821X(02)01009-9.
- Billen, M. I. and M. Jadamec (2012), Origin of localized fast mantle flow velocity in numerical models of subduction, *Geochem. Geophys. Geosyst.*, 13, Q01016, doi: 10.1029/2011GC003856.
- Braeck, S. and Y. Y. Podladchikov (2007), Spontaneous thermal runaway as an ultimate failure mechanism of materials. *Phys. Rev. Lett.*, 98, 095504, doi: 10.1103/PhysRevLett.98.095504.
- Branlund, J.M., M. C. Kameyama, D.A. Yuen and Y. Kaneda (2000), Effects of temperature-dependent thermal diffusivity on shear instability in a viscoelastic zone: implications for faster ductile faulting and earthquakes in the spinel stability field, *Earth Planet. Sci. Lett.*, 182(2), pp. 171–185, doi: 10.1016/S0012-821X(00)00239-9.
- Brown, J. (2011), *Computational methods for ice flow simulation with applications to Jakobshavn Isbræ*, Ph.D thesis, ETH, Zurich <[80](http://e-</p></div><div data-bbox=)

collection.library.ethz.ch/eserv/eth:5692/eth-5692-02.pdf>.

- Burckhardt, K., D. Szczerba, J. Brown, K. Muralidhar, G. Székely (2009), Fast Implicit Simulation of Oscillatory Flow in Human Abdominal Bifurcation Using a Schur Complement Preconditioner, Euro-Par 2009 Parallel Processing. Springer Berlin Heidelberg, pp. 747-759.
- Butcher, J. C. (1990), Order, step size and stiffness switching, *Computing*, 44(3), pp 209-220, doi: 10.1007/BF02262217.
- Choi, H. H., et al. (2002), Comparison of Implicit and Explicit Finite-Element Methods for the Hydroforming Process of an Automobile Lower Arm, *The International Journal of Advanced Manufacturing Technology*, 20(6), pp. 407-413, doi: 10.1007/s001700200170.
- Chopra, P. N., and M. S. Paterson (1981), The experimental deformation of dunite, *Tectonophysics*, 78, pp. 453-473.
- Constantinescu, E. M. and A. Sandu (2010), Extrapolated implicit-explicit time stepping, *SIAM J. Sci. Comput.*, 31(6), pp. 4452-4477, doi: 10.1137/080732833.
- Dahlquist, G. and Björck, Å. (2008), *Numerical Methods in Scientific Computing: Volume 1*, SIAM.
- Gerya, T. V., D. A. Yuen and W. V. Maresch (2004), Thermomechanical modelling of slab detachment, *Earth Planet. Sci. Lett.*, 226(1-2), 101-116, doi: 10.1016/j.epsl.2004.07.022.
- Glen, J. W. (1955), The creep of polycrystalline ice, *Proc. R. Soc. Lond.*, A,228(1175), pp. 519-538, doi:10.1098/rspa.1955.0066.
- Griffiths, D. F. and D. J. Highman (2010), *Numerical Methods for Ordinary Differential Equations: Initial Value Problems*, Springer-Verlag, London.
- Hairer, E. and G. Wanner (2004), *Solving Ordinary Differential Equations II*, Springer-Verlag, Berlin.

- Hale, A. J., et al. (2010), Dynamics of slab tear faults: Insights from numerical modeling, *Tectonophysics*, **483**(1–2): 58-70, doi: 10.1016/j.tecto.2009.05.019.
- Hibbit, Karlsson and Sorenson Inc., (2009), Abaqus User's Manual Version 6.9 Vol. 1.
- Hobbs, B., K. Regenauer-Lieb and A. Ord (2007), Thermodynamics of folding in the middle to lower crust, *Geology*, **35**, pp. 175-178, doi: 10.1130/G23188A.
- Homburg, J. (2011), Field and theoretical investigations of strain localization: effects of mineralogy, shear heating and grain size evolution on deformation in the Earth, chapter 3.1., Ph.D thesis, Columbia University < <http://hdl.handle.net/10022/AC:P:18792>>.
- Hughes, T. J. R., R. L. Taylor and W. Kanoknukulchai (1977), A Simple and efficient element for plate bending, *International Journal for Numerical Methods in Engineering*, vol. 11, pp. 1529–1543, doi: 10.1002/nme.1620111005.
- Hulbert, G. and J. Chung (1996), Explicit time integration algorithms for structural dynamics with optimal numerical dissipation, *Computer Methods in Applied Mechanics and Engineering*, Vol. 137 pp.175-88, doi: 10.1016/S0045-7825(96)01036-5.
- Ide, S, G. C. Beroza, D. R. Shelly and T. Uchide (2007), A scaling law for slow earthquakes, *Nature* **447**, 76-79, doi: 10.1038/nature05780.
- Iserles, A. (1996), *A First Course in the Numerical Analysis of Differential Equations*, Cambridge Univ. Press, Cambridge, UK, 1996.
- Karato, S., (2008), *Deformation of Earth Materials: An Introduction to the Rheology of Solid Earth*, Cambridge University Press, London.
- Karrech, A., K. Regenauer-Lieb and T. Poulet (2011), Continuum damage mechanics for the lithosphere, *J. Geophys. Res.*, **116**, B04205, doi:

10.1029/2010JB007501.

- Kassam, A.-K. and L. N. Trefethen (2005), Fourth-order time-stepping for stiff PDEs, *SIAM J. Sci. Comput.*, 26, pp. 1214-1233, doi: 10.1137/S1064827502410633.
- Kaus, B. J. P. and Y. Y. Podladchikov (2006), Initiation of localized shear zones in viscoelastoplastic rocks, *J. Geophys. Res.*, 111, B04412, doi: 10.1029/2005JB003652.
- Kincaid, C. and P. Silver (1996), The role of viscous dissipation in the orogenic process, *Earth Planet. Sci. Lett.*, 142(3-4), pp. 271-288, doi: 10.1016/0012-821X(96)00116-1.
- King, S. D. (2008), *ConMan Manual*, www.geodynamics.org.
- King, S. D. et al. (2010), A community benchmark for 2-D Cartesian compressible convection in the Earth's mantle, *Geophys. J. Int.*, 180(1), pp. 73-87, doi: 10.1111/j.1365-246X.2009.04413.x.
- Langer, S., L. M. Olsen-Kettle, D. K. Weatherley, L. Gross, and H.-B. Mühlhaus (2010), Numerical studies of quasi-static tectonic loading and dynamic rupture of bi-material interfaces, *Concurrency Comput. Pract. Exper.*, 22(12), 1684–1702, doi: 10.1002/cpe.1540.
- Nezo, J., L. Dunai and B. H. V. Topping (2011), A mixed time integration scheme for virtual fabrication of steel plate girders, *Journal of Computers and Structures*, doi: 10.1016/j.compstruc.2011.05.018.
- Noels, L., L. Stainier and J.-P. Ponthot (2004), Combined implicit/explicit algorithms for crashworthiness analysis, *International Journal of Impact Engineering*, 30(8-9), pp. 1161-1177, doi:10.1016/j.ijimpeng.2004.03.004.
- Ogawa, M. (1987), Shear instability in a viscoelastic material as the cause of deep focus earthquakes, *J. Geophys. Res.*, 92, 13801–13810, doi:10.1029/JB092iB13p13801.

- Regenauer-Lieb, K. and D. A. Yuen (1998), Rapid conversion of elastic energy into plastic shear heating during incipient necking of the lithosphere. *Geophys. Res. Lett.*, 25(14), doi: 10.1029/98GL02056.
- Regenauer-Lieb, K., D.A. Yuen and J. M. Branlund (2001), The initiation of subduction: criticality by addition of water?, *Science*, 294 (5542), pp. 578–580, doi: 10.1126/science.1063891.
- Regenauer-Lieb, K., G. Rosenbaum and R. F. Weinberg (2008), Strain localisation and weakening of the lithosphere during extension, *Tectonophysics*, 458(1–4), 96–104, doi: 10.1016/j.tecto.2008.02.014.
- Scholz, C. H. (2002), *The Mechanics of Earthquakes and Faulting* (2nd Edition), Cambridge Univ. Press, Cambridge, UK.
- So, B.-D., D. A. Yuen, K. Regenauer-Lieb, and S.-M. Lee (2012), Asymmetric lithospheric instability facilitated by shear modulus contrast: implications for shear zones, *Geophys. J. Int.*, 190(1): 23-36, doi: 10.1111/j.1365-246X.2012.05473.x.
- Stadler, G., M. Gurnis, C. Burstedde, L. C. Wilcox, L. Alisic, and O. Ghattas (2010), The Dynamics of Plate Tectonics and Mantle Flow: From Local to Global Scales, *Science*, 329(5995), 1033-1038, doi: 10.1126/science.1191223.
- Sukanek, P. C., C. A. Goldstein, and R. L. Laurence (1973), The stability of plane Couette flow with viscous heating, *Journal of Fluid Mechanics*, 57(04), 651-670, doi: 10.1017/S002211207300193X.
- Sun, J. S., K. H. Lee and H. P. Lee (2000), Comparison of implicit and explicit finite element methods for dynamic problems, *Journal of Materials Processing Technology*, 105, pp. 110–118, doi: 10.1016/S0924-0136(00)00580-X.
- Turcotte, D. L. and G. Schubert (2002), *Geodynamics* (2nd edition), Cambridge University Press, London.

- Wang, S. P., S. Choudhry and T. B. Wertheimer (1997), Comparison between the static implicit and dynamic explicit methods for FEM simulation of sheet forming processes, White papers in MARC Corp.,.
- Yamasaki, T. (2004), Localized rheological weakening by grain-size reduction during lithospheric extension, *Tectonophysics*, 386(3-4), pp. 117-145, doi: 10.1016/j.tecto.2004.05.006.
- Zhu, G. and T. V. Gerya, S. Honda, P. J. Tackley and D. A. Yuen (2011), Influences of the buoyancy of partially molten rock on 3-D plume patterns and melt productivity above retreating slabs, *Phys. Earth. Planet. Inter.*, 185(3-4): 112-121.

3.11. Figures

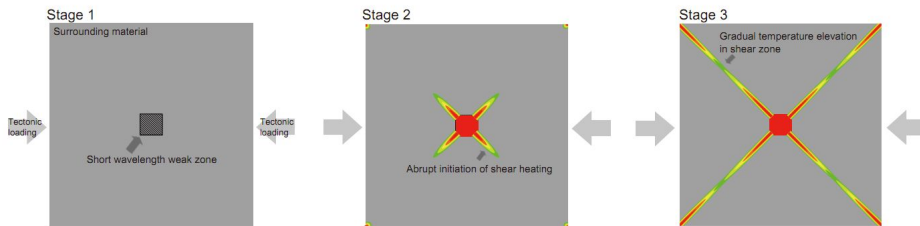
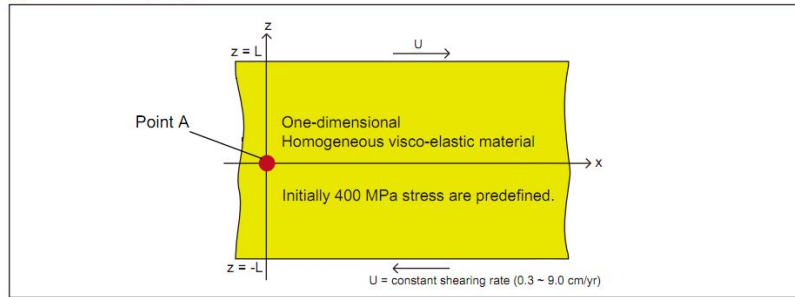
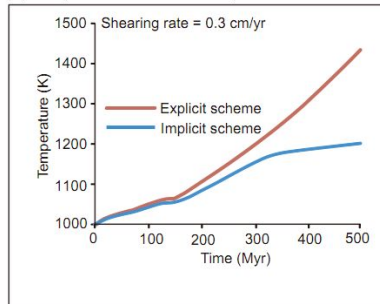


Figure 3.1. The cartoons showing three stages in shear zone development. Red color means high temperature or plastic strain-rate. Gray color represents small variation in temperature of strain-rate. Stages 1 and 3 are dominated by relatively long timescale physics, whereas stage 2 is under the short timescale nonlinear physics of the coupling between momentum, constitutive and energy equations.

(a) Ogawa model (1987)



(b) Temporal evolutions of temperature at Point A



(c) Temperature profiles at 400 Myr

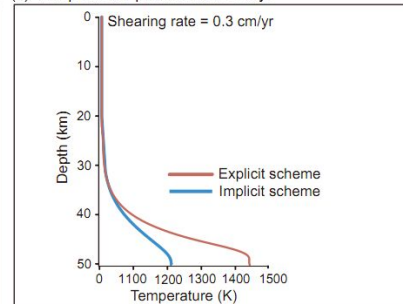


Figure 3.2. **a.** The schematic description for Ogawa's model (1987). Temporal temperature variation on homogeneous viscoelastic material is integrated under constant shearing rate condition. Simple one-dimensional evolution (z axis vs. temperature) is calculated. **b.** Temperature evolution with time at the central node of domain. Red and blue lines show temperature evolution from the explicit and implicit schemes, respectively. The explicit scheme makes faster and stronger shear instability. **c.** The temperature profile at time = 400 Myr. Red and blue lines refer temperature profiles using the explicit and implicit schemes, respectively.

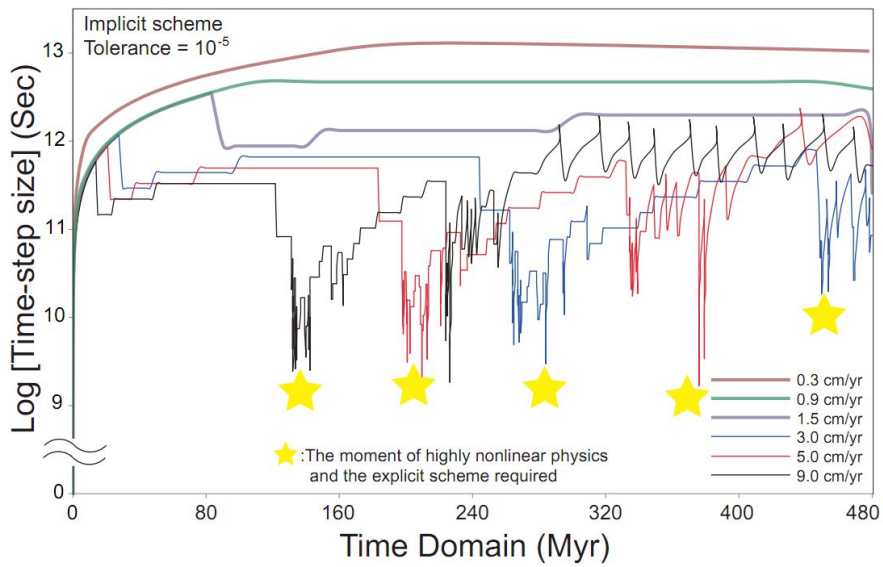


Figure 3.3. Temporal evolution of time-step with different shearing rate under the implicit scheme. Thick and thin solid lines depict cases of slow and fast shearing rates, respectively. Yellow stars point out the moment when the explicit scheme with short time-stepping should be applied.

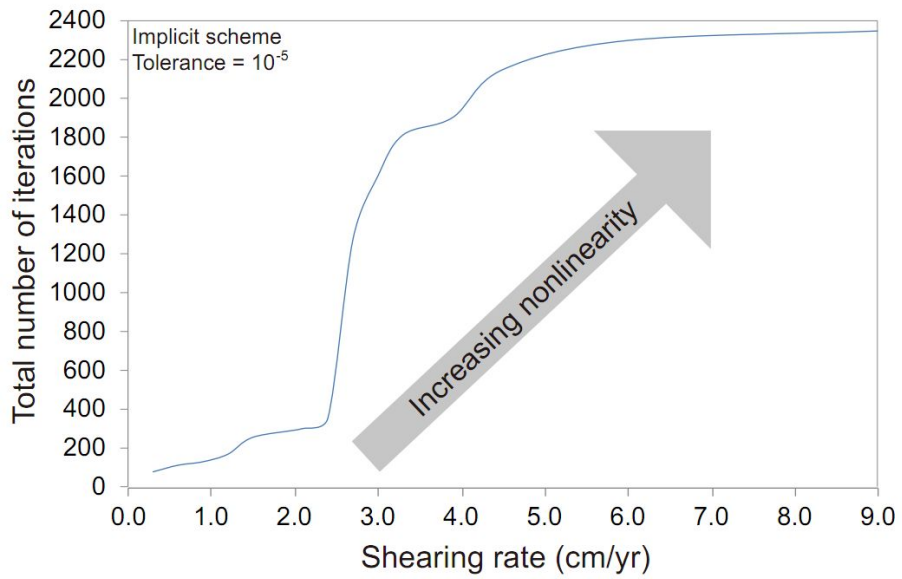
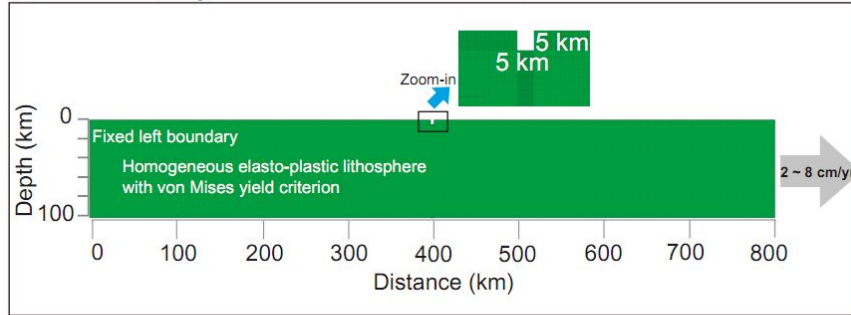


Figure 3.4. Total number of iterations with varying shearing rates. As expected, the higher shearing rate is applied, the larger number of iterations is required. Many iterations show clearly the long computing time.

(a) R model [*Regenauer-Lieb & Yuen, 1998*]



(b) S model [*So et al., 2012*]

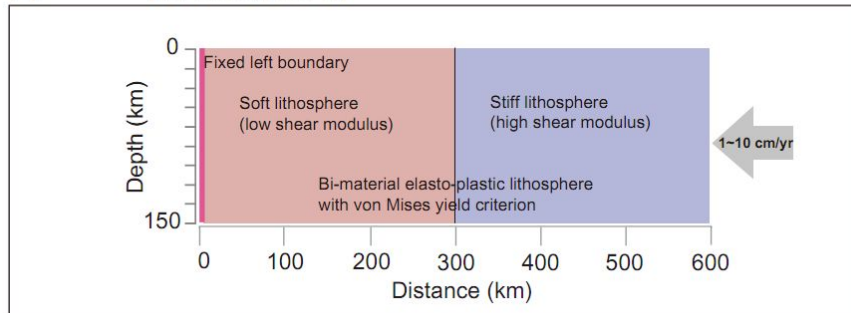


Figure 3.5. Descriptions for R (Figure 3.5.a) and S (Figure 3.5.b) models. R model uses homogeneous material and is suitable to observe tendency of deformation with three different time-integration schemes because of the notched zone where the stress is extensively concentrated. S model has the domain composed of two elastically heterogeneous elasto-plastic materials (i.e., bi-material situations).

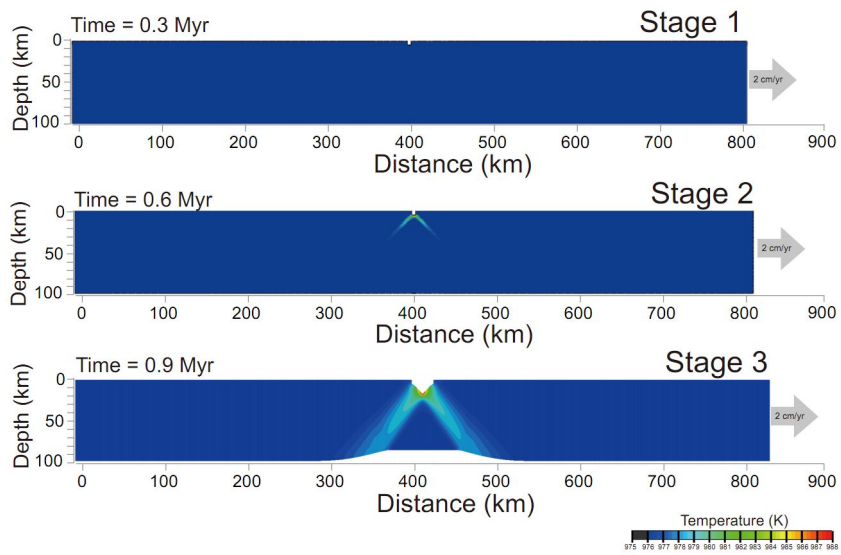


Figure 3.6. Numerical results of R model using the ATS. Detailed explanation of each stage, as given in Figure 3.1, is consistent with this figure.

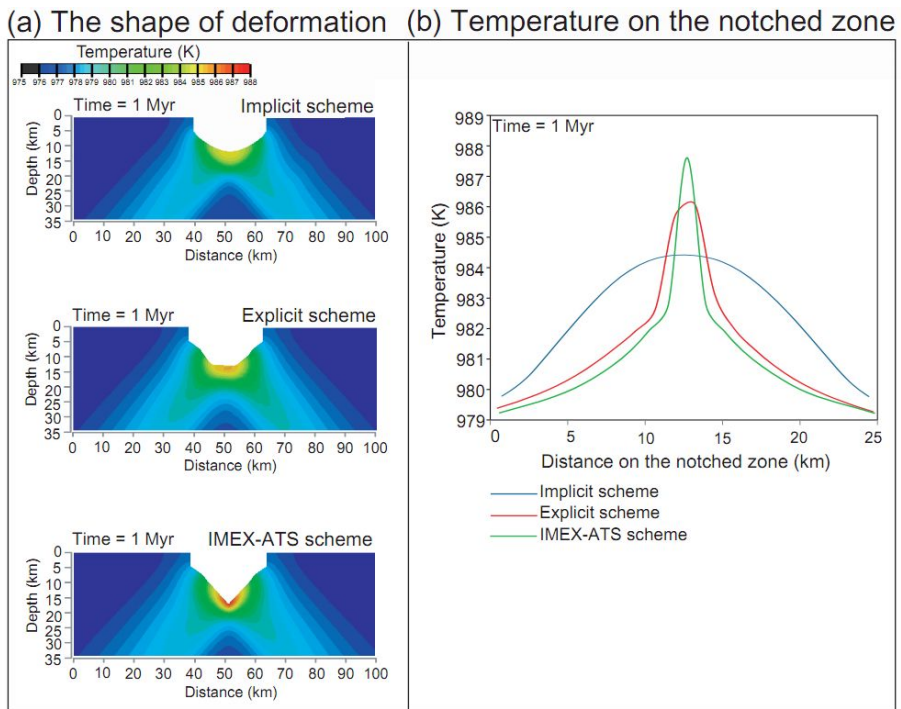


Figure 3.7. a. The deformation appearances and temperature distributions around notched zone at 1 Myr of R model. The deformation of the ATS produces the sharpest compared with other schemes. **b.** Temperature profile along the notched zone at 1 Myr of R model. Consistent with Figure 3.7.a, the ATS displays the most localized and highest temperature field.

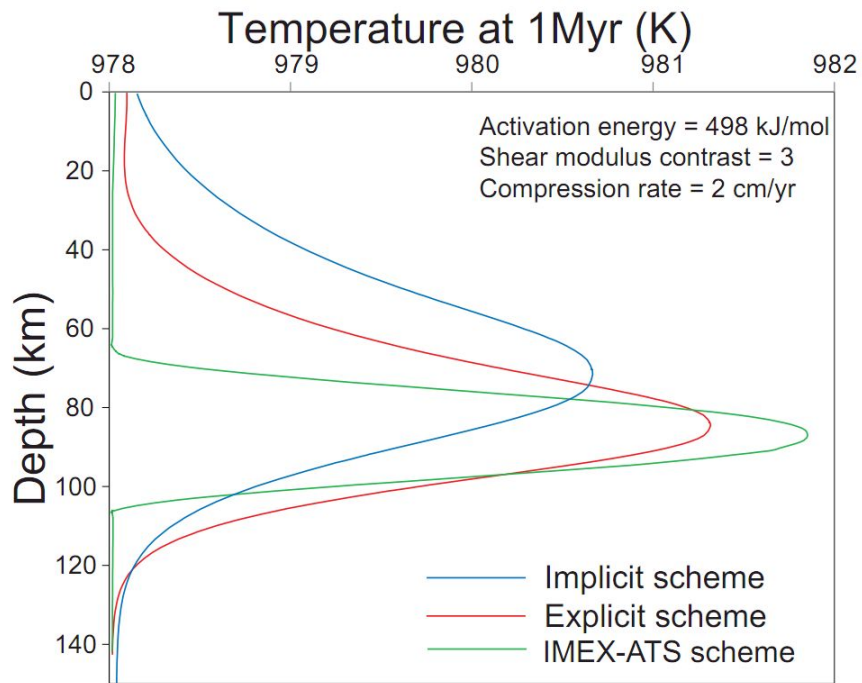


Figure 3.8. The temperature profiles along interface at 1 Myr with three different schemes for S model. The width of shear localized zone with the ATS is almost 2 times more localized compared with the implicit case.

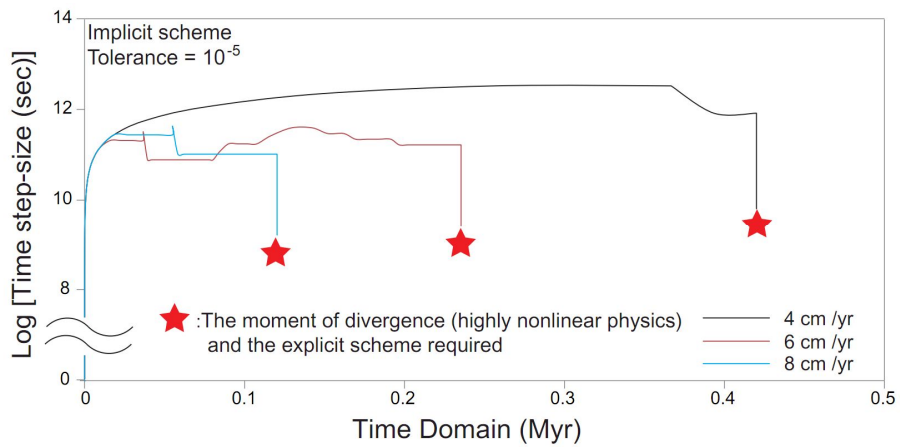


Figure 3.9. The variation of time-step with higher extension rate under the implicit scheme. Higher deformation rate induces quicker divergence. To reach convergence, I must use an explicit scheme at the time of divergence in the solution, as indicated by the red stars.

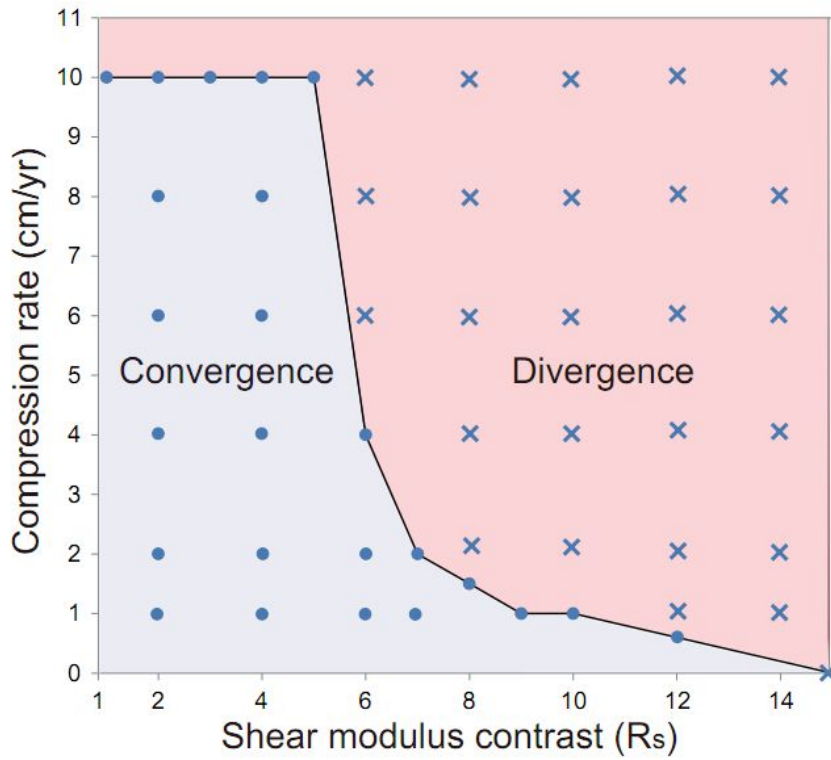
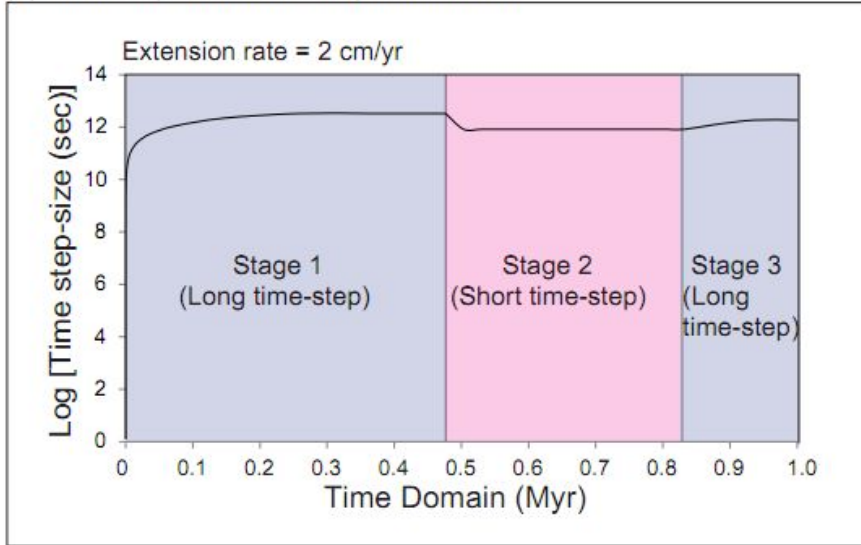


Figure 3.10. The map of convergence and divergence of S model under the implicit scheme. Solid circles and crosses indicate respectively the nature of convergence and divergence of the solutions. The convergence (blue zone) occupies lower shear modulus contrast and slower velocity, while the divergence (red zone) occurs in case of the higher shear modulus contrast and faster deformation rate.

(a) Time-step variation in implicit scheme



(b) Time-step variation in IMEX-ATS scheme

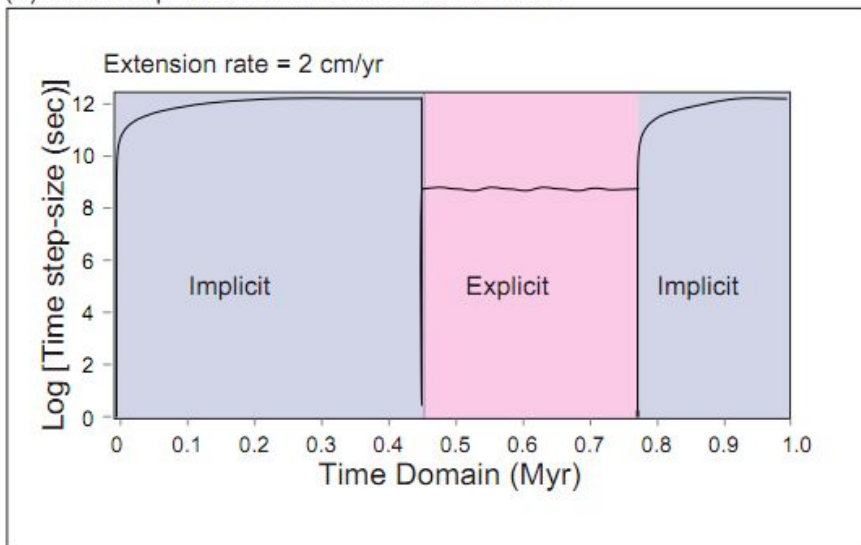


Figure 3.11. **a.** The evolution of time-step of R model in the implicit scheme with a slow extension of 2 cm/yr. The almost uniform time-step is shown, but clear time-step reduction in the stage of shear instability initiation appears. Higher velocity than 2 cm/yr does not converge in the implicit scheme. **b.** Temporal variation of time-step in R model under the ATS with extensional velocity = 2 cm/yr. Blue and red regions represent respectively implicit and explicit stages. The temporal evolution of time-steps in S model with the ATS displays a similar trend with R model.

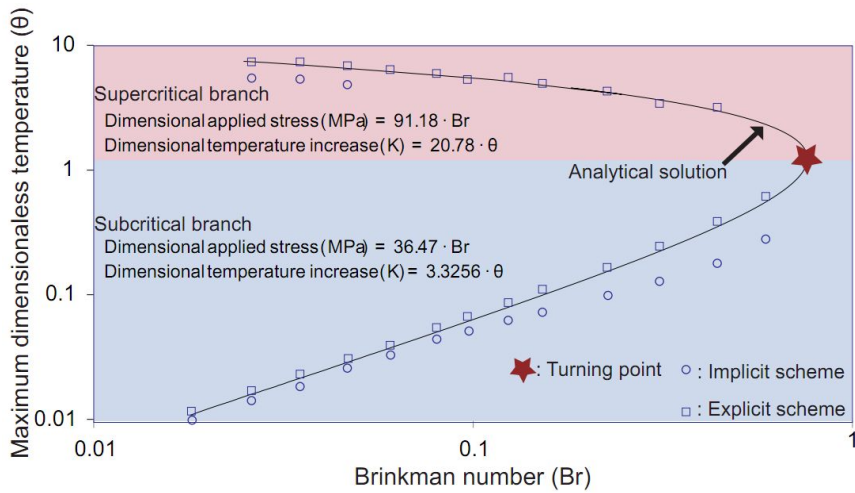


Figure 3.12. The comparison between analytical solution and numerical result with the explicit and implicit schemes. Black solid curve represents the analytical solution. Open rectangles and circles show numerical solution with the implicit and explicit schemes. Generally, the explicit scheme is more accurate to the analytical solution.

3.12. Tables

Table 1. Input parameters of assessments for three models

Variables	Symbol [Unit]	Ogawa's model	R model	S model
Specific heat	c_p [J/(kg·K)]	800	1240	1240
Thermal conductivity	k [W/(m/K)]	2.4	3.4	3.4
Density	ρ [kg/m ³]	3000	3300	3300
Shear modulus	μ [Pa]	use Young's modulus	use Young's modulus	variable
Young's modulus	K [Pa]	7×10^{10}	10^{11}	use shear modulus
Activation energy	Q [kJ/mol]	500	498	498
Universal gas constant	R [J/(K·mol)]	8.314	8.314	8.314
Power law exponent	n	3	4.48	4.48
Prefactor	A [Pa ⁻ⁿ ·s ⁻¹]	4.3×10^{-16}	5.5×10^{-25}	5.5×10^{-25}
Yield strength	σ_{yield} [MPa]	already yielded	100	100
efficiency from plastic work into shear heating	Ψ	1	0.9	0.9

Table 2. Differences of the three models being assessed

Variables	Ogawa's model	R model	S model
Dimension	one-dimensional	two-dimensional	two-dimensional
Material type	homogeneous	homogeneous	bi-material
Size of elements	0.05 km	fine part: 0.25×0.25 km coarse part: 1×0.25 km	fine part: 0.2×0.25 km coarse part: 1×0.25 km
Number of grid	~2,000	~450,000	~600,000
Rheology	strain-rate and stress dependent	same	same
Predefined weak	no	notched hole	no
Initial temperature	uniformly 978 K	uniformly 978 K	uniformly 978 K
Non-dimensionalization?	yes (see Ogawa, 1987)	no	no
Boundary velocity	0.3–9.0	2.0–8.0	0.1–12.0
Yield criterion	no	von Mises	von Mises

Chapter 4

Influence of Temperature-Dependent Thermal Conductivity on Surface Heat-Flow near Major Faults*

Abstract

I have studied with high-resolution finite element simulations the potential thermo-mechanical effects ensuing from positive feedback between temperature-dependent thermal conductivity $k(T) \propto (1/T)^b$ and frictional heating in a crust-lithosphere system with both brittle and viscoelastic rheology. The variable conductivity together with frictional heating causes drastic reduction in thermal conductivity and these changes can influence the heat-flux near major faults. When $b = 1$, the temperature is 400 K higher under the fault than that in uniform conductivity case. This is caused by the reduction in thermal conductivity under the surface fault with the temperature rise. Consequently, frictional heating dominates over vertical heat diffusion. In spite of the high temperature around the fault in variable conductivity cases, the surface heat-flux is 60 (for $b = 0.5$) to 80% (for $b = 1$) lower than that in the uniform conductivity case. The fault is thermally insulated by the vertical conductivity contrast between the warm frictional zone and the adjacent cold region underneath. I may be able to explain partly the lack of heat-flow anomalies near major faults and also concur with previous hypotheses on the nature of the shear strength associated with these faults.

Keyword: temperature-dependent conductivity, frictional heating, heat-flow paradox

* An edited version of this chapter is under “accepted” in Geophysical Research Letters in 2013.

4.1. Introduction

Previous heat-flow studies (e.g., Brune et al., 1969) have proposed that the fault stress inferred from surface heat-flow data (i.e., ~20 MPa) are 5 times lower than that expected based on laboratory-derived rock friction (i.e., ~100 MPa, Byerlee, 1978). This discrepancy has long been an outstanding problem (Zoback et al., 1987; Lachenbruch and Sass, 1992 and Saffer et al., 2003). To resolve this issue, many have argued that the effective shear strength of fault plane is weak (e.g., Carpenter et al., 2011) and also have suggested various weakening mechanisms such as a reduction of effective friction coefficient by rolling grain mechanism (Mora and Place, 1998), thermal decomposition (Han et al., 2007), melt formation by frictional heating (Hirose and Shimamoto, 2005), velocity-dependent friction coefficient (Di Toro et al., 2004). However, I cannot ignore the argument that the fault strength may also be strong. For instance, Scholz (2000) discussed that the stress rotation measurement in the Cajon Pass Scientific Borehole at the San Andreas Faults indicates that the fault is mechanically strong. For the strong fault hypothesis, a proper mechanism to mask a large frictional heat in fault plane should be required. Even in the case of weak fault, the reduction of shear strength may not be sufficient for a complete explanation of the lack of positive heat-flow anomalies.

Although previous works have successfully explained the reason why fault strength is weak, they have been focusing only on the effective shear strength such as frictional coefficient (e.g., Tembe et al., 2006). On the other hand, the temperature- and pressure-dependent thermal conductivity, which plays an important role in thermal evolution of the Earth (e.g., van den Berg et al., 2004 and Hauck et al., 1999), has not been considered too much in analyzing of the observed surface heat-flow data. Most numerical studies adopted uniform conductivity when modeling of the crustal processes (e.g., Williams and Narasimhan, 1989). However, variable conductivity causes a large heterogeneity in conductivity within the frictionally heated fault area. This contrast may have an influence on the surface heat-flow around major

faults. In this study I carry out numerical simulations to explore the relationships among variable thermal conductivity, frictional heating and heat-flow.

4.2. Numerical model

I have employed a two-dimensional thermal-mechanical finite element code, ABAQUS, under the plane strain assumption (Hibbit, Karlsson and Sorenson Inc., 2009). My model represents the topmost part of the crust-lithosphere system. Figure 4.1 shows a rectangular layered domain with an area of $1000 \times 100 \text{ km}^2$, which is composed of two layers of brittle Mohr-Coulomb crust ($1000 \times 30 \text{ km}$) (Schmalholz et al., 2009) and viscoelastic lithosphere ($1000 \times 70 \text{ km}$). I have also considered models with thermal conductivity characteristic of the continental crust and lithosphere (Whittington et al., 2009). I predefine the fault with a width of 80 km long and a higher shear strength compared to the surrounding crust in order to localize frictional heating around this fault. Subsequently, the localized heat source, which will be detected by the surface heat-flux, is created by the interaction between frictional heating and heat diffusion toward the surface. Red arrows around the top in Figure 4.1 mean the surface heat-flux \mathbf{q} , which are lessened by the reduction of thermal conductivity $\Delta k(T)$ from frictional heating. The left and right boundaries have respectively fixed and constant velocity (i.e., 2 cm/yr) conditions. The surface has a fixed temperature at 300 K. The constant basal heat-fluxes of 25 and 40 mW/m^2 are imposed at the bottom boundary, while both vertical boundaries are adiabatic. Additional explanations for the variables in my simulation can be found in Table 1.

The energy conservation law and the constitutive relation with the spin-rate tensor are solved with Eqns. (1) and (2) for the energy and rheology of the brittle crust and viscoelastic lithosphere

$$\rho c_p \frac{dT}{Dt} = \rho c_p \left[\frac{\partial T}{\partial t} + v_k \frac{\partial T}{\partial x_k} \right] = \frac{\partial T}{\partial x_i} \left(k(T) \frac{\partial T}{\partial x_i} \right) + Q \quad (1)$$

$$\text{and } \frac{D\tau_{ij}}{Dt} = \frac{\partial\tau_{ij}}{\partial t} + v_i \frac{\partial\tau_{ij}}{\partial x_i} - W_{ik}\tau_{kj} + \tau_{ik}W_{kj} \quad (2).$$

The last term Q on the right-hand side of Eq. (1) respectively represents frictional heating $Q_f = \tau_{ij}\dot{\epsilon}_{ij}$ (W/m^3) in the crust and shear heating $Q_s = \tau_{ij}\dot{\epsilon}_{ij}^{creep}$ (W/m^3) in the lithosphere. The rheology for crust is a brittle Mohr-Coulomb friction (e.g., Schmalholz et al., 2009)

$$\tau = \tan\theta + C \quad (3)$$

where θ and C are internal friction angle and cohesion. The fault has a larger internal friction angle for generating the frictional heating (see Table 1). The lithosphere is set to behave as a viscoelastic material with temperature/deviatoric stress-dependent creeping law (Chopra and Paterson, 1981). Elastic, creeping strain-rates and effective viscosity are express by following relations:

$$\dot{\epsilon}_{ij}^{elastc} = \frac{1}{2\mu} \frac{D\tau_{ij}}{Dt} \quad (4),$$

$$\dot{\epsilon}_{ij}^{creep} = AJ_2^{n-1} \tau_{ij} \exp\left(-\frac{E}{RT}\right) \quad (5)$$

$$\text{and } \tau_{ij} = 2\eta_{eff} \dot{\epsilon}_{ij}^{creep} \quad (6).$$

Previous studies (Hofmeister, 1999 and Kirby et al., 1996) have elucidated that thermal conductivity $k(T)$ varies as $(1/T)^b$:

$$k(T) = 1.7 \cdot (300/T)^b \quad \text{where } 0 \leq b \leq 1 \quad (7).$$

Although the thermal conductivity is also altered by pressure, the effect of temperature dominates over pressure (Whittington et al., 2009) in the shallow crust. Most minerals in the Earth have between 0.5 and 1 of b (Xu et al., 2004; Dobson et al., 2010 and Hofmeister et al., 2007). I add a realistic case where thermal conductivities are $k_f(T)$ for feldspar (Clauser and Huenges, 1995) in the crust and $k_o(T)$ for olivine (Hofmeister, 1999 and Whittington et al., 2009) in the lithosphere:

$$k_f(T) = 3 \cdot (300/T)^{1.0} \quad (8)$$

$$k_o(T) = 7 \cdot (300/T)^{1.0} \quad (9).$$

Two end-members with the highest and lowest values of conductivity are presented as reference models. The high end-member model has conductivities of 3 and 3.68 W/m/K for crust and lithosphere, respectively. On the other hand, the low end-member model adopts respectively 1.58 and 1.75 W/m/K for crust and lithosphere. These values are chosen by the minimum (i.e., 300 K and 570 K for crust and lithosphere) and maximum (i.e., 570 K and 1200 K for crust and lithosphere) temperatures for steady-state conduction.

Here I focus on the positive feedback between $k(T)$ and frictional heating in the governing equations of energy and momentum. The feedback may cause a thermal insulation due to the occurrence of strong conductivity contrast between the localization zone and surrounding regions.

4.3. Results

I will show results from high resolution numerical simulation dealing with the variation of conductivity leading to the contrast in conductivity. Figure 4.2 displays general features of temperature distribution in cases of $b = 0, 0.5$ and 1 with the basal heat-flux of 25 mW/m^2 . At the stage where 16% compression has been attained, I can see localized thermal instabilities around the imposed fault due to frictional heating and the subsequent rising geotherms. I plot isotherm lines to show the localized zone clearly. For larger values of b , the temperature around the fault zone is much higher than that of smaller value of b . Moreover, temperature distribution around the fault is most localized when $b = 1$. The large value of b means that the conductivity drops more sharply with increasing temperature. Previous studies already confirmed that the variable conductivity reinforces thermal instability in the lithosphere (Branlund et al., 2000) and also influences on thermal evolution of deep

mantle (Matyska and Yuen, 2006).

Figure 4.3.a shows vertical heat-flux distributions in the whole domain with $b = 0, 0.5$ and 1 . I applied the constant basal heat-flux condition (i.e., 25 mW/m^2) on the bottom boundary. At 16% compression, vertical heat-flow in all models remain nearly the same because frictional heating around the imposed fault and heat diffusion toward the surface are well balanced. In Figure 4.2, lower values of b creates weaker frictional heating and a broader distribution of temperature. However, in Figure 4.3.a, the case of lower b shows more efficient vertical heat conduction. In a general sense, it is natural that less steep temperature gradient produces less heat conduction. However, there is a complex interplay between a large amount of frictional heat and the observation of low heat-flow values. This phenomenon may suggest one alternative hypothesis to explain partially the lack of heat-flux anomalies near the San Andreas Fault system (e.g. Brune et al., 1969)

In order to follow the time histories of surface heat-flux at the Point A (see Figure 4.3a), I defined two stages in Figure 4.3.b. The former stage is simply for steady deformation leading to frictional heating at the predefined fault. In the latter stage, I terminate the deformation to stop the generation of heat and see how the heat-flux relaxes in various cases with different values of b . As I already discussed, the case of larger b shows weaker surface heat-flux even though this case embeds much warmer localized zone (see Figure 4.2). For this case, there can exist a strong contrast in thermal conductivity, which cannot occur in the case of constant conductivity (i.e., $b = 0$). In the latter stage, the heat-flux decreases with diffusion of the localized heat. The case of $b = 1$ shows the insensitive variation in surface heat-flux with time. Thus, I may infer that there exists a thermal insulator between the warm fault and the cold surrounding crust. On the other hand, the case of $b = 0$ depicts the fastest elevation and relaxation of heat-flux after the termination of deformation. Obviously, there is no thermal insulator in this case.

Figs. 4a and 4b display the vertical profiles of heat-flux and conductivity for explaining the relationship between weak heat-flow

anomalies and the thermal insulator. Furthermore, I have tested the effect of different background heat-flows (i.e., basal heat-flux boundary conditions of 25 and 40 mW/m²). Figure 4.4.a describes heat-flux profiles along the vertical central line crossing the domain (see the line AB in Figure 4.2) with varying values of b under 25 (solid lines) and 40 mW/m² (dashed lines) basal heat-fluxes. Although general features are similar in cases of both basal heat-fluxes, magnitudes of vertical heat-fluxes are shifted toward strong values in the case of 40 mW/m² basal heat-flux. To account the insulating effect of conductivity contrasts, I show thermal conductivity profiles along the line AB at 16% compression. The large value of b causes the sharp contrast in conductivity regardless of magnitudes of basal heat-fluxes. The maximum contrast in the conductivity between the hot fault and the cold surface is ~70% in the case of $b = 1$ (see the black line in Figure 4.4.b). I may speculate that this contrast retards the heat diffusion toward cold region. On the other hand, there is no contrast in conductivity in the case of $b = 0$. In this case, the heat can be diffused effectively. The heat diffusion is directly detected as a surface heat-flux because there is no longer any thermal insulator in the crust (see the green line in Figure 4.4.b and Figure 4.3.b).

I conducted one more model with realistic thermal conductivities $k_f(T)$ for feldspar in the crust and $k_o(T)$ for olivine in the lithosphere. Reference modeling with maximum (i.e., high end-member) and minimum (i.e., low end-member) conductivities were also performed. In Fig 4c, dashed red and green lines are respectively vertical heat-flow profiles of high and low end-members at 16% compression. On other hand, the solid black line represents the profile of realistic case with feldspar and olivine. The weakest surface heat-flow is shown in the case of variable conductivity, not in the low end-member. In order to distinguish the pure effect of the contrast in conductivity, I plot the profiles of heat-flux at the moment of same temperature (i.e., 750 K) in the center of localized zone (see Figure 4.4.d). The case of variable conductivity shows the weakest surface heat-flux at the same temperature. Compared with the high end-member, the flux is lower by around 50%. It is also caused by the thermal insulation from the contrast in

thermal conductivity (see Figure 4.4.b)

4.4. Discussion

Previous studies have investigated the effect of temperature/pressure-dependent thermal conductivity on geotherms (Hofmeister, 1999) and mantle dynamics (Dubuffet et al., 1999 and Maierová et al., 2012). Although they tried to understand how the variable conductivity modifies earlier thoughts on the thermal evolution of deep Earth, few have suggested that variable conductivity can affect the surface heat-flux, which is important observational constraint. Thermal conductivity is an influential factor for governing heat transport. Furthermore, the conductivity predominantly depends on the temperature (Whittington et al., 2009) in a condition of low temperature and low pressure. Thus, I may recognize that there can be a large discontinuity in the conductivity between localized heat sources (i.e., frictional/shearing heating zone) and surrounding medium at shallow crustal levels. This idea was applied to model the temperature structure within subducting slab (Hauck et al., 1999). Hauck et al. (1999) estimated that the possible depth of deep focus earthquake is much shallower than former thoughts, because the sharp contrast in conductivity due to phase transition causes the excessive heat accumulation below the 660 km phase boundary and metastable olivine cannot exist at the depth. In present study, the strongly localized frictional heating induces the conductivity contrast instead of the phase transition.

I have calculated the time histories of both temperature and heat-flow for different parameter values of variable thermal conductivity. Generally, the thermal structure and heat transport are mainly dictated by the competitive interaction between frictional heating and heat diffusion. However, the particular value of b in $k(T)$ determines the dominant effect. If the conductivity decreases with temperature elevation, this reduction suppresses the heat diffusion from the fault zone to the surrounding crust. Thus, temperature near fault is much higher than that of the uniform conductivity

case when I use the variable conductivity. Consequently, a significantly large conductivity contrast is induced in all models, except for the case of constant thermal conductivity. When $b = 1$, conductivity contrasts of $\sim 70\%$ are produced at a compression of 16%. Especially for the case of $b = 1$, its surface heat-flow is less than a quarter of that from constant thermal conductivity. Moreover, the contrast impacts the evolution of surface heat-flow. In the case of constant conductivity, the heat-flow rises fast with frictional heating and relaxes quickly after the cessation of the heating.

For the realistic situation with crust-lithosphere lithology included (see Figures 4.4.c and 4.4.d) where thermal conductivities are $k_f(T)$ for feldspar in the crust and $k_o(T)$ for olivine in the lithosphere (see eqns. 8 and 9). I then compared this result with high and low end-members which respectively have the maximum and minimum conductivities for each layers. The realistic case with $k_f(T)$ and $k_o(T)$ displays the lowest values of surface heat-flux compared with both high and low end-members. This finding is caused by the formation of zone with lower conductivity (i.e., 0.8-0.9 W/m/K) and the resultant thermal insulation. In general feldspar has been ignored due to its low conductivity in thermal-mechanical modeling (e.g., Höfer and Schilling, 2002). However, I may suggest that the extraordinary low value of feldspar's conductivity strongly influences on surface heat-flux over the heat-source such as frictional heating zone.

The thermal conductivity contrast has two important implications to explain the weak heat-flow anomalies near major faults. The one is that the contrast in conductivity insulates the heat near the fault from the surrounding crust. I observed that the heat-flux is weak and insensitive with time in spite of a great amount of heat around the fault when there is the conductivity contrast. This result implies that the contrast can cause thermal insulating effect within the localized region. The vertical heat transport from the localized zone is restricted and the surface heat-flow anomaly remains undetectably low. Unless comprehensive analysis of the variable conductivity with temperature and its contrast is performed, the observed heat-flow data

cannot give accurate information about thermal state inside the crust near faults. The other point is that mechanical strength of fault can be effectively reduced by the pronounced frictional heating due to insulating effect in the case of variable conductivity. Many laboratory experiments have shown that the strength is significantly affected by the temperature elevation. For instance, higher temperature due to the significant heating enhances rock melting (Kanamori et al., 1998) and thermal decomposition (Han et al., 2007), which are important mechanisms to reduce the strength of fault rock. The case of variable conductivity in present study also shows much higher temperature by ~ 400 K with enough deformation (i.e., 16%) compared with the case of uniform conductivity. I may suggest that the variable conductivity induce more reduction of the effective strength within localized friction zone. Therefore, a friction model with the variable conductivity may better explain the reduction of shear strength than that with the constant conductivity. In brief, my hypothesis is suggesting that the strongly temperature-dependent conductivity plays a non-negligible role in causing low surface heat-flow anomaly along major faults because of the insulation effect and the enhanced reduction of fault rock strength.

As I discussed above, I need to include additional realistic mechanisms such as temperature-induced strength weakening rheology (e.g., Hirose and Shimamoto, 2005 and Han et al., 2007) and advective heat transport (e.g., Smith and Chapman, 1983). If the shear strength reduction from frictional heating interplays with the variable conductivity, the feedback among frictional heating, surface heat-flux and strength reduction can be more complicated. The heating with variable conductivity and temperature-induced strength weakening mechanism causes two contrary effects of the strength reduction and the broadening of conductivity contrast. The former effect definitely decreases the surface heat-flux by low frictional heat generation. Otherwise, the latter increases heat-flux. In addition, the heat transport by fluidal convection also disturbs and redistributes the surface heat-flux, as well as the heat source. Rather than exclude these possibilities, I suggest that the

insulating effect can be cooperative with previous hypotheses. One more question I have to ask myself is if this insulation hypothesis also works when there is melted rock by frictional heating (Kanamori et al., 1998). I estimated 400 K larger temperature around the fault zone in the case of variable conductivity (i.e., $b = 1$). This temperature can cause melting in fault plane, which has been thought as an important factor for slip-rate and heat transport (e.g., McKenzie and Brune, 1972). Since melted rocks generally have lower conductivities than crystalline rocks (Pertermann et al., 2008), the existence of melts in fault plane may reduce the surface heat-flux due to an intensification of the thermal insulation and weakening shear strength around fault plane. If I use three-dimensional domain, there is the horizontal conductivity contrast, as well as the vertical contrast which I have seen in this study. This indicates that the surface heat-flux anomalies with three-dimensionality may be reduced more than what I reported in my two-dimensional study. Thus, I should evaluate further the contribution of horizontal conductivity contrast on the surface heat-flux.

4.5. Conclusions

Although I have focused on the purely conductive model with variable conductivity, my approach for solving the lack of positive heat-flow anomaly in major faults is fundamentally different from previous conjectures based on only shear strength of fault rocks. Some authors tried to propose different point of view, such as rolling grain mechanism (Mora and Place, 1998) and normal stress reduction by fault interface vibration (Brune et al., 1993), to move away from the general thoughts based on strength weakening mechanism. The thermal insulating effect in present study is also consistent with those efforts. The strong insulation, which comes mainly from the positive feedback between frictional heating and the dramatic reduction in the thermal conductivity, can be a good alternative explanation for the heat-flow constraint. This idea provides a novel means to clarify partly the low heat-flow anomalies and argues strongly for the use of variable thermal

conductivity.

4.6. References

- Branlund, J., Kameyama, M.C., Yuen, D.A., and Kaneda, Y., (2000). Effects of temperature-dependent thermal diffusivity on shear instability in a viscoelastic zone: Implications for faster ductile faulting and earthquakes in the spinel stability field. *Earth Planet. Sci. Lett.* v. 182, p. 171-185, doi: 10.1016/S0012-821X(00)00239-9.
- Brune, J. N., Henyey, T.L., and Roy, R.F., (1969). Heat Flow, Stress, and Rate of Slip along the San Andreas Fault, California. *J. Geophys. Res.* v. 74, p. 3821–3827, doi:10.1029/JB074i015p03821.
- Brune, J.N., Brown, S., and Johnson R.A., (1993). Rupture mechanism and interface separation in foam rubber models of earthquakes: a possible solution to the heat flow paradox and the paradox of large overthrusts. *Tectonophysics.* v. 218, p. 59-67, doi: 10.1016/0040-1951(93)90259-M.
- Byerlee, J.D., (1978). Friction of rock. *Pure and Applied Geophysics*, 116, 615– 626.
- Carpenter, B.M., Marone, C., and Saffer, D.M., 2011. Weakness of the San Andreas Fault revealed by samples from the active fault zone. *Nature Geoscience.* v. 4, p. 251–254, doi:10.1038/ngeo1089.
- Chopra, P. N. and Paterson, M. S., (1981). The experimental deformation of dunite. *Tectonophysics.* 78, pp. 453-473.
- Clauser, C., and Huenges, E., (1995). Thermal conductivity of rocks and minerals, in: T.J. Ahrens (Ed.), *Rock Physics and Phase Relations*, AGU Reference Shelf 3, AGU, Washington, DC, pp. 105-126.
- Di Toro, G., Golbsby, D.L., and Tullis, T.E., (2004). Friction falls toward zero in quartz rock as slip velocity approaches seismic rates. *Nature.* v. 427, p. 436–439, doi: 10.1038/nature02249.
- Dobson, D. P., Hunt, S. A., McCormack, R., Lord, O. T., Weidner, D. J., Li, L.,

and Walker, A. M., (2010). Thermal diffusivity of MORB-composition rocks to 15 GPa: Implications for triggering of deep seismicity. *High Pressure Res.* 30, 406–414.

Dubuffet, F., Yuen, D.A., and Rabinowicz, M., (1999). Effects of a realistic mantle thermal conductivity on the patterns of 3-D convection. *Earth Planet. Sci. Lett.* v. 171, p. 401-409, doi: 10.1016/S0012-821X(99)00165-X.

Han, R., Shimamoto, T., Hirose, T., Ree, J.-H., Ando, J.-i., (2007). Ultralow Friction of Carbonate Faults Caused by Thermal Decomposition. *Science.* 316, 878, doi: 10.1126/science.1139763.

Hauck, S.A., Phillips, R.J., Hofmeister, A.M. (1999). Variable conductivity: effects on the thermal structure of subducting slabs, *Geophys. Res. Lett.* 26, p. 3257 – 3260.

Hibbit, Karlsson and Sorenson Inc. (2009). *Abaqus/Standard User's Manual Version 6.9, Vol.1.*

Hirose, T., Shimamoto, T., (2005). Growth of molten zone as a mechanism of slip weakening of simulated faults in gabbro during frictional melting. *J. Geophys. Res.* 110, B05202, doi:10.1029/2004JB003207.

Höfer, M., and Schilling, F. R., (2002). Heat-transfer in quartz, orthoclase, and sanidine at elevated temperature, *Phys. Chem. Miner.* 29, 571–584.

Hofmeister, A. M., (1999). Mantle Values of Thermal Conductivity and the Geotherm from Phonon Lifetimes. *Science.* v. 283, p. 1699-1706, doi: 10.1126/science.283.5408.1699.

Hofmeister, A.M., Branlund, J.M., and Pertermann, M. (2007). Properties of Rocks and Minerals–Thermal Conductivity of the Earth. *Treatise on Geophysics*, Elsevier, Amsterdam, 2007, P 543-577, doi: 10.1016/B978-044452748-6.00048-1.

Kanamori, H., Anderson, D.L., and Heaton, T.H., (1998). Frictional Melting

During the Rupture of the 1994 Bolivian Earthquake. *Science*. v. 279, p. 839-842, doi: 10.1126/science.279.5352.839.

Kirby, S. H., Stein, S., Okal, E. A. and Rubie, D. C., (1996). Metastable mantle phase transformations and deep earthquakes in subducting oceanic lithosphere. *Rev. Geophys.* 34(2), 261–306, doi:10.1029/96RG01050.

Lachenbruch, A. H., and Sass, J. H., (1992). Heat flow from Cajon Pass, fault strength, and tectonic implications. *J. Geophys. Res.*, v. 97, p. 4995–5015, doi:10.1029/91JB01506.

Maierová, P., Chust, T., Steinle-Neumann, G., Čadek, O. and Čížková, H. (2012). The effect of variable thermal diffusivity on kinematic models of subduction. *J. Geophys. Res.* 117, B07202, doi:10.1029/2011JB009119.

Matyska, C., Yuen, D.A., (2006). Lower mantle dynamics with the post-perovskite phase change, radiative thermal conductivity, temperature- and depth dependent viscosity. *Earth Planet. Sci. Lett.* 154, 196–207.

McKenzie, D., and Brune, J.N., (1972). Melting on fault planes during large earthquakes. *Geophysical Journal of the Royal Astronomical Society*. v. 29, p. 65–78, doi:10.1111/j.1365-246X.1972.tb06152.x.

Mora, P. and Place, D., (1998). Numerical simulation of earthquake faults with gouge: Toward a comprehensive explanation for the heat flow paradox. *J. Geophys. Res.*, v. 103, p. 21,067–21,089, doi:10.1029/98JB01490.

Pertermann, M., Whittington, A.G., Hofmeister, A.M., Spera, F.J., and Zayak, J., (2008). Thermal diffusivity of low-sanidine single-crystals, glasses and melts at high temperatures. *Contrib. Mineralogy and Petrology* 155, 689-702, doi: 10.1007/s00410-007-0265-x

Saffer, D.M., Bekins, B.A. and Hickman, S., (2003). Topographically driven groundwater flow and the San Andreas heat flow paradox revisited. *J. Geophys. Res.*, v. 108, doi:10.1029/2002JB001849.

- Schmalholz, S. M., Kaus, B. J.-P., and Burg, J.-P., (2009). Stress-strength relationship in the lithosphere during continental collision, *Geology*, 37(9), 775-778.
- Scholz, C. H., (2000). Evidence for a strong San Andreas fault. *Geology*, v. 28, p. 163– 166.
- Smith, L. and Chapman, D. S. (1983), On the thermal effects of groundwater flow: 1. Regional scale systems. *J. Geophys. Res.* 88, p. 593 – 608.
- Tembe, S., Lockner, D. A., Solum, J. G., Morrow, C. A., Wong, T., and Moore, D. E., (2006). Frictional strength of cuttings and core from SAFOD drillhole phases 1 and 2. *Geophys. Res. Lett.* 33, L23307, doi:10.1029/2006GL027626.
- van den Berg, A.P., Yuen, D.A., and Rainey, E.S.G., (2004). The influence of variable viscosity on delayed cooling due to variable thermal conductivity: *Phys. Earth Planet. Inter.* v. 142, p. 283 – 295.
- Whittington, A.G., Hofmeister, A.M., and Nabelek P.I., (2009). Temperature-dependent thermal diffusivity of the Earth's crust and implications for magmatism. *Nature*, v. 458, p. 319-321, doi: 10.1038/nature07818.
- Williams, C. F., and Narasimhan, T. N., (1989). Hydrogeologic constraints on heat-flow along the San Andreas fault—A testing of hypotheses, *Earth Planet. Sci. Lett.* 92(2). 131–143.
- Xu, Y., Shankland, T.J., Linhardt, S., Rubie, D.C., Langenhorst, F., and Klasinski, K., (2004). Thermal diffusivity and conductivity of olivine, wadsleyite and ringwoodite to 20 GPa and 1373 K. *Phys. Earth Planet. Inter.* v. 143-144, p. 321–336.
- Zoback, M.D., Zoback, M.L., Mount, V.S., Suppe, J., Eaton, J.P., Healy, J.H., Oppenheimer, D., Reasenber, P., Jones, L., Raleigh, C.B., Wong, I.G., Scotti, O., and Wentworth, C., (1987). New evidence on the state of stress of the San Andreas fault system. *Science*. v. 238, p. 1105–1111.

4.6. Figures

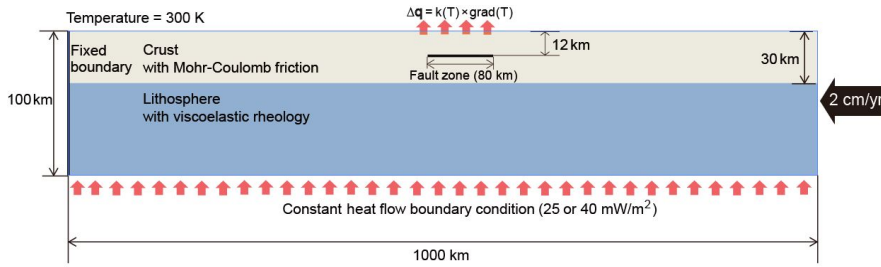


Figure 4.1. The schematic description for my model. The thin fault with the greater internal friction angle (i.e., the fault zone) is embedded in the Mohr-Coulomb brittle crust. This imposed fault zone may correspond to the asperity patch that generates the frictional heating. The left and right vertical boundaries are thermally insulated. Red arrow at the bottom boundary means that constant heat-flux. I used 25 and 40 mW/m².

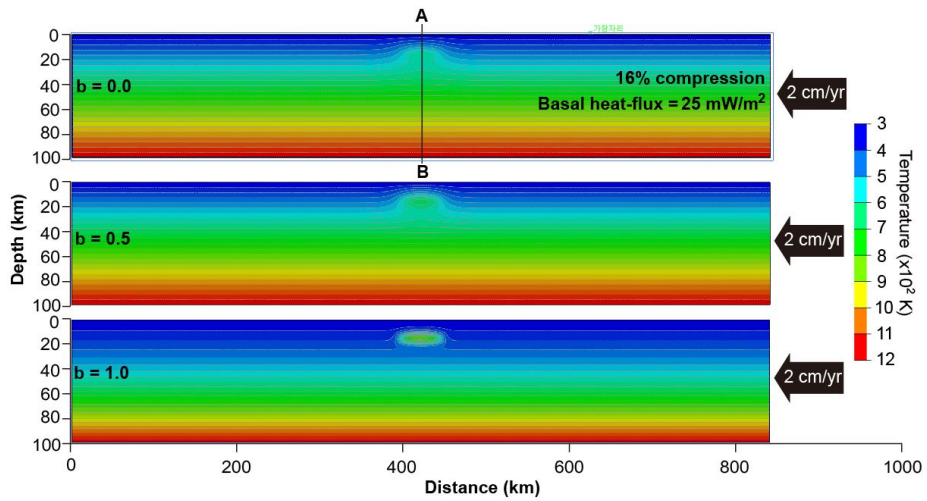


Figure 4.2. The temperature distribution with varying values of b at 16% compression under 25 mW/m^2 basal heat-flux condition. The Large value of b reinforces the frictional heating through suppressing the heat diffusion. The case of $b = 0$ shows the smallest amount of heat generation and the broadest temperature distribution. Although the case of $b = 1$ should show the strongest surface heat-flux, the feature of heat-flux is not consistent with the temperature distribution (see Figs. 3a and 3b).

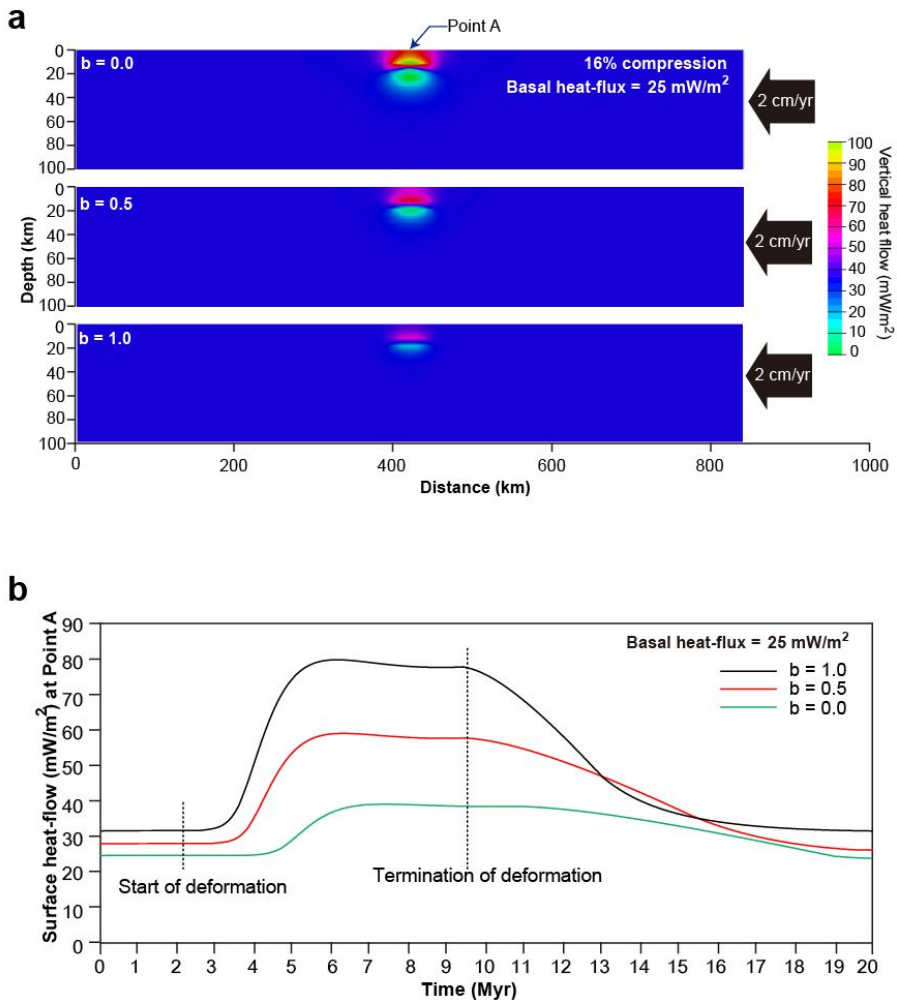


Figure 4.3. a. Heat-flux distributions with varying values of b at 16% compression. In contrast with Figure 4.2., the heat-flux shows the most vigorous features in the case of $b = 0$. When $b = 1$, the heat-flux is very weak in spite of the highest temperature in the localized friction zone. **b.** Temporal evolutions of the heat-flux with varying values of b observed at the Point A (see Figure 4.3.a). When $b = 1$, the heat-flux is weakest (80% less than the case of $b = 0$) and most insensitive to frictional heating. Moreover, the heat-flux relaxation after the termination of deformation is also slowest. Otherwise, when $b = 0$, the heat-flux is very sensitive. This means that there is a mechanism to prevent heat-flow when b is larger than 0 (i.e., variable conductivity case)

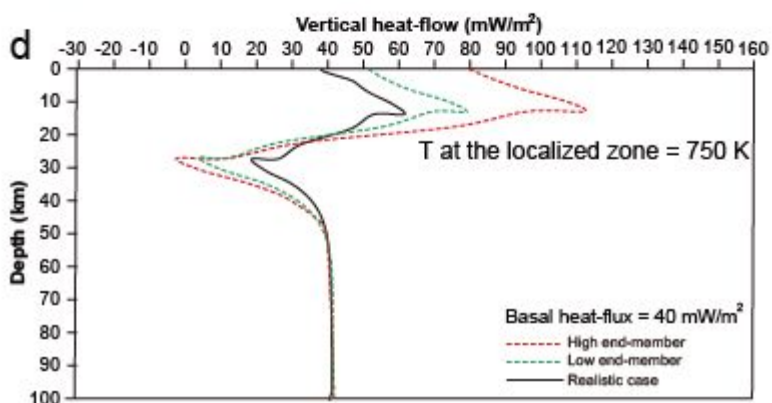
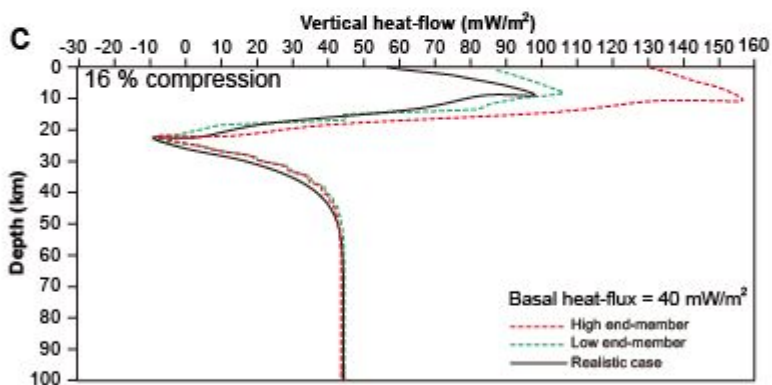
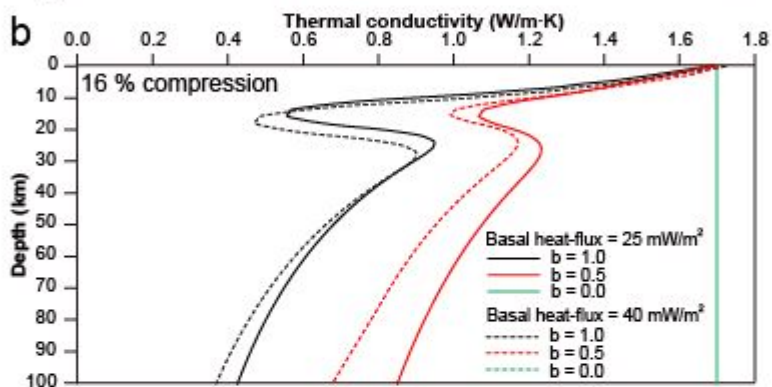
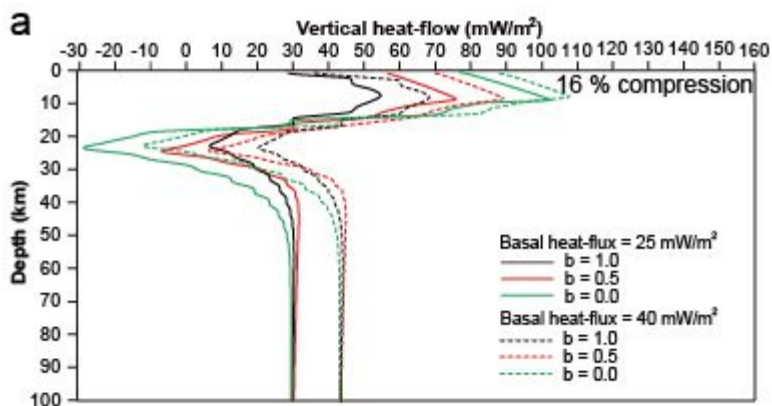


Figure 4.4. a. The heat-flux profiles along the line AB with varying values of b in cases of 25 mW/m^2 (solid lines) and 40 mW/m^2 (dashed lines) basal heat-fluxes. Both cases show that the weak heat-flux in the case $b = 1$. Negative values of heat-flux mean the heat-flux toward the bottom boundary. **b.** The conductivity profiles along the line AB (see Figure 4.2) with varying values of b . There are clear conductivity contrast in the case of $b = 1$ regardless of values of the basal heat-flux. This contrast in conductivity acts as a thermal insulator. Due to this insulator, the heat-flux and temperature at the localized zone shows opposite results. **c.** The heat-flux profiles at 16% compression of high, low end-members (dashed lines) and realistic case with conductivities of feldspar for the crust and olivine for the lithosphere. High and low end-members respectively have upper and lower bounds of thermal conductivity for each layer. The upper bounds of conductivities are 3 W/m/K for the crust (i.e., at 300 K) and 3.68 W/m/K (i.e., 570 K). The lower bounds are 1.58 W/m/K for the crust (i.e., at 570 K) and 1.75 W/m/K (i.e., 1200 K). **d.** The heat-flux profiles at the same temperature (i.e., 750 K) in the localized zone. I can see the pure effect of insulating effect from the conductivity contrast. At the same temperature, the realistic case shows the weakest heat-flux profiles.

4.8. Table

Table 1. Input parameters and notations

Symbol [Unit]	Values	Descriptions
t		time
D/Dt		material derivative
x_i		coordination along the i -direction
v_i		velocity in the i -direction
τ_{ij}		deviatoric stress tensor
θ_s	25°	Angle of internal friction of surrounding crust
C_s	30 [MPa]	Cohesion of surrounding crust
θ_f	40°	Angle of internal friction of the fault
C_f	40 [MPa]	Cohesion of the fault
W_{ij}	$\frac{1}{2} \left[\frac{\partial v_j}{\partial x_i} - \frac{\partial v_i}{\partial x_j} \right]$	spin-rate tensor
J_2	$\left(\frac{1}{2} \tau_{ij} \tau_{ij} \right)^{1/2}$	The second invariant of τ_{ij}
ρ	3000 [kg/m ³]	density
c_p	900 [J/(kg·K)]	specific heat
μ	10 ¹¹ [Pa]	shear modulus
E	498 [kJ/mol]	activation energy
R	8.314 [J/(K·mol)]	universal gas constant
n	3	power law exponent

A $4.3 \times 10^{-16} [\text{Pa}^{-n} \cdot \text{s}^{-1}]$ prefactor

ν 0.3 Poisson's ratio
